

SYNTHESIS AND CHARACTERIZATION OF MELTING GEL-WAX COMPOSITES

By

CAILLIN RYAN

A thesis submitted to the

School of Graduate Studies

Rutgers, The State University of New Jersey

In partial fulfillment of the requirements

For the degree of

Master of Science

Graduate Program in Materials Science and Engineering

Written under the direction of

Lisa C. Klein

And approved by

New Brunswick, New Jersey

May 2020

ABSTRACT OF THE THESIS

Synthesis And Characterization Of Melting Gel-Wax Composites

By

CAILLIN RYAN

Thesis Supervisor: Professor Lisa C. Klein

Sol-gel processing is an integral tool in developing inorganic-organic nanocomposite materials from wet chemistry techniques. By controlling the hydrolysis and condensation of various alkoxysilane precursors, tunable hybrid structures and properties can be achieved. A special class of sol-gel nanocomposites are so called “melting gels”, which thermally cure like an epoxy, but produce organically functionalized silicates. These melting gels are noted for their adhesion, hermeticity, chemical stability, and thermal stability.

This thesis focuses on the synthesis and characterization of new wax-melting gel composites. Both paraffin and microcrystalline waxes were successfully dispersed as microparticles in a melting gel matrix through in-situ emulsification with a silicone-based

surfactant. “Par-gels” and “Micro-gels” were synthesized with between 5.2 and 17.6 vol % wax. The samples were characterized using profilometry, optical microscopy, and SEM analysis. Additionally, the dielectric behavior of these wax-gels was evaluated in the RF spectral range (~ 1 -1000 kHz) and measured as a function of cumulative thermal history.

It was found that the emulsion stability of Par-gels is greater than that of Micro-gels. Specifically, Micro-gels contained internal pools of wax and surface segregated wax islands, while Par-gels showed more uniform mixing. Using image analysis with SEM and optical microscopy to resolve particle sizes, the distributions were best fitted with a Gamma distribution for particle sizes between ~ 0.1 -300 microns. Micro-gels exhibited larger median particle sizes than Par-gels, but both showed that the majority of their wax content was microparticles between ~ 5 -50 microns. Additionally, it was found that the dielectric properties were insensitive to wax content from 0-17.6 vol%. In addition, one week of sustained thermal treatments at $\sim 175^{\circ}\text{C}$ caused the dielectric behavior of all samples to converge into a narrow range. These thermal aging effects suggest that melting gels continue to undergo structural changes beyond the recommended consolidation conditions.

ACKNOWLEDGEMENTS

First and foremost, I need to reserve an especially immense gratitude to Dr. Lisa Klein and for her four years of guidance in my undergrad/grad career at Rutgers. None of this research would be possible without her support and wisdom. Also, I would like to sincerely thank Dr. Ahmad Safari and Dr. Koray Akdogan for agreeing to be my committee members and thoroughly reviewing my thesis drafts. I would like to express my gratitude to Dr. Safari's research assistants, Gabi Tagliaferro and Jack Leber, for training and allowing me to use the impedance analyzer. Additionally, I must thank Dr. Bob Horvath and Ethan Benderly-Kremen for training and allowing me to use the desktop SEM. Furthermore, I express my earnest gratitude to Dr. Andrei Jiteanu for his years of guidance with melting gel synthesis and characterization. Lastly, I would like to thank my family for investing and supporting my education for the past 5 years.

TABLE OF CONTENTS

	<u>PAGE</u>
ABSTRACT	ii-iii
ACKNOWLEDGEMENTS	iv
LIST OF TABLES	viii
LIST OF FIGURES	ix-xii
LIST OF APPENDICES	xii
I. INTRODUCTION	
1.1 SOL-GEL PROCESSING	
1.1.1 BACKGROUND	1-4
1.1.2 ADVANTAGES AND LIMITATIONS	4-5
1.1.3 APPLICATIONS	6
1.2 MELTING GELS	
1.2.1 BACKGROUND	6-8
1.2.2 LITERATURE REVIEW	9-11
1.2.3 APPLICATIONS	11
1.3 WAX-BASED PHASE CHANGE MATERIALS	
1.3.1 BACKGROUND	12-13
1.3.2 SOL-GEL COMPOSITES	13-14
1.3.3 APPLICATIONS	15
1.4 MELTING GEL-WAX COMPOSITE OBJECTIVES	15-16
II. METHOD OF ATTACK	16-17
III. EXPERIMENTAL TECHNIQUE	
3.1 GEL SYNTHESIS	17-19
3.2 SAMPLE PREP	
3.2.1 MONOLITHIC COATINGS	19-21
3.2.2 CAPACITOR ASSEMBLY	21-22
3.3 SAMPLE CHARACTERIZATION	
3.3.1 PROFILOMETRY	22-23
3.3.2 OPTICAL MICROSCOPY	23-24
3.3.3 SEM ANALYSIS	24
3.3.4 DIELECTRIC CHARACTERIZATION	24-26

IV. RESULTS	
4.1 PROFILOMETRY	26-30
4.2 OPTICAL MICROSCOPY	
4.2.1 REPRESENTATIVE MICROGRAPHS	31-35
4.2.2 THERMALLY DEGRADED SAMPLES	35-37
4.2.3 PARTICLE SIZE ANALYSIS	37-48
4.3 SEM ANALYSIS	
4.3.1 REPRESENTATIVE MICROGRAPHS	48-52
4.3.2 PROFILOMETRY SAMPLE	53-55
4.3.3 PARTICLE SIZE ANALYSIS	55-62
4.3.4 COMPARISON WITH OPTICAL PARTICLE SIZE DISTRIBUTION	63-67
4.4 DIELECTRIC CHARACTERIZATION	
4.4.1 DIELECTRIC BEHAVIOR OF WAX-GELS	67-73
4.4.2 EFFECT OF THERMAL TREATMENTS	73-76
V. DISCUSSION	
5.1 PROFILOMETRY	76-77
5.2 OPTICAL MICROSCOPY	
5.2.1 REPRESENTATIVE MICROGRAPHS	77-78
5.2.2 THERMALLY DEGRADED SAMPLES	78
5.2.3 PARTICLE SIZE ANALYSIS	78-80
5.3 SEM ANALYSIS	
5.3.1 REPRESENTATIVE MICROGRAPHS	80
5.3.2 PROFILOMETRY SAMPLE	80
5.3.3 PARTICLE SIZE ANALYSIS	81
5.3.4 COMPARISON WITH OPTICAL PARTICLE SIZE DISTRIBUTIONS	81-82
5.4 DIELECTRIC CHARACTERIZATION	
5.4.1 DIELECTRIC BEHAVIOR OF WAX-GELS	82-83
5.4.2 EFFECT OF THERMAL TREATMENTS	83-84
VI. SUMMARY AND CONCLUSIONS	84-85
VII. SUGGESTIONS FOR FUTURE WORK	

7.1 CHARACTERIZATION	85-86
7.2 SYNTHESIS	86-87
7.3 THERMAL APPLICATIONS	87-88
7.4 ELECTRO-OPTICAL APPLICATIONS	88-89
7.5 OTHER APPLICATIONS	89
VIII. REFERENCES	90-95
IX. APPENDIX	96-107

LIST OF TABLES

<u>TABLE</u>	<u>PAGE</u>
Table 1: List of Common Alkoxysilane Melting Gel Precursors	9
Table 2: Tabulated Amounts Used To Synthesize Melting Gel-Wax Composites	18
Table 3: Par-Gel Tabulated Statistics of Roughness Parameters	30
Table 4: Micro-Gel Tabulated Statistics of Roughness Parameters	30
Table 5: Two sample Kolmogorov–Smirnov tests of Wax-gel optical particle sizes	40
Table 6: Parameters of CDF Best Fits for Wax-gel Optical Particle Size EDFs	45-46
Table 7: Bounded Gamma Parameter Ranges for Par/Micro-gel Optical Particle Sizes	46
Table 8: Medians of Optical Particle Size Wax-gel CDFs and EDFs	47
Table 9: Bounded Median Ranges for Par/Micro-gel Optical Particle Sizes	47
Table 10: Parameters of CDF Best Fits for SEM Wax-gel Particle Size EDFs	60
Table 11: Bounded Gamma Parameter Ranges for Par/Micro-gel SEM Particle Sizes	60
Table 12: Medians of Optical Particle Size Wax-gel CDFs and EDFs	61
Table 13: Bounded Median Ranges for Par/Micro-gel SEM Particle Sizes	61

LIST OF FIGURES

<u>FIGURE</u>	<u>PAGE</u>
Figure 1: Synthesis Flowchart For Producing Melting-Gel Wax Composites	19
Figure 2: Monolithic gel coating (right) with foil mold imprint (left)	20
Figure 3: Monolithic gel coatings on glass slides	20
Figure 4: Acetone-polished capacitor gel sample	22
Figure 5: Typical Roughness Profile Data of Melting Gel	26
Figure 6: Micro-Gel Surface Features Captured By Profilometer Video Feed	27
Figure 7: Par-Gel Surface Features Captured By Profilometer Video Feed	27
Figure 8: Ra and TIR-wax vol% rug plots of Par-gels (n = 30 each, Linear R ²)	29
Figure 9: Ra and TIR-wax vol% rug plots of Micro-gels (n = 30 each, Linear R ²)	29
Figure 10: Optical Micrograph of 5.2 vol% Par-Gel (40x)	31
Figure 11: Optical Micrograph of 9.7 vol% Par-Gel (40x)	32
Figure 12: Optical Micrograph of 17.6 vol% Par-Gel (40x)	32
Figure 13: Optical Micrograph of 5.2 vol% Micro-Gel (40x)	33
Figure 14: Optical Micrograph of 9.7 vol% Micro-Gel (40x)	34
Figure 15: Optical Micrograph of 17.6 vol% Micro-Gel (40x)	34
Figure 16: 40x Micrographs of 5.2% Par-gel/Micro-gel after 4 days at 200°C	35
Figure 17: 17.6% Par-gel before (right) and after (left) 7 days at 180°C	36
Figure 18: UV illumination of 17.6% Par-gel before and after 7 days at 180°C	36
Figure 19: 100x micrographs of post-degraded 17.6% Par-gel across gradient	37

Figure 20: EDF of all Wax-gel optical particle sizes (n = 3564)	38
Figure 21: EDFs of Par-gel and Micro-gel optical particle sizes	38
Figure 22: EDFs of Par-gel optical particle sizes across various wax contents	39
Figure 23: EDFs of Micro-gel optical particle sizes across various wax contents	39
Figure 24: Histogram of All Pooled Wax-gel Optical Particle Sizes	41
Figure 25: Semi-log EDF plot of all Wax-gel optical particle sizes	42
Figure 26: Par-gel Optical Particle Size Best Fits	44
Figure 27: Micro-gel Optical Particle Size Best Fits	45
Figure 28: Gamma Parameters for Par-gel and Micro-gel Optical Particle Sizes	48
Figure 29: Median Ranges for Par-gel and Micro-gel Optical Particle Sizes	48
Figure 30: Representative Melting Gel SEM Micrograph	49
Figure 31: SEM Micrograph of 5.2 vol% Par-Gel	50
Figure 32: SEM Micrograph of 9.7 vol% Par-Gel	50
Figure 33: SEM Micrograph of 17.6 vol% Par-Gel	51
Figure 34: SEM Micrograph of 5.2 vol% Micro-Gel	51
Figure 35: SEM Micrograph of 9.7 vol% Micro-Gel	52
Figure 36: SEM Micrograph of 17.6 vol% Micro-Gel	52
Figure 37: 5000x SEM Micrograph of 17.6 vol% Micro-Gel Profilometry Sample	53
Figure 38: 20,000x SEM Micrograph of 17.6 vol% Micro-Gel Profilometry Sample	54
Figure 39: 16,500x SEM Micrograph of 17.6 vol% Micro-Gel Profilometry Sample	54
Figure 40: EDF of all SEM Wax-gel particle sizes (n = 1774)	55

Figure 41: EDF of SEM Par/Micro-gel particle sizes	56
Figure 42: EDF of SEM Par-gel particle sizes across various volume percents	56
Figure 43: EDF of SEM Micro-gel particle sizes across various volume percents	57
Figure 44: Histogram of all pooled SEM wax-gel particle sizes	57
Figure 45: Par-gel SEM Particle Size Best Fits	58
Figure 46: Micro-gel SEM Particle Size Best Fits	59
Figure 47: Gamma Parameters for Par-gel and Micro-gel SEM Particle Sizes	62
Figure 48: Median Ranges for Par-gel and Micro-gel SEM Particle Sizes	62
Figure 49: Par-Gel Optical-SEM Model Comparison	64
Figure 50: Micro-Gel Optical-SEM Model Comparison	65
Figure 51: Representative Wax-gel CDF Fits Over Unified Optical-SEM Range	66
Figure 52: Representative Wax-gel PDF Fits Over Unified Optical-SEM Range	66
Figure 53: Best Wax-gel Gamma Volume PDF Fits Over Unified Optical-SEM Range	67
Figure 54: Dielectric Constant Duplicate Measurement Variation of Wax-Gels	68
Figure 55: Dissipation Factor Duplicate Measurement Variation of Wax-Gels	69
Figure 56: Dielectric Constant Replicated Measurement Variation of Wax-Gels	70
Figure 57: Dissipation Factor Replicated Measurement Variation of Wax-Gels	71
Figure 58: Dielectric Constant Measured Ranges of Wax-Gels	72
Figure 59: Dissipation Factor Measured Ranges of Wax-Gels	72
Figure 60: dk/dt variation of wax-gels during cumulative thermal cycling	74

Figure 61: Dissipation factor variation of wax-gels during cumulative thermal cycling

75-76

LIST OF APPENDICES

<u>APPENDIX</u>	<u>PAGE</u>
Appendix 1: Pooled Ra and TIR values plotted against AVG (n = 210, Linear R ²)	96
Appendix 2: Pooled TIR and Ra Correlation (n = 210, Power Model R ² Fit)	97
Appendix 3: TIR-Ra Clusters of Par/Micro-Gels (n = 90, each)	98
Appendix 4: Optical Micrograph of 5.2 vol% Par-Gel (100x)	99
Appendix 5: Optical Micrograph of 9.7 vol% Par-Gel (100x)	100
Appendix 6: Optical Micrograph of 17.6 vol% Par-Gel (100x)	101
Appendix 7: Optical Micrograph of 5.2 vol% Micro-Gel (100x)	102
Appendix 8: Optical Micrograph of 9.7 vol% Micro-Gel (100x)	103
Appendix 9: Optical Micrographs of 17.6 vol% Micro-Gel (100x)	104
Appendix 10: Pooled Wax-gel Optical Particle Size Best Fits	105
Appendix 11: Pooled Wax-gel SEM Particle Size Best Fits	106
Appendix 12: Pooled Wax-Gel Optical-SEM Model Comparison	107

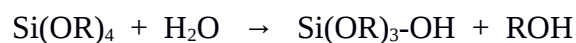
I. INTRODUCTION

1.1 SOL-GEL PROCESSING

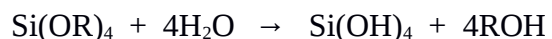
1.1.1 BACKGROUND

Sol-gel processing is a general classification for organometallic, wet-chemistry techniques that produce solid materials from solutions of chemical precursors. Specifically, these chemical solutions of monomers or colloids are polymerized into three-dimensional networks of gel. Subsequently, these gels are dried into solid materials. Due to the aqueous nature of these reactions, sol-gel processes readily produce metal oxides (i.e. glasses and ceramics) directly from solution. Hence, the chemical precursors used to produce these metal oxides are generally metal alkoxides; these are metals with bridging oxygens between two or more alkyl groups.^[1]

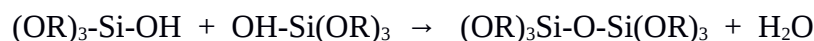
For example, silica gel is commonly produced from TEOS (Tetraethyl orthosilicate). With the addition of water to TEOS, the ethoxy groups are hydrolyzed. This generates a hydroxyl group on the metal alkoxide and liberates an ethanol molecule. This hydrolysis reaction can be generalized in the following form, where “R” can be any alkyl group:



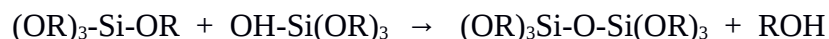
If this reaction continues to completion such that all the alkoxy groups of the metal alkoxide becomes fully hydrolyzed, the resulting products become solely a mixture of silicic acid and alcohols:



Instead, by partially hydrolyzing the metal alkoxide species, condensation reactions between these precursor molecules can be facilitated to produce oligomers. Depending on the interacting functional groups, this condensation reaction can be expressed in the following chemical reactions:



or



These specific condensation reactions are mediated by protons or hydroxide ions in aqueous solution. In general, the higher the concentration of these ions, the faster the overall reaction kinetics of the system. However, the structure of the polymers formed by these two ions are vastly different.^[2]

For instance, positive partial charges of the hydroxyl sites tend to attract hydroxide ions closely such that nearly all possible sites have reacted. This results in discrete particles grow into “tumbleweed” type structures. Contrastingly with protons, fewer

number of sites condense and produce longer, lower-coordinated “spaghetti” structures. These nanoscale differences between the structures of condensing oligomers results in macroscopic differences in the final sol-gel products. Under basic conditions, colloids/nanoparticles are synthesized, while acidic conditions generate a continuous network of gel. Regardless of the pH, after all the oligomers have polymerized together, the final product is metal oxide gel suspended in alcohol/water.^[3]

Once the reaction is complete, to obtain solid monoliths or coatings from the metal oxide gel, further processing is required. Specifically, the solvent must be removed from the gel. Since these reactions occurred under an aqueous environment, micro-nanoscale porosity intrinsically exists within the gel and act effectively as capillaries for solvent. By evaporating solvent, strong capillary forces act along the drying front and can easily supersede the strength of metal oxide. Therefore, slow and careful evaporation is generally required to obtain crack-free solids from most conventional sol-gel processing.

[4]

This careful drying procedure however can be bypassed by transforming sol-gels into aerogels through supercritical drying. Generally, CO₂ is used as a solvent and the temperature/pressure of the system is manipulated to obtain a supercritical fluid. As a supercritical fluid, there is effectively no surface tension between liquid and vapor phases. Thus, evaporation of the solvent from the gel can be accomplished without the shrinkage normally associated with surface tension. Consequently, this preserves the

intrinsic nanoporosity of the gel state without cracking. These aerogels are the lightest materials ever developed (>98% air) and possess legendary properties: including high specific modulus, low thermal conductivity, low dielectric constant/loss, and high specific surface area.^[5]

1.1.2 ADVANTAGES AND LIMITATIONS

The sol-gel process offers many unique advantages that distinguishes it from many other conventional materials processing methods. For instance, since the sol-gel process is a “bottom-up” process, composition and structure can be directly engineered from the molecular scale all the way to the macroscale as gelation evolves. By mixing various ratios of different chemical precursors and controlling processing variables (i.e. pH, temperature, and time), an extremely wide range of tunable properties can be achieved. Additionally, by using highly refined chemicals, ultra-high purity materials can be derived. Furthermore, these materials are derived with minimal energy consumption, as the processing can be done between room temperature and the modest temperatures of a simple hot plate.^[6]

Moreover, perhaps the greatest advantage of sol-gel processing is its ability to compatibilize organic and inorganic materials together. For example, sol-gels can be directly coated onto virtually any substrate; this allows for inorganic, refractory materials to be deposited onto organic substrates without exposing them to damagingly high

temperatures. Likewise, these inorganic gels can be loaded with organic materials or used to coat organic payloads with inorganic shells to produce organic-inorganic microcomposites. Lastly, these metal oxide gels can be hybridized in-situ to achieve nanocomposites that otherwise cannot be produced by any other means. This is accomplished by choosing precursors with non-reactive, organic functional groups that allow the hydrolysis/condensation reactions to continue unimpeded, but leave behind organic ligands attached to the metal oxide backbone. No other materials processing method can feasibly achieve this molecular level, organic-inorganic mixing that sol-gel processing offers with these functionalized metal oxide gels.^[7]

Despite all these unique benefits, sol-gel processing still presents a few significant challenges. Firstly, only metal oxides can be directly synthesized from sol-gel chemistry. However, post-processing can extend this into other material systems. For example, auto-ignition pyrolysis of sol-gel products has produced carbides and advanced carbon composites. Additionally, carbothermal reduction and ammonia reactions have successfully produced borides, nitrides, and oxynitrides from sol-gel products. Also, it is intrinsically difficult to develop large, monolithic pieces from sol-gel processing due to the significant gel shrinkage. Ergo, sol-gels are best implemented as aerogels or under confined dimensions: such as thin films, fibers, or particles. Lastly, to achieve fully dense glasses or ceramics, further heat treatments are generally required to eliminate the intrinsic porosity.^[1]

1.1.3 APPLICATIONS

Sol-gels are used in a variety of advanced material applications. For example, in the form of colloids/nanoparticles, sol-gels are used for biomedical/pharmaceutical treatments, specialty polishing compounds, high temperature binders, catalysts, desiccants, synthetic opals, and a variety of other uses. When drawn as a fiber or lens, sol-gels have special use for optical waveguides because of their high purity and ability to host rare earth, lasing ions. If deposited as a thin film, sol-gel coatings are especially utilized for their superior scratch-resistance and corrosion protection. Hence, they are commonly used as barriers for oxidation-sensitive metals (e.g. Mg-alloys) and battery materials. Also, sol-gel films have been used for anti-reflective, bio-compatible, and superhydrophobic coatings. Lastly, in the form of aerogels, they are used across various applications such as thermal insulation, optical diffusers, filtration, catalysts, battery electrodes, supercapacitors, sensors, and hypervelocity particle traps.^{[1-2],[7-9]}

1.2 MELTING GELS

1.2.1 BACKGROUND

Historically, the first organically modified silicates were developed in the early 20th century in the form of silicones. These silicones were simple siloxane polymers that were functionalized with organic groups; they came in a wide range of forms, such as oils, rubbers, and resins. Compared to traditional organic polymers, these silicones have

always been prized for sharing the beneficial, inorganic properties of silica (i.e. high thermal stability and chemical inertness) with the flexible, low temperature processing of organic materials. Nevertheless, pure silicones possess several significant challenges. For instance, their extraordinarily low surface tension makes adhesion with substrates extremely difficult and are notorious for spreading molecular contamination through direct contact to sensitive materials (e.g. electronics, optics, and bonding surfaces). Furthermore, their high viscoelasticity, outgassing, and gas permeability prevents their use in vacuum, pressurized, or contamination sensitive environments.^[10-11]

Using sol-gel processing, greater tunability of properties could be gained, while attaining the advantages of silicones without inheriting their limitations. This is done by using functionalized metal alkoxides (alkoxysilanes) to polymerize gels. These gels are called ORMOSILs, or “organically-modified siloxanes”, and are examples of hybrid, organic-inorganic nanocomposites. There are two classification types of hybridization for organic-inorganic nanocomposites. Type I hybrids use secondary bonding between organic/inorganic components, while type II involves covalent bonding between them. Hence, ORMOSILs are type II organic-inorganic hybrid nanocomposites.^[12]

A special class of ORMOSILs are “melting gels”, which are characterized by their unique softening behavior. They are derived from a combination of mono-substituted and di-substituted alkoxysilanes, where the prefix refers to the number of non-reactive groups. These non-reactive groups do not hydrolyze, as they are organic functional

groups covalently bonded to silicon, forming very strong Si-C bonds. The “melting” associated with these melting gels is neither a classical thermodynamic melting or thixotropic rheological behavior. Instead, this softening is a relaxation process due to the lack of sufficient crosslinks stabilizing the gel network. This melting process is reversible for practically an infinite number of cycles. However, after exceeding a critical point known as the consolidation temperature ($\sim 130\text{-}180^\circ\text{C}$), the gel cures into a rigid solid that can no longer melt. This is similar to a thermoset, where crosslinks form at a sufficiently high temperature, but is comparably less exothermic. This ability to thermally cure at low temperatures is highly advantageous because there is no shrinkage and no risk of cracking. Meanwhile, conventional sol-gels must be carefully dried and undergo significant shrinkage.^[13]

Being a sol-gel, it would be expected that these melting gels should exhibit significant nanoporosity from aqueous processing. However, most surprisingly, consolidated melting gels actually form non-porous, hermetic structures. Although the exact mechanisms for this phenomena are still being investigated, it is currently theorized that the non-reactive functional groups orient themselves in such a way that blocks nanopores. Overall, the properties of these melting gels seem to defy the norms of traditional sol-gels and offer new, exciting opportunities to create hybrid nanocomposites with remarkable properties and robust processing capabilities.^[14]

1.2.2 LITERATURE REVIEW

Given that melting gels are defined by the non-reactive group ratio of their constituent precursors, melting gel compositions are only limited by the alkoxysilane precursors that are available. Based on the literature, the most common organic functional groups on alkoxysilanes used for synthesizing melting gels have been aliphatics and aromatics. A comprehensive list of common alkoxysilane precursors used to make melting gels is provided below in **Table 1**.^[13]

Precursor Name	Chemical Formula	Number of Non-Reactive Groups	% SiO ₂
Dimethyldiethoxysilane (DMDES)	C ₆ H ₁₆ O ₂ Si	2	40.5
Methyltriethoxysilane (MTES)	C ₇ H ₁₈ O ₃ Si	1	33.7
Dimethyldimethoxysilane (DMDMS)	C ₄ H ₁₂ O ₂ Si	2	50.0
Methyltrimethoxysilane (MTMS)	C ₄ H ₁₂ O ₃ Si	1	44.1
Diphenyldiethoxysilane (DPhDES)	C ₁₆ H ₂₀ O ₂ Si	2	22.1
Phenyltriethoxysilane (PhTES)	C ₁₂ H ₂₀ O ₃ Si	1	25.0
Diphenyldimethoxysilane (DPhDMS)	C ₁₄ H ₁₆ O ₂ Si	2	24.6
Phenyltrimethoxysilane (PhTMS)	C ₉ H ₁₄ O ₃ Si	1	30.3
Vinyltriethoxysilane (VTES)	C ₈ H ₁₈ O ₃ Si	1	37.2
Tetraethoxysilane (TEOS)	C ₈ H ₂₀ O ₄ Si	0	28.8
Tetramethoxysilane (TMOS)	C ₄ H ₁₂ O ₄ Si	0	39.5

Table 1: List of Common Alkoxysilane Melting Gel Precursors^[13]

By choosing different pairs of mono/di-substituted precursors and varying their relative molar ratios, a wide range of melting gel properties can be achieved. For example, as the relative amounts of di-substituted precursors increases, the crosslinking density and glass transition temperature decreases, but the consolidation temperature increases. With greater relative amounts of mono-substituted precursors or TEOS/TMOS, the opposite trend occurs. Similarly, as the relative amount of aromatic-substituted precursors increases, the glass transition temperature increases, but the crosslinking density and consolidation temperature decreases. Furthermore, methoxysilane precursors produce melting gels with higher glass transition temperatures than ethoxysilanes. This arbitrary tunability in glass transition temperature and crosslinking density is important for obtaining gels with optimized physical properties, such as hardness, density, refractive index, and thermal stability. Likewise, consolidation temperatures are optimized for the type of processing and substrates on which melting gels are attached.^[15-16]

Differences in precursor functional groups not only affects melting gel properties, but their processing as well. For instance, the electron delocalization of phenyl groups helps auto-catalyze condensation reactions. Meanwhile, aliphatic-substituted precursors generally need a separate catalyst to be added to solution in order to achieve the same reaction rates as phenyl-substituted precursors. This catalyst acts as an impurity and needs to be removed from the melting gel. Phenyl-substituted precursors also have the advantage of producing melting gels with higher hydrophobicity than aliphatic-substituted precursors. Nevertheless, the lower silica content of the phenyl-substituted

precursors significantly diminishes the thermal stability of melting gels compared to aliphatics. Lastly, vinyl-phenyl melting gels are special in that they are the only ones that have demonstrated enhanced UV curing capabilities.^[13-15]

1.2.3 APPLICATIONS

These melting gels exhibit the desirable properties of a traditional sol-gel hybrid nanocomposite, but with ease of processing associated with a conventional epoxy. For instance, they possess attractive optical properties such as high visible transparency and UV absorption/stability. Likewise, as a dielectric, melting gels are excellent low k, low loss materials with high electrical resistivities and breakdown voltages. Furthermore, as a barrier to gases/liquids, their superior chemical stability, hermeticity, and adhesion are among the best for curable material systems. However, unlike organic thermosets, melting gels are refractory and fire-resistant, surviving temperatures exceeding 800°C. Despite all these benefits, these materials are currently still mostly in the R&D phase and have not been commercially mass produced yet. However, substantial academic and industrial efforts are being undertaken to make melting gels feasible for various applications, such as LED encapsulants, high temperature bonding, low-k interconnect coatings, planar waveguides, anti-graffiti coatings, and corrosion barrier films for metals.

[13-16]

1.3 WAX-BASED PHASE CHANGE MATERIALS

1.3.1 BACKGROUND

The term “wax” refers to a general group of lipophilic, organic compounds that are solid at room temperature and exhibit relatively low melting points ($< 100^{\circ}\text{C}$).

Historically, they are among the oldest materials used by mankind and are still utilized ubiquitously in everyday items such as candles, crayons, cosmetics, lubricants, and binders. Waxes have always been extracted from four major resources: plants, animals, minerals, and petroleum. All of these resources produce highly complex, multicomponent mixtures of various organic compounds. However, by far the most commercially produced and purest extracted waxes are petroleum based. Although synthetic waxes are considerably purer, they are significantly more expensive and generally used in smaller quantities for niche products.^[17]

The two major petroleum waxes that are separated from crude oil extraction include paraffin and microcrystalline wax. Both are composed of the same types of hydrocarbons, such as n-alkanes, iso-alkanes, and naphthenes. Nonetheless, the relative ratios of these components are significantly different between these two waxes. Paraffin wax contains mostly linear n-alkanes, while microcrystalline wax contains more branched iso-alkanes. These differences in relative hydrocarbon compositions lead to significant differences in physical properties.^[18-19]

Regardless of the wax type, they all share relatively low melting points and high enthalpies of melting. Consequently, this recommends their use as organic phase change materials (PCMs). The term “PCM” generally refers to any material system that utilizes the property changes associated with a phase transition to carry out useful work. However, in this context, PCM refers to a material using thermal phase changes to store/release energy in the form of latent heat. These thermal PCMs are generally distinguished between organic and inorganic materials.^[20]

Inorganic PCMs rely on the dissolution/crystallization of salt hydrates, while organic PCMs use the melting/freezing of waxes to control latent heat storage. Although inorganic PCMs have higher volumetric latent heat capacities and thermal conductivities than organic PCMs, they have two major drawbacks. Firstly, their change in volume is drastically high, which can easily stress and fracture many host materials. Secondly, that they often supercool to the point where they do not self-nucleate. To circumvent this, nucleating agents are added, but generally have a limited number of cycles before they no longer are active. Nevertheless, organic PCMs do not have these same issues, but are vulnerable to thermal degradation if overheated. This can be mitigated by micro-nanoscale encapsulation of organic PCM phases, which significantly increases the effective thermal degradation temperature of the wax.^[21]

1.3.2 SOL-GEL COMPOSITES

Micro-encapsulated, organic PCMs are currently produced through two methods: conventional polymer processing and sol-gel processing. Mixing molten wax into thermoplastics/thermosets is trivial and effective for producing very large, inexpensive PCM components. However, their composite properties are strictly limited to the polymer host, whose hermeticity, thermal conductivity, and thermal stability are generally quite poor. On the other hand, sol-gel processing enables organic PCM composites to be developed in an inorganic host, combining superior inorganic properties with the built-in PCM functionality of encapsulated wax.^[22]

For sol-gel processing, there are two approaches to developing PCM composites. One approach is to harness the vast open porosity of sol-gels (esp. aerogels) by infiltrating it with wax. This allows large PCM composites with high wax loadings to be obtained; however, this continuous phase PCM requires the extra, critical step of capping. If compromised, damage to any part of the seal can lead to significant leakage of the infiltrated wax. The second approach is to emulsify the wax with surfactants in-situ during the gelation process. This creates micro-confined, dispersed wax phases within the gel matrix. This dispersion can be turned into a PCM powder, where organics are coated in an inorganic shell, or left in the gel as a PCM composite. Either way, this micro-confinement increases the thermal stability and effective thermal conductivities of the wax compared to infiltrated sol-gel PCMs. Moreover, damage to one part of a PCM does not lead to any connected leakage from the rest of the encapsulated wax.^[22-24]

1.3.3 APPLICATIONS

In terms of thermal applications, PCMs have been essential for passive thermal cooling systems, efficient thermoelectric devices, and thermal energy storage. For example, PCMs have been extensively used in advanced electronics cooling, aerospace heat exchangers, geothermal pipes, and solar energy harvesting. In the form of encapsulated microparticles, PCM powders are often loaded into engineering plastics, plaster, cement, and asphalt to improve their thermal performance.^[25-29]

In addition, by applying an electric field to molten wax and allowing it to freeze, the induced dipoles remain aligned. This creates an “electret”, which is analogous to a magnet, but instead radiates a static electric field. Electrets are actively used in many commercial applications, such as acoustic microphones, vibrational energy harvesting, radiation dosimeters, and gas filtration systems.^[30-31]

1.4 MELTING GEL-WAX COMPOSITE OBJECTIVES

With the unique processing capabilities and physical properties of melting gels, there is significant motivation for developing new, wax-melting gel PCM composites. Hence, there are two primary objectives for this research. Firstly, to develop an effective synthesis procedure for feasibly producing stable wax-melting gel composites. Secondly, to characterize the physiochemical nature of the produced wax-melting gel composites. As a preliminary, exploratory investigation, the composite structure was profiled across various length scales and dimensions. Based on these findings, suitable applications and

applicable analog systems were identified for these melting gel-wax composites. That way, this work may be used as a platform for future development of melting gel composites filled with organic payloads.

II. METHOD OF ATTACK

Without additives, wax is naturally immiscible in unconsolidated melting gel. Hence, consolidation of pure melting gel-wax mixtures leads to significant phase segregation. Therefore, it was determined that the most effective strategy for achieving mixture stability would be to introduce the wax in-situ during gel synthesis with an appropriate surfactant. Empirically, the best performing surfactant was found to be Dow Corning 56 Additive. This is a silicone-based surfactant that demonstrated both superior emulsification and thermal stability during the consolidation heat treatments. As a result, stabilized melting gel-wax emulsions were successfully obtained for both paraffin and microcrystalline waxes.

To study the effect of wax content on the composite structure/properties, a standard melting gel system was chosen and loaded with three different wax volume fractions. The gel standard used was a phenyl-based melting gel composed of 90 mol% PhTES and 10 mol% DPhDES. This particular composition was chosen for its simple, robust processing and well-documented physical properties. After sol-gel processing, gravimetric

measurements indicated that the compositions of wax weight percents obtained were 3.6, 6.9, and 12.9 wt%. Assuming the specific gravity of the gel was 1.30 and 0.90 for the wax respectively, this translates to wax volume percents of 5.2, 9.7, and 17.6 vol% accordingly. It was observed the density change from consolidation and wax evaporation were negligible; hence, these measured wax contents are representative of the consolidated composite gel values. Subsequently after consolidation, composite gel samples were analyzed with four different characterization techniques: contact profilometry, optical microscopy, SEM analysis, and dielectric spectroscopy. These techniques were employed to gain a holistic, preliminary understanding of the structure and interactions between the components across various perspectives.

III. EXPERIMENTAL TECHNIQUE

3.1 GEL SYNTHESIS

All chemical precursors used were purchased in high purity from Gelest and Sigma-Aldrich. In addition, the consumer-grade paraffin and microcrystalline waxes used were procured from local candle vendors (Candles and SuppliesTM; Quakertown, PA). The amounts of each raw material used are summarized below in **Table 2**.

	PhTES	DPhDES	EtOH	H ₂ O	HCl (0.1 M)	Surfactant (Dow Corning 56 Additive)	Paraffin/Microcrystalline Wax (5.2, 9.7, 17.6 vol%)		
Mass (g)	2.75	0.35	0.42	0.31	0.01	0.01	0.07	0.14	0.28

Table 2: Tabulated Amounts Used To Synthesize Melting Gel-Wax Composites

As detailed in the literature, the PhTES was first added to deionized water in a 1:1.25 molar ratio that was adjusted to a pH of 2.5 with HCl.^[15] Then the wax was introduced to this mixture with a drop of surfactant. Together, this mixture was left stirring in a closed beaker for 6 hours at ~40°C. Next, the DPhDES was diluted with ethanol in a 1:4 molar ratio and added dropwise into the stirring beaker solution. After another 2 hours stirring at ~40°C, the beaker was left to cool while stirring overnight.

Subsequently, the gel was transferred from the beaker into a vial through manual scrapping and rinses of hot acetone/hexane to extract all residual components. These solvents were then boiled off, leaving only the gel/wax mixture behind in the vial. This vial was placed in an oven for consecutive heat treatments of 70 and 110°C for 24 hours each. A total of seven different wax-gel compositions were produced through this methodology: one control gel and six composite gels, (three wax loadings for two waxes). This entire synthesis process is summarized schematically below in **Figure 1**:

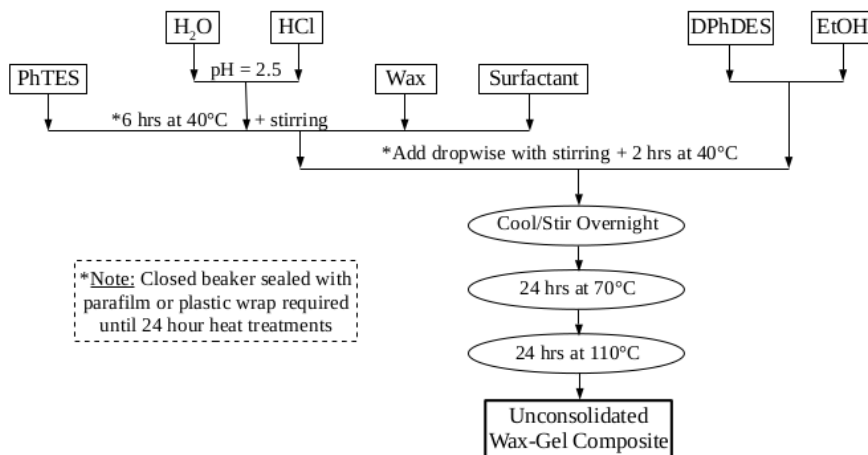


Figure 1: Synthesis Flowchart For Producing Melting-Gel Wax Composites

3.2 SAMPLE PREP

3.2.1 MONOLITHIC COATINGS

For profilometry and optical microscopy, monolithic coatings were casted from the vials of unconsolidated composite gel. For each wax-gel composition, three gel samples were cured onto aluminum foil covered square molds ($\sim 5 \times 5 \times 1$ mm) for 24 hours at $\sim 175^\circ\text{C}$. These film-coated foils were then mounted onto glass slides with wax; this allowed for immobilized, flat surfaces to be effectively probed by the profilometer. After profilometry measurements were collected, the samples were subsequently etched in concentrated HCl to remove the bonded aluminum foil without damaging the gel. After neutralization and thorough ultrasonic cleaning, the samples were placed on glass slides

for optical microscopy. An example of a pristine monolithic gel coating is provided below in **Figure 2**.

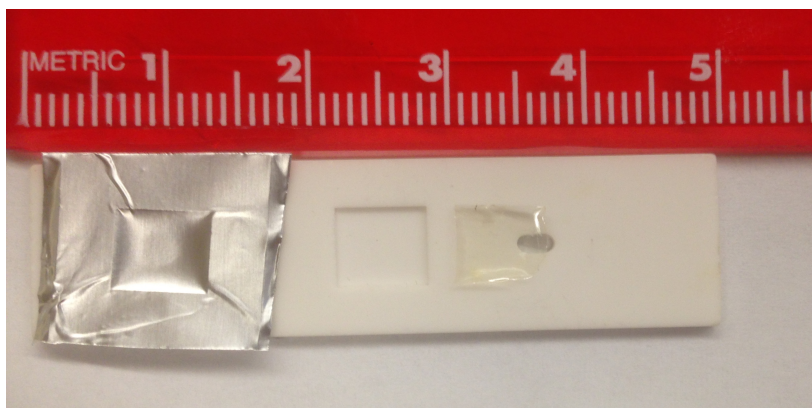


Figure 2: Monolithic gel coating (right) with foil mold imprint (left)

Additional optical samples were cured under the same conditions as the profilometry samples, but directly on soda lime glass slides. Examples of these optical samples are shown below in **Figure 3**.

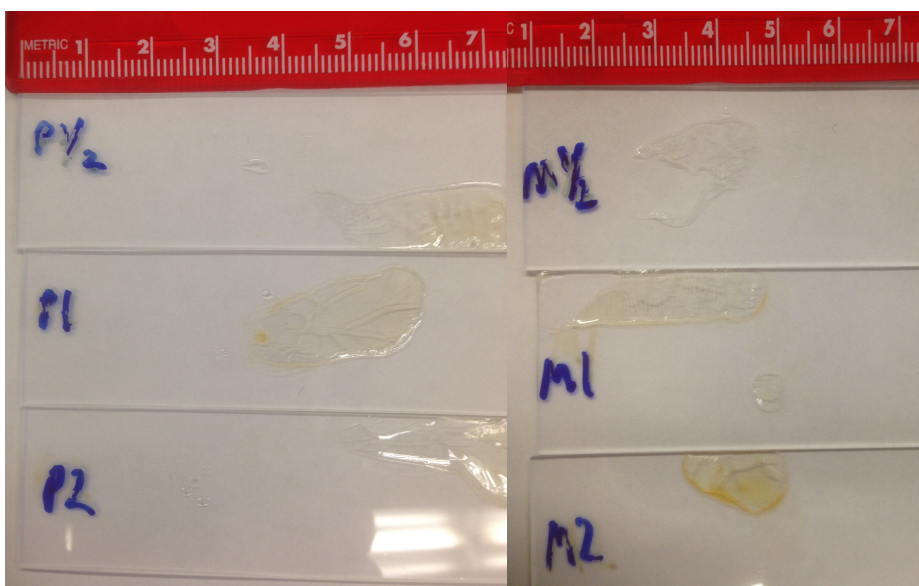


Figure 3: Monolithic gel coatings on glass slides

In **Figure 3**, the letters “P” and “M” correspond to paraffin and microcrystalline composite gels. Also, the numbers “½”, “1”, and “2” correspond to the three wax volume fractions used (5.2, 9.7, 17.6 vol%).

3.2.2 CAPACITOR ASSEMBLY

For each composition of composite gel, circular aluminum discs (CleverDelights™ stamping blanks: ~25.4 mm diameter and 0.58 mm thickness) were coated on each side with gel and heated at ~175°C for about 2 hours. Under these conditions, the gel was viscous and measurably thick (~30-60 μm) capacitor samples could be made. That way, thickness measurement errors could be minimized for more accurate dielectric constant estimates. After being sandwiched together, the samples were heated again at ~175°C for an additional 14 hours in teflon dishes. This cured the gel sufficiently enough to be a rigid solid at elevated temperatures, but just soluble enough in strong solvents to remove residual gel from the electrode sides of the samples. Thus, the electrodes of these “semi-consolidated” samples were acetone polished to ensure greater electrical contact without altering the dielectric specimen. An example of a polished capacitor sample is provided below in **Figure 4**.

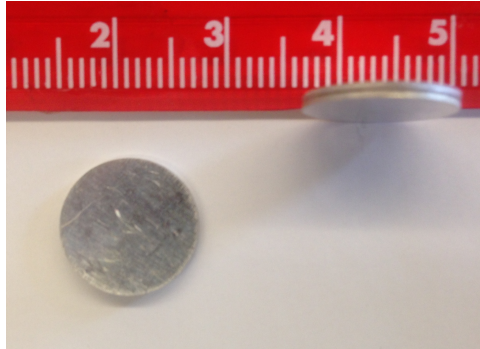


Figure 4: Acetone-polished capacitor gel sample

Once cool, each capacitor sample was measured with a digital micrometer to determine their thickness. After dielectric measurements were complete, samples were cracked open with a hammer. Their pulverized fragments were then carefully stuck onto carbon tape and mounted onto SEM stubs. After blowing off loose particles with compressed air, these samples were then sputter coated with a ~ 10 nm layer of gold for SEM analysis.

3.3 SAMPLE CHARACTERIZATION

3.3.1 PROFILOMETRY

The profilometer used was a Tencor Alpha-Step 200, which was equipped with a 5 mg, $5\ \mu\text{m}$ tip. Measurements were done $k\text{\AA}$ mode, giving a vertical resolution of $5\ \text{\AA}$ and lateral resolution of $40\ \text{nm}$. Ten scans of $80\ \mu\text{m}$ probing length, with sampling density of $25\ \text{s}/\mu\text{m}$ and $0.2\ \mu\text{m}$ step resolution, were performed onto each aluminum foil sample. The points measured on the surface were chosen quasi-randomly, where they were spaced

out as evenly as possible, while avoiding the steep edges of the aluminum foil cavity perimeter. Likewise, extra care was taken to avoid cracks during scans such that only gel-specific features were detected.

Every measured scan was recorded with a corresponding set of roughness parameters: Ra, TIR, and AVG. Ra is the arithmetic average surface roughness, which indicates the mean absolute deviation from the baseline along the sampling path. TIR or “total indicator reading” quantifies the difference between the max and min heights recorded over the scan length. AVG refers to the average height from all of the data points collected over the scanning path. Together, these three parameters help describe and compare the nanoscale roughness between samples, without requiring complex Fourier or fractal analysis of the raw profilometry data.^[32]

3.3.2 OPTICAL MICROSCOPY

A standard optical microscope was used at a 40x and 100x total magnification for imaging each sample. Both transparent and dark backgrounds were used to improve the contrast of the white wax particles under intense illumination. Additionally, various different microstructural features were observed and identified for each sample. After visually scanning the entire sample and taking representative micrographs, these images were processed by ImageJ to statistically analyze the wax particles size and distribution. Thresholding was done carefully using the available SOP guidelines to avoid artifacts and isolate only real wax particles. Particle sizes were estimated by converting particle areas

into effective spherical particle radii. Due to the low aspect ratios of all the identified particles, this assumption of spherical wax particles is reasonable. However, given the theoretical resolution limit of the microscope was $\sim 2\text{ }\mu\text{m}$, thresholded particles below $2\text{ }\mu\text{m}$ were excluded from the analysis.

3.3.3 SEM ANALYSIS

The desktop SEM used was a Phenom Pro and high resolution (2048 px) images were taken with a 10 kV e-beam. After each sample was entirely mapped out, representative BSE (backscattered electron) micrographs were taken at 10,000x, 15,000x, and 40,000x magnifications. These images were then processed in ImageJ for particle size analysis. The same thresholding procedures and spherical particle size calculations performed in optical microscopy were repeated again for these SEM micrographs. Given that the theoretical resolution limit of this instrument was about $\sim 100\text{ nm}$, thresholded particles below this value were appropriately truncated.

3.3.4 DIELECTRIC CHARACTERIZATION

The instrument used to measure the dielectric properties of each capacitor sample was an HP 4194A Impedance Analyzer, which had a spectroscopic frequency range of 100 Hz-40 MHz. This impedance analyzer applied a voltage of 10 mV under room temperature conditions ($\sim 20^\circ\text{C}$), with 1 mHz resolution and no more than $\sim 5\%$ instrument error. After calibration, each capacitor was carefully positioned between

electrical contacts such that the most stable readings, with the least parasitic capacitance/loss, were obtained. The parallel plate capacitance (C_p) and dissipation factor (DF) were simultaneously measured at various frequencies (esp. 1 kHz-1 MHz) and recorded with at least 3 stable data points per frequency. During data collection, long integration times with at least 16 data points averaged per sweep were used for each frequency. Furthermore, the first few data points were consistently recorded across each frequency, as significant time dependence and hysteresis was observed at higher frequencies over the course of several minutes.

When an electric field polarizes a dielectric, electrical energy is stored in the form of capacitance. Capacitance is the ability for a dielectric to store charge. For a parallel plate capacitor, capacitance (C_p) is defined in the following equation:

$$C_p = Q/V = \epsilon_0 \epsilon_r \cdot A/d$$

where Q is plate charge, V is the applied voltage, ϵ_0 is the permittivity of free space, ϵ_r is the relative permittivity of the dielectric, A is the cross-sectional area, and d is the thickness. The SI units for capacitance are farads (F), where 1 farad is 1 coulomb per volt. Thus, the real dielectric constant (ϵ_r) can be estimated using the measured capacitance and sample dimensions. Nevertheless, under an oscillating electric field, some of the electric energy is dissipated as heat from the lossy responses of polarization mechanisms. This results in polarization oscillations becoming out-of-phase with the electric field oscillations. To quantify this, the dissipation factor (DF) is used, which is defined in the following equation:

$$DF = \tan\delta = |\epsilon''/\epsilon'|$$

where δ is the phase angle of the impedance vector, ϵ'' is the imaginary component of dielectric constant, and ϵ' is the real component of dielectric constant. The higher the dissipation factor, the greater the dielectric losses per cycle. By multiplying the real dielectric constant and dissipation factor together, the imaginary dielectric constant can be directly calculated as well. With these quantities, the dielectric behavior of these samples can be rigorously characterized.^[33-34]

IV. RESULTS

4.1 PROFILOMETRY

Contact profilometry was used to assess the surface roughness of these wax-gels. Through out many of the scans, sinusoidal peaks of varying wavelength (~ 1 - $10\ \mu\text{m}$) and amplitude (~ 10 - $100\ \text{nm}$) were observed in virtually every gel sample. A typical example of this is found in **Figure 5**.

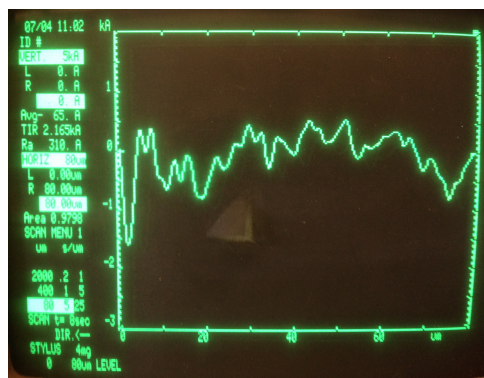


Figure 5: Typical Roughness Profile Data of Melting Gel

However, strong deviations of this nano-roughness were found exclusively in Micro-gel (microcrystalline wax-melting gel) samples, where the wavelength and amplitudes generally increased by at least an order of magnitude. The reason for this disparity was the presence of observed micro-folds/wrinkles on the surface of Micro-gels. As seen in **Figure 6**, these surface features were captured by the built-in optical microscope video feed in the profilometer.

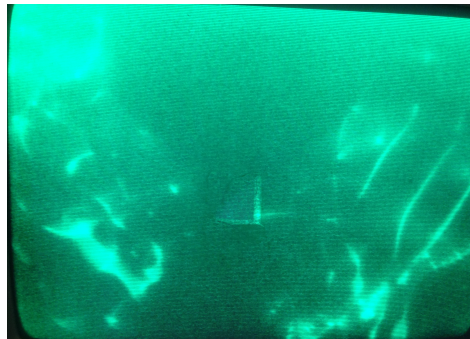


Figure 6: Micro-Gel Surface Features Captured By Profilometer Video Feed

Contrastingly in **Figure 7**, the Par-gels (paraffin wax-melting gel) showed no wrinkles/folds, but instead exhibited circular features.

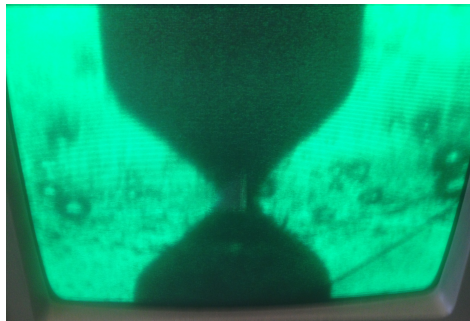


Figure 7: Par-Gel Surface Features Captured By Profilometer Video Feed

Given that the profilometer tip is $\sim 5 \mu\text{m}$, it appears these bubble-like features are roughly commensurate in size to the tip. However, exact feature dimensions can not be extracted

from these images, as the camera is obliquely angled by almost 90 degrees. Furthermore, when scanned, these Par-gel features did not show roughness differences that were distinct from the clear regions. Meanwhile, the scans on the wrinkles/folds of Micro-gels showed obvious roughness differences relative to the featureless regions.

To compare the profilometry roughness data between each sample, three roughness parameters were utilized: Ra, TIR, and AVG. Ra quantifies the mean absolute deviation from the baseline, TIR is the difference between the max and min recorded heights, and AVG refers to the average height from all of the collected data points. In **Appendix 1**, the Ra and TIR values of all gel samples were pooled together and plotted against AVG respectively. Both Ra and TIR showed nearly identical variation in AVG, where higher roughness values contributed to a higher spread in AVG. Since the linear R^2 values were practically zero, it is clear that there was no bias towards ascending or descending slopes during scans. Moreover, that the variation of these roughness parameters generally corresponds to differences in amplitude, given that AVG is invariant to frequency.

As seen in **Appendix 2**, the correlation between Ra and TIR across all the samples is very high. Nonetheless, there is still some unexplained variation between the data and the power model fit. Thus, by using the combination of Ra and TIR values, distinct clusters of roughness parameters can be resolved. These clusters represent a heterogeneous range of measured gel surfaces. For example, in **Appendix 3**, Par-gel and Micro-gel samples can be distinguished from each other as two distinct cluster regions. From this, it is clear

that both Par-gels and Micro-gels overlap significantly in roughness parameters between $Ra \approx 10\text{-}80\text{ nm}$ and $TIR \approx 70\text{-}600\text{ nm}$. However, the Micro-gel cluster extends into relatively higher roughness regions, where $Ra \approx 80\text{-}500\text{ nm}$ and $TIR \approx 600\text{-}1100\text{ nm}$. To break down these clusters by wax content, rug plots of the roughness parameters with respect to wax volume percent were constructed in **Figures 8-9**.

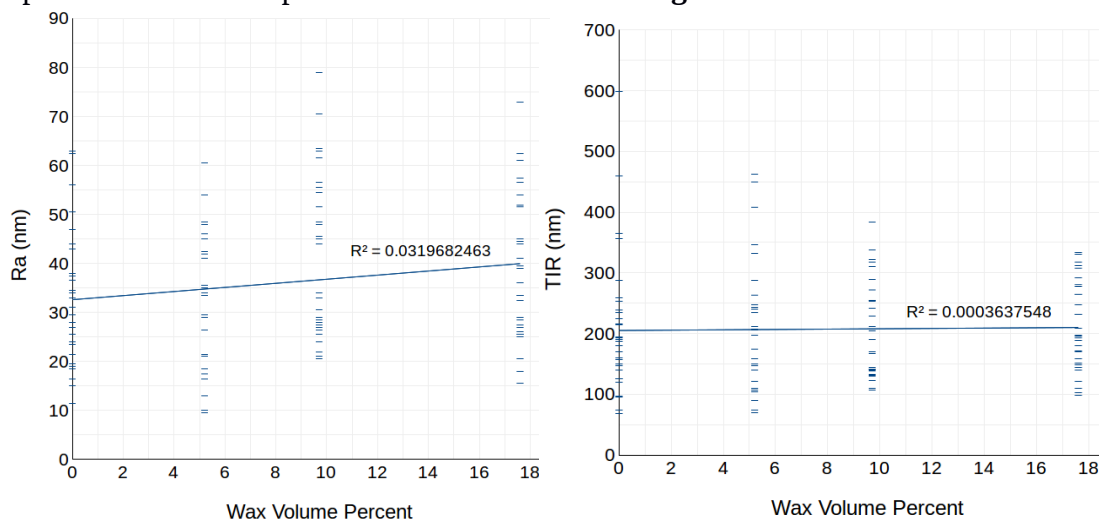


Figure 8: Ra and TIR -wax vol% rug plots of Par-gels ($n = 30$ each, Linear R^2)

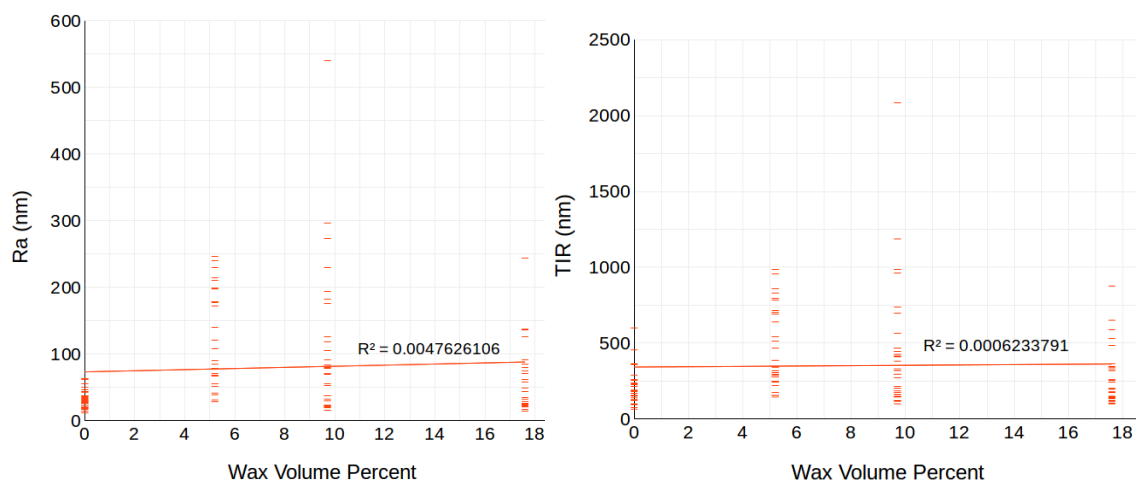


Figure 9: Ra and TIR -wax vol% rug plots of Micro-gels ($n = 30$ each, Linear R^2)

The descriptive statistics of these rug plots are summarized in **Tables 3-4**.

Par-Gel Wax Vol%	0%		5.2%		9.7%		17.6%	
Descriptive Statistic	Ra (nm)	TIR (nm)	Ra (nm)	TIR (nm)	Ra (nm)	TIR (nm)	Ra (nm)	TIR (nm)
Mean	323.2	2094.2	325.4	2013	408	2065.3	383.3	2123
Median	295	1892.5	337.5	1860	335	1972.5	347.5	1970
Stdev	135.1	1142.7	146.9	1114.9	164.6	780.7	147.6	723.8
IQR	143.8	962.5	252.5	1383.8	262.5	1141.3	236.3	1216.3
Range	515	5305	511	3925	585	2760	575	2350

Table 3: Par-Gel Tabulated Statistics of Roughness Parameters

Micro-Gel Wax Vol%	0%		5.2%		9.7%		17.6%	
Descriptive Statistic	Ra (nm)	TIR (nm)	Ra (nm)	TIR (nm)	Ra (nm)	TIR (nm)	Ra (nm)	TIR (nm)
Mean	323.2	2094.2	1183	4788.5	1091.2	4493.2	609.3	2723.5
Median	295	1892.5	870	3682.5	795	3237.5	395	2025
Stdev	135.1	1142.7	724.1	2633.1	1117.7	4158.6	519.3	1869
IQR	143.8	962.5	1205	4252.5	903.8	2943.8	540	1962.5
Range	515	5305	2180	8395	5250	19875	2300	7760

Table 4: Micro-Gel Tabulated Statistics of Roughness Parameters

4.2 OPTICAL MICROSCOPY

4.2.1 REPRESENTATIVE MICROGRAPHS

Optical microscopy was used to characterize the microstructure of these wax-gel composites by exploiting the intrinsic transparency of the gel phase. In **Figures 10-12**, representative 40x micrographs of various Par-gels casted on glass slides were taken. Supplementary 100x micrographs of profilometry Par-gel samples are provided in **Appendices 4-6**, showing greater contrast of the wax particles on a dark filter background; however, the apparent linear scratches are an artifact from the aluminum foil roughness and are not gel features. Each minor tick on the built-in length scale is ~ 50 and ~ 20 μm for the 40x and 100x images respectively.

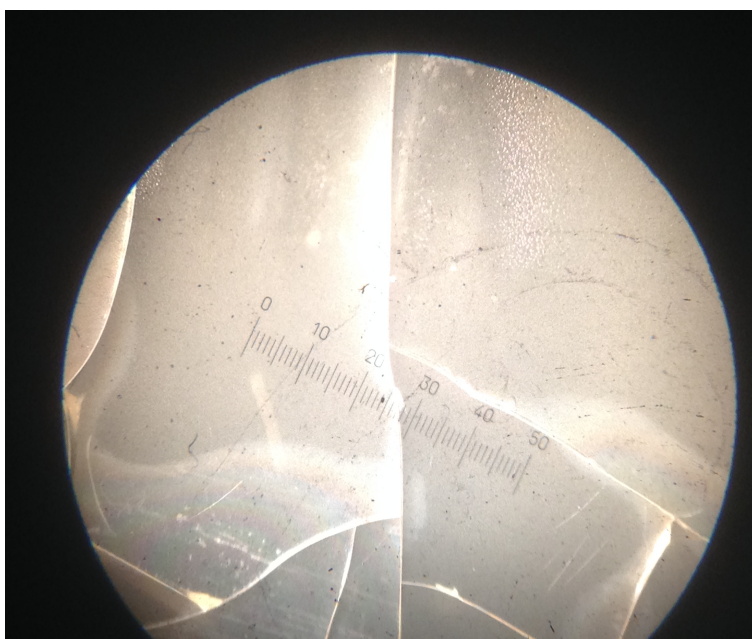


Figure 10: Optical Micrograph of 5.2 vol% Par-Gel (40x)

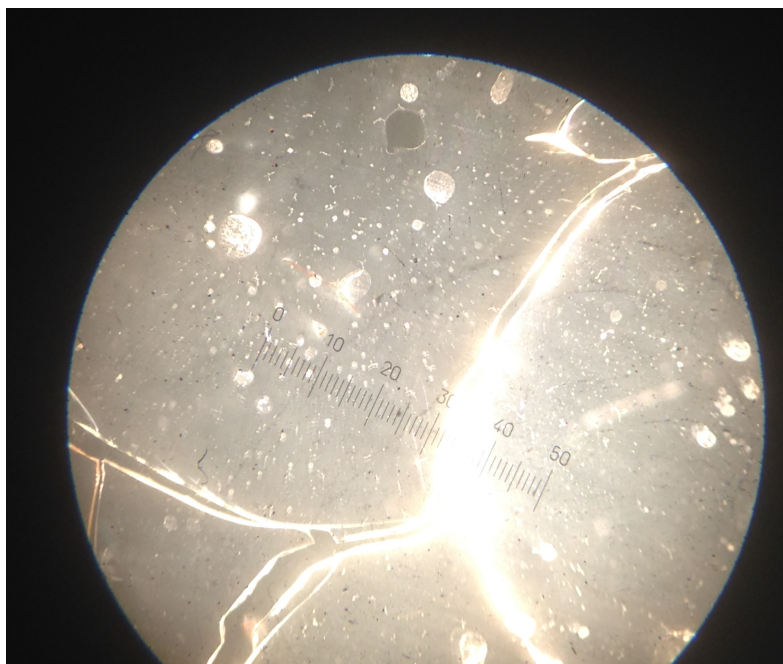


Figure 11: Optical Micrograph of 9.7 vol% Par-Gel (40x)

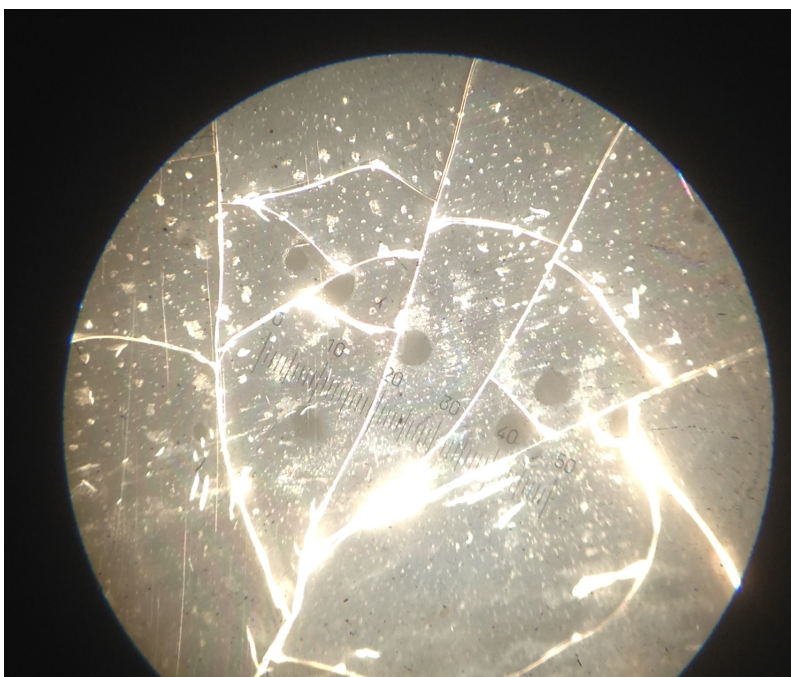


Figure 12: Optical Micrograph of 17.6 vol% Par-Gel (40x)

The apparent linear scratches in the profilometry samples are an artifact from the aluminum foil roughness and are not gel features. Regardless, it is quite clear that the paraffin wax microparticles are dispersed across a wide range of sizes ($\sim 1\text{-}100\text{ }\mu\text{m}$) and shapes. Furthermore, in **Figures 13-15 and Appendices 7-9**, similar wax microparticles are found in the Micro-gel micrographs; however, there also exists semi-continuous regions of wax that were not emulsified.



Figure 13: Optical Micrograph of 5.2 vol% Micro-Gel (40x)



Figure 14: Optical Micrograph of 9.7 vol% Micro-Gel (40x)

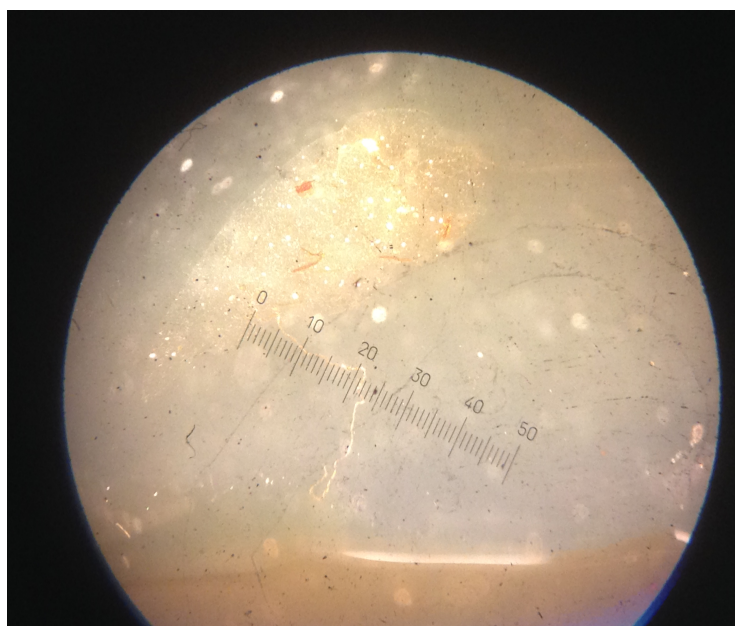


Figure 15: Optical Micrographs of 17.6 vol% Micro-Gel (40x)

Additionally, in **Figure 15**, macro-sized pools of wax appear in the 17.6 vol% Micro-gels and the population of microparticles becomes exceedingly low compared to the other wax-gel compositions.

4.2.2 THERMALLY DEGRADED SAMPLES

To qualitatively observe the effect of thermal degradation on these wax-gels, a separate set of glass slide samples were subjected to extended periods of time at elevated temperatures. For example, in **Figure 16**, 5.2 vol% Par-gel and Micro-gel samples were exposed to $\sim 200^{\circ}\text{C}$ for 4 days.

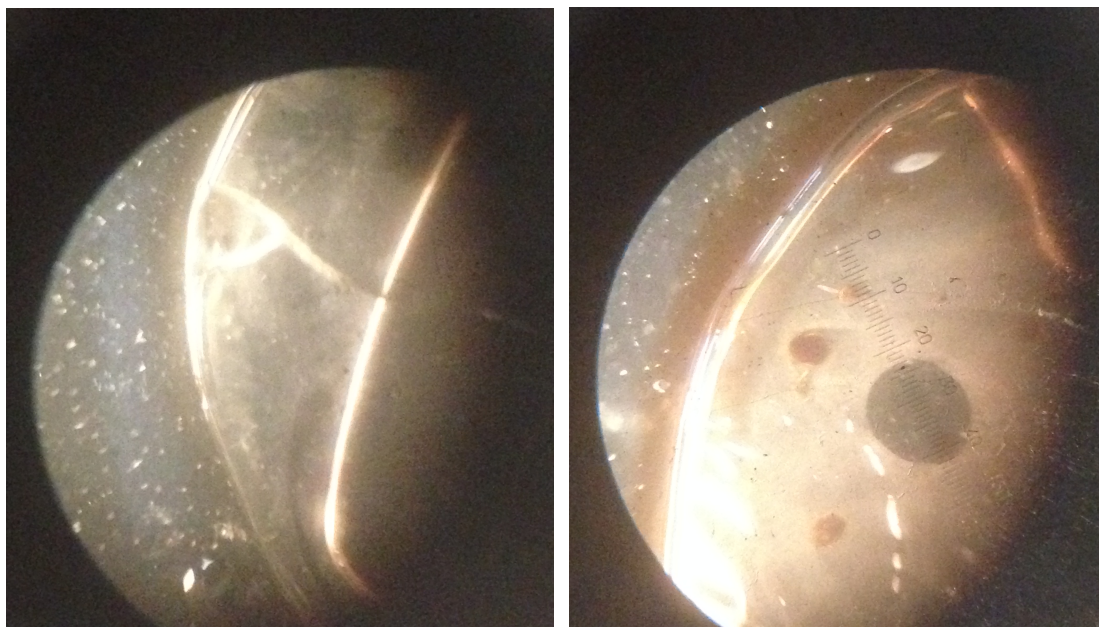


Figure 16: 40x Micrographs of 5.2% Par-gel (left)/Micro-gel (right) after 4 days at 200°C

These microscopic differences in thermal degradation are representative of the rest of the wax-gel compositions. However, there exists macroscopic heterogeneities in thick, wax-gel monoliths. For instance, in **Figure 17**, a 17.6% Par-gel was heated for 7 days at $\sim 180^{\circ}\text{C}$ and showed macroscopic gradients in thermal stability ranging over several centimeters.

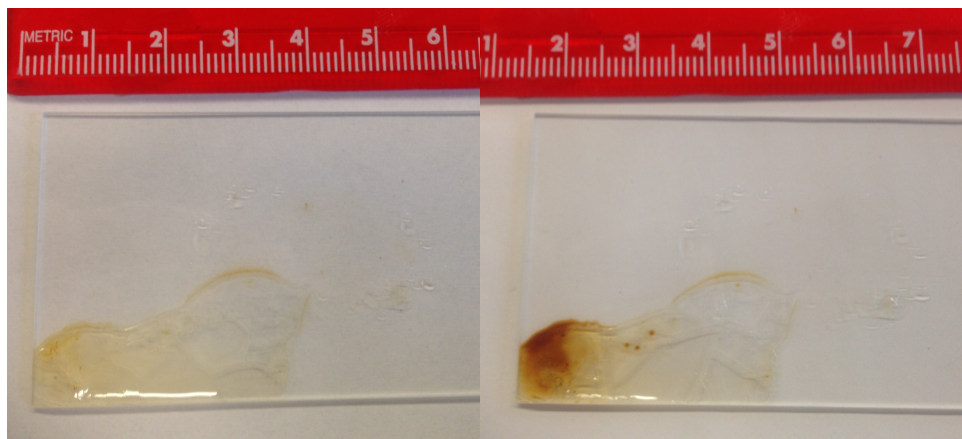


Figure 17: 17.6% Par-gel before (left) and after (right) 7 days at 180°C

The particle density and compositional gradient in this thermally degraded sample is accentuated by the UV lamp illumination ($\sim 300\text{ nm}$) in **Figure 18**.

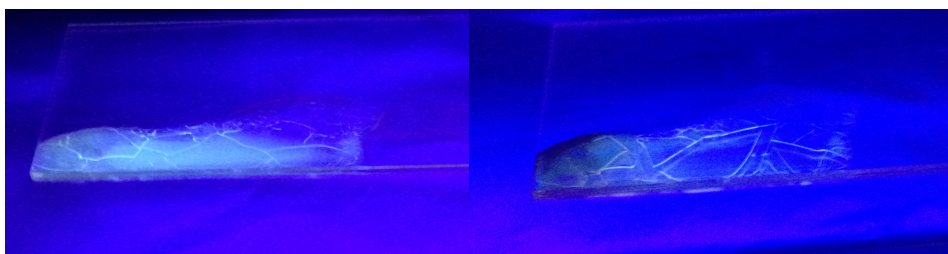


Figure 18: UV illumination of 17.6% Par-gel before (left) and after (right) 7 days at 180°C

This same, post-degraded sample was probed under the microscope across macroscopic gradient in **Figure 19**.

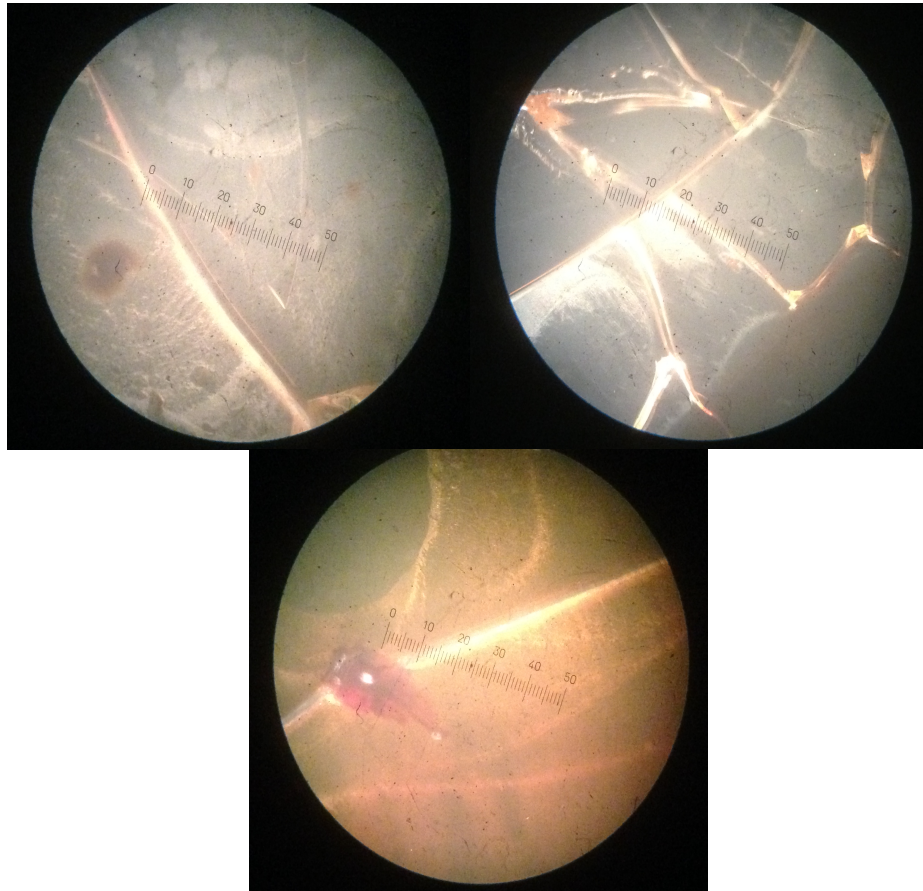


Figure 19: 100x micrographs of post-degraded 17.6% Par-gel across gradient

4.2.3 PARTICLE SIZE ANALYSIS

Combining the 40x and 100x optical micrographs, effective spherical particle sizes were plotted in the form of empirical distribution functions (EDFs). These are nonparametric, cumulative distribution functions (CDFs) that directly show the nature of

the raw data. For example, all of the observed wax-gel particle sizes were pooled together as an EDF in **Figure 20**. In **Figure 21**, this EDF was decomposed into its constituent data sets for each wax-type.

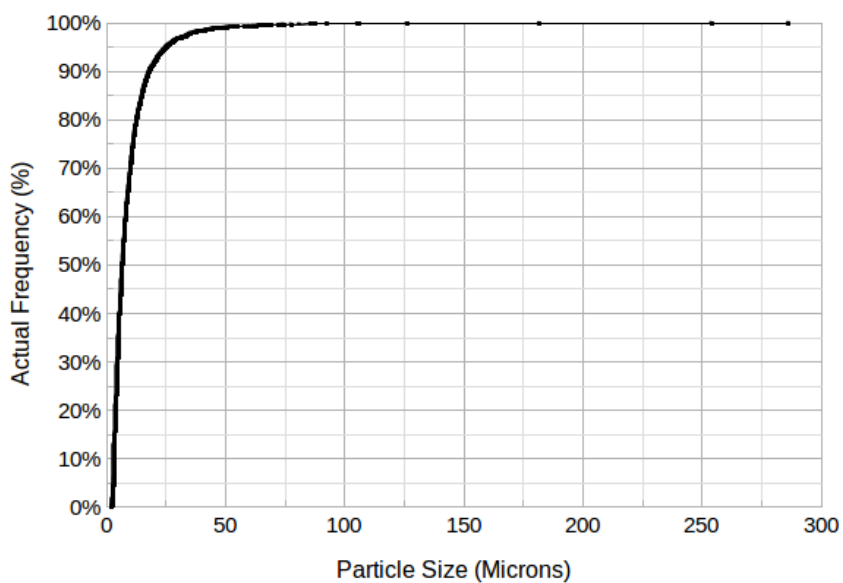


Figure 20: EDF of all Wax-gel optical particle sizes ($n = 3564$)

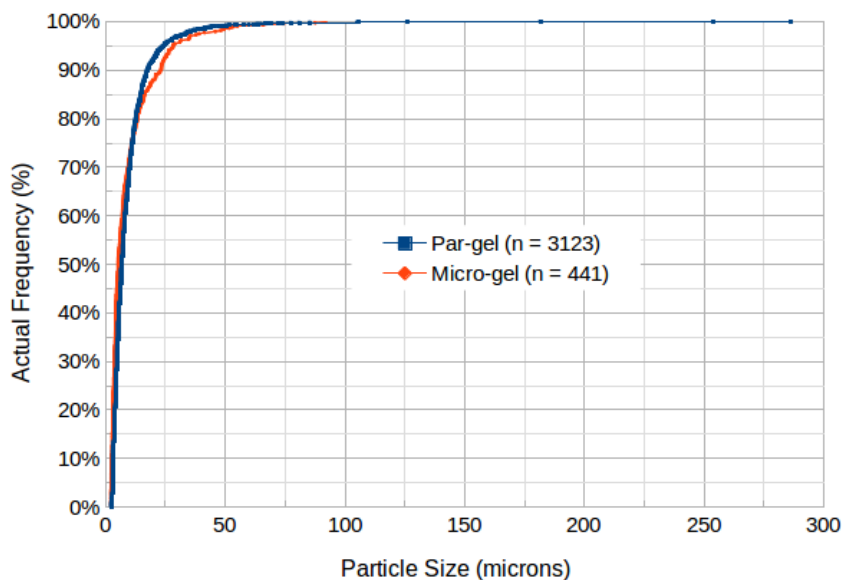


Figure 21: EDFs of Par-gel and Micro-gel optical particle sizes

Within each wax type, these EDFs were further decomposed by wax content in **Figures 22-23**.

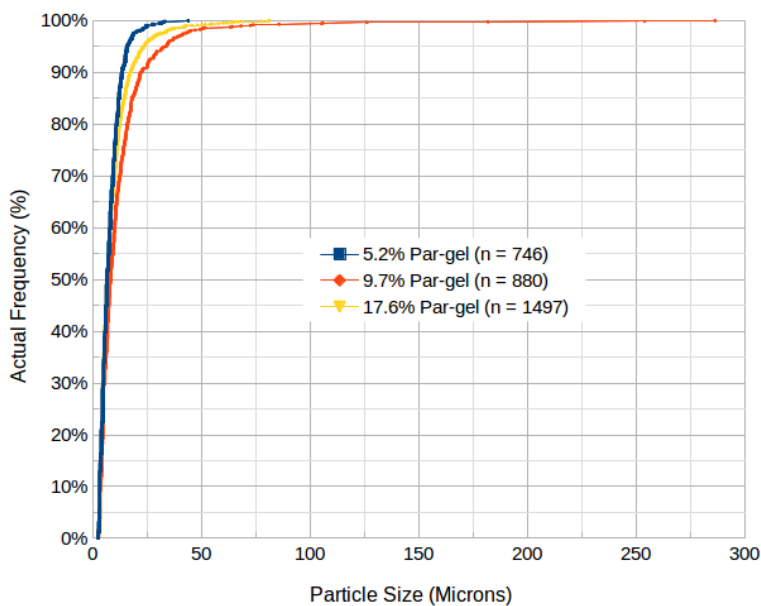


Figure 22: EDFs of Par-gel optical particle sizes across various wax contents

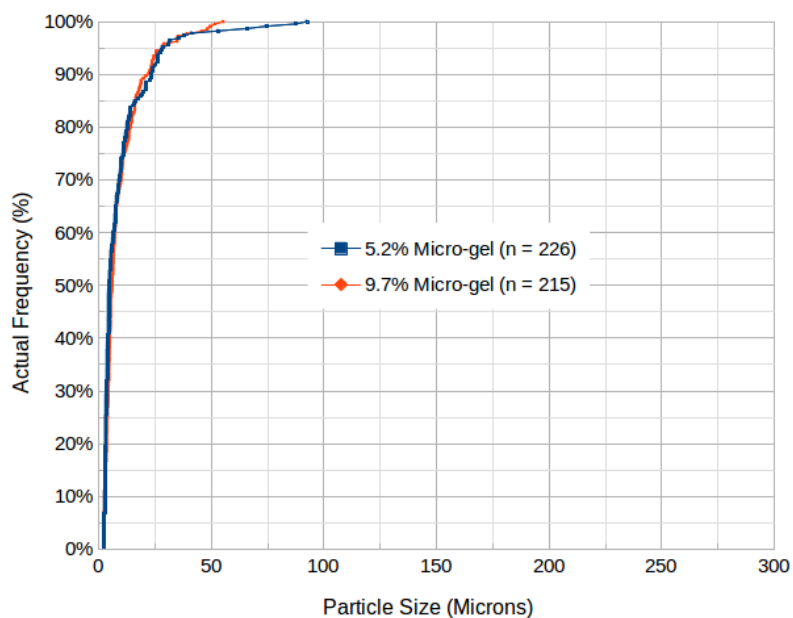


Figure 23: EDFs of Micro-gel optical particle sizes across various wax contents

In **Figure 23**, the 17.6% Micro-gel was dominated by segregated wax pools and did not provide any significant number measurable particles.

To quantitatively discern whether these EDFs were statistically distinguishable between each other, two sample Kolmogorov–Smirnov tests were conducted. The results of these tests are summarized below in **Table 5**.

Wax-Gel Combo	n	m	$D_{n,m}$	p-value
Par-Micro	3123	441	0.17696	$4.5205 \cdot 10^{-11}$
5.2%-9.7% Par	746	880	0.17213	$6.0330 \cdot 10^{-11}$
9.7%-17.6% Par	880	1497	0.13241	$5.9180 \cdot 10^{-9}$
5.2%-17.6% Par	746	1497	0.11599	$2.6127 \cdot 10^{-6}$
5.2%-9.7% Micro	226	215	0.16602	$3.9553 \cdot 10^{-3}$

Table 5: Two sample Kolmogorov–Smirnov tests of Wax-gel optical particle sizes

Due to the steepness of these EDFs, the corresponding histograms they produce are extremely heavy tailed and difficult to compare between each other. Likewise, the choice of bin size directly changes the perceived nature of the data. A representative example is shown below in **Figure 24**, where all observed particle sizes were pooled together.

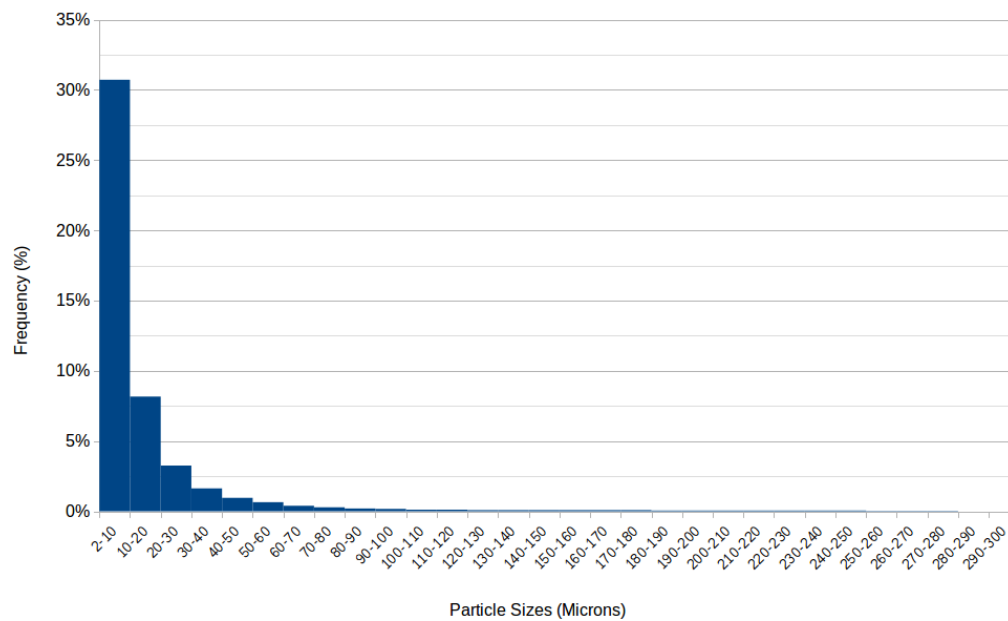


Figure 24: Histogram of All Pooled Wax-gel Optical Particle Sizes

Given the complexity of this analysis, it is unrealistic based off these sample sizes to derive an accurate model for predicting the particle size distribution of any wax-gel directly as a function of wax type and volume fraction. Instead, it is more prudent to model the general shapes of these distributions and quantify the range in which the underlying parameters vary. The logical approach to this was to use the pooled wax-gel EDF as the representative data for fitting the likeliest underlying CDF. Otherwise, using the noisier, lower sample size data sets would lead to an infeasible range of possible distributions to narrow down. Using these possible distributions, appropriate fits to the constituent EDFs could be made by minimizing the Kolmogorov–Smirnov statistic and other measures of fit. Consequently, a range of modeling parameters were estimated to bound the behavior of these wax-gels.

Nonetheless, a significant drawback to using image analysis for particle size determination is highlighted below in **Figure 25**.

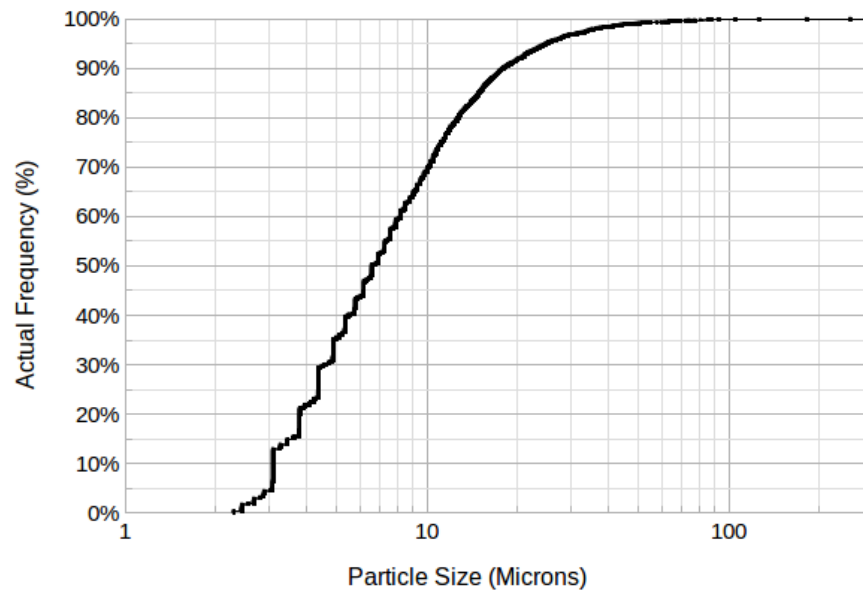


Figure 25: Semi-log EDF plot of all Wax-gel optical particle sizes

As seen in **Figure 25**, the EDF approaches infinite steepness at low particle sizes, due to the presence of these unnatural, graded steps. This is because of the inherent nature of thresholding in image analysis; truncating creates less combinations of distinguishable pixel clusters near the resolution limit. As a result, seemingly identical particle sizes are grouped together in steep, discrete EDF steps. These steps are artifacts that do not accurately represent the true nature of underlying distribution.

Through trial and error, these wax-gel EDF distributions were best fit piecewise using two different CDFs to model the lower and upper bounds. Specifically, Weibull distributions were chosen out of convenience to effectively fit the steep lower bounds and Gamma distributions were found to most suitably fit the curvature of the upper bounds.

By combining the two parameters from each distribution, each EDF could be effectively modeled with a four parameter system. This piecewise distribution model is representative by the following equation:

$$P(x) = \begin{cases} \text{Gamma}(\alpha, \beta, x) = 1/\Gamma(\alpha) \cdot \gamma(\alpha, \beta x), & x > x^* \\ \text{Weibull}(k, \lambda, x) = (1 - \exp(-(x/\lambda)^k)), & x \leq x^* \end{cases}$$

where $P(x)$ is the cumulative probability, x is the random variable (particle size), α is the shape parameter of the Gamma distribution, β is the rate parameter of the Gamma distribution, Γ is the Gamma function, γ is the lower incomplete gamma function, λ is the scale parameter of the Weibull distribution, k is the shape parameter of the Weibull distribution, and x^* is the intersection of the Gamma and Weibull distributions.

To model the EDF lower and upper bounds effectively, a Monte Carlo approach was iteratively used to minimize best fit indicators. These best fit indicators included the Kolmogorov–Smirnov D-statistic, residual square sum, absolute residual sum, yule skewness coefficient, and median absolute deviation. With these five indicators, convergent solutions could be obtained without significant bias from extreme values. Due to the piecewise nature of these distributions, the critical transition point between models was artificially determined by cumulatively recalculating the D-statistic with incremental subsets of the EDF data until it was above an appropriate multiple of the running average D-statistic. This step size increment and running average multiple were carefully tuned to achieve the unique sensitivity of each EDF. This was repeated until convergent

solutions were obtained and visually confirmed as best fits. These CDF best fits are plotted with there respective EDFs below in **Figures 26-27 and Appendix 10**.

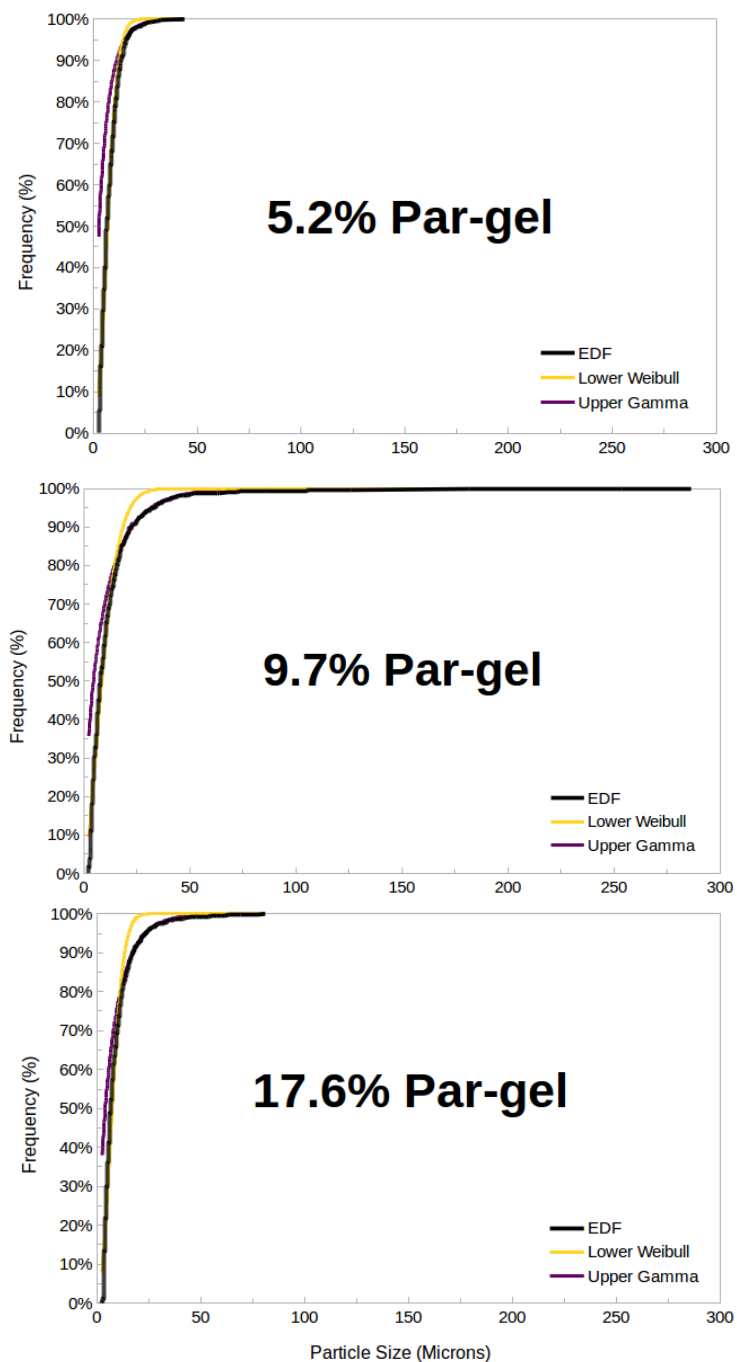


Figure 26: Par-gel Optical Particle Size Best Fits

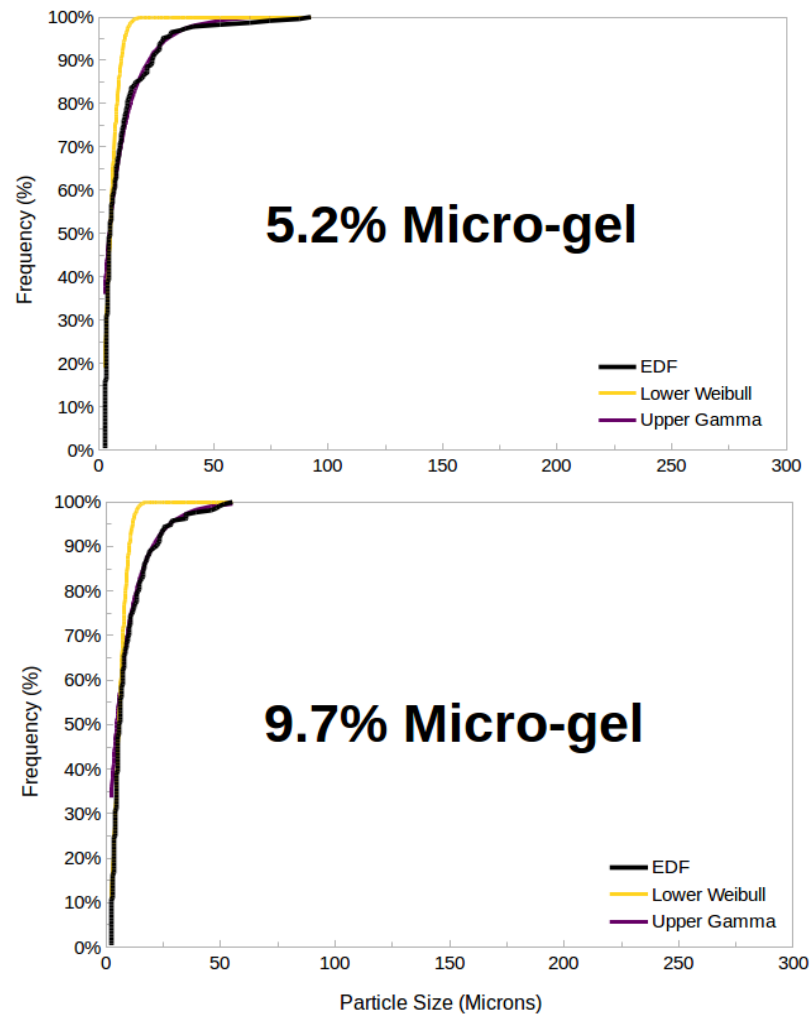


Figure 27: Micro-gel Optical Particle Size Best Fits

For each wax-gel CDF, tabulated best fit parameters are presented below in **Table 6**.

	Sample Size	Best Model Fit Parameters				
EDFs	n	x^*	α	β	k	λ
Wax-gels	3564	15	0.223487	21.005246	1.595975	0.103909

Par-gels	3123	13	0.268931	18.306503	1.596116	0.107295
Micro-gels	441	6	0.659572	12.956003	1.776615	0.150147
5.2% Par	746	13	0.732332	6.119340	1.970132	0.122594
9.7% Par	880	15	0.602737	14.642449	1.545710	0.092464
17.6% Par	1497	12	0.692506	9.873869	1.965556	0.114523
5.2% Micro	226	5	0.618732	13.589893	1.730226	0.167151
9.7% Micro	215	7	0.679338	11.827433	2.019827	0.148722
17.6% Micro	0	-	-	-	-	-

Table 6: Parameters of CDF Best Fits for Wax-gel Optical Particle Size EDFs

Given that the lower Weibull fits represent the truncation errors of the image analysis, the upper-Gamma fits are the best estimates for the true underlying particle size distributions. The comparative medians and parameter ranges between the wax-gels is tabulated below in **Tables 7-9** and plotted in **Figures 28-29**.

Interval (5.2-17.6%)	α	β
Par-gels	0.667534 ± 0.064796	10.380895 ± 4.261554
Micro-gels	0.649035 ± 0.030303	12.708663 ± 0.881230

Table 7: Bounded Gamma Parameter Ranges for Par/Micro-gel Optical Particle Sizes

	EDF Median (microns)	Gamma Median (microns)
Wax-gels	6.57	0.64
Par-gels	6.90	0.99
Micro-gels	5.26	4.79
5.2% Par-gel	6.54	2.68
9.7% Par-gel	8.08	4.66
17.6% Par-gel	6.56	3.95
5.2% Micro-gel	4.74	4.52
9.7% Micro-gel	5.85	4.59

Table 8: Medians of Optical Particle Size Wax-gel CDFs and EDFs

Interval (5.2-17.6%)	EDF Median (microns)	Gamma Median (microns)
Par-gels	7.31 ± 0.77	3.67 ± 0.99
Micro-gels	5.30 ± 0.56	4.56 ± 0.04

Table 9: Bounded Median Ranges for Par/Micro-gel Optical Particle Sizes

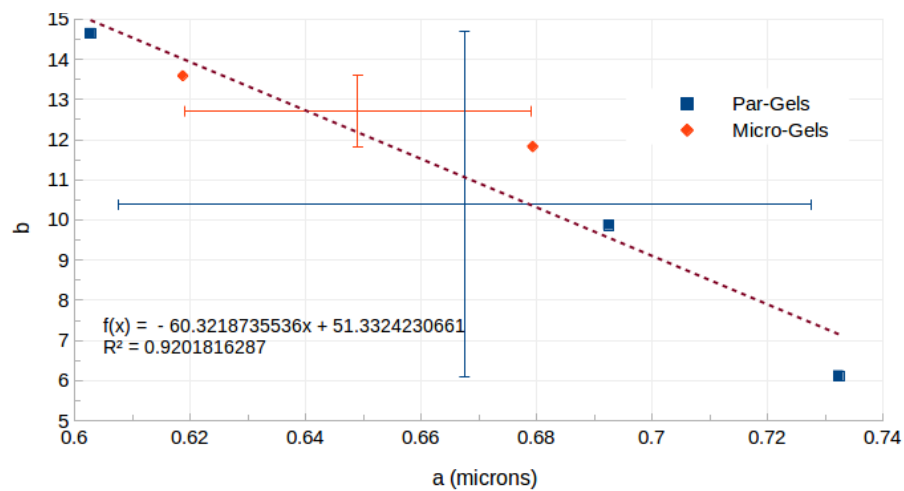


Figure 28: Gamma Parameters for Par-gel and Micro-gel Optical Particle Sizes

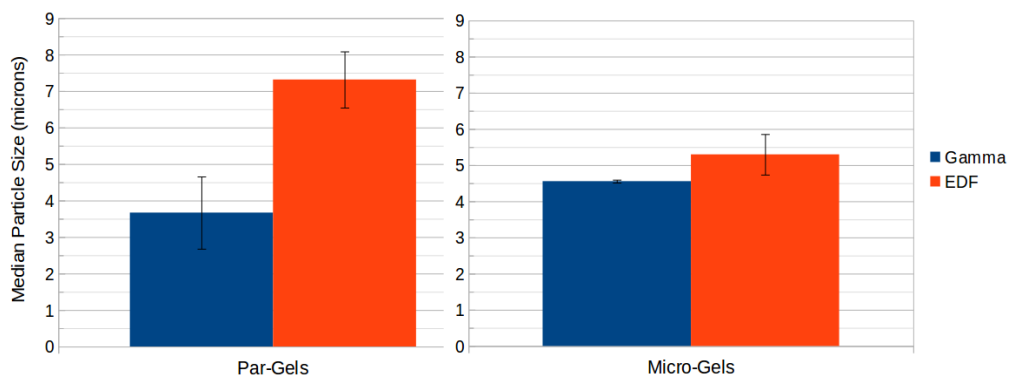


Figure 29: Median Ranges for Par-gel and Micro-gel Optical Particle Sizes

4.3 SEM ANALYSIS

4.3.1 REPRESENTATIVE MICROGRAPHS

Scanning electron microscopy (SEM) was employed to further characterize the microstructure of these wax-gels. Instead of probing through the optically transparent gel phase, the fracture surfaces of cleaved gel samples were imaged with the SEM to reveal bulk features hidden below the surface. In **Figure 30**, a representative SEM micrograph of a control gel was taken.

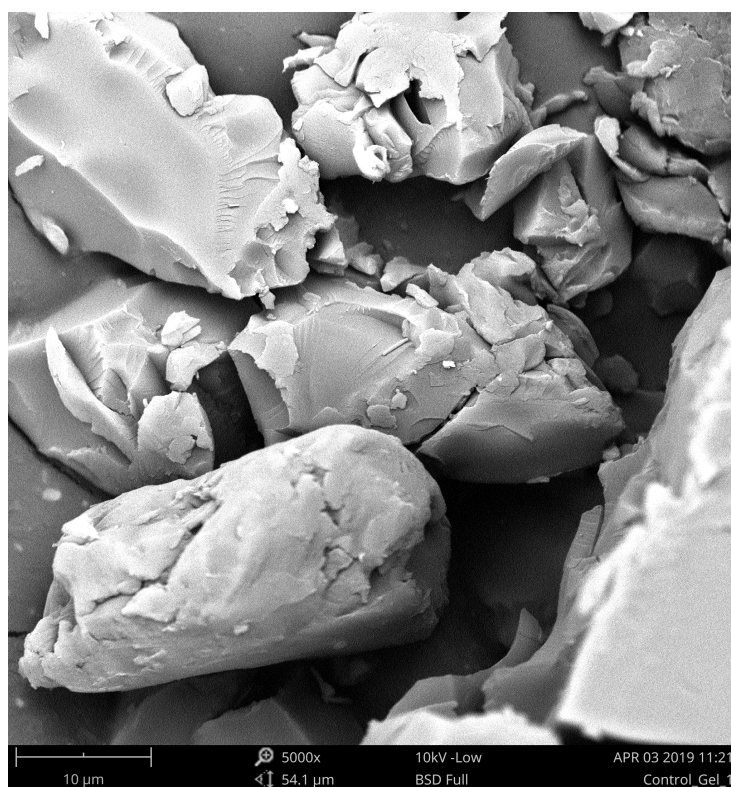


Figure 30: Representative Melting Gel SEM Micrograph

In **Figures 31-33**, representative SEM micrograph of Par-gels across various wax volume percents were taken.

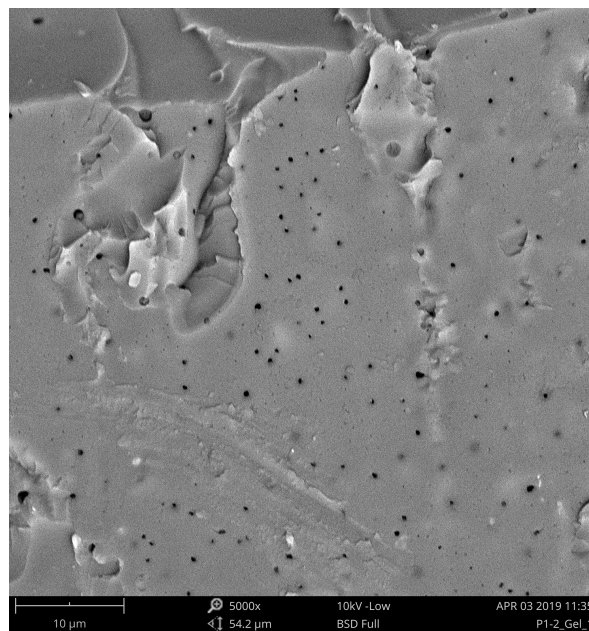


Figure 31: SEM Micrograph of 5.2 vol% Par-Gel

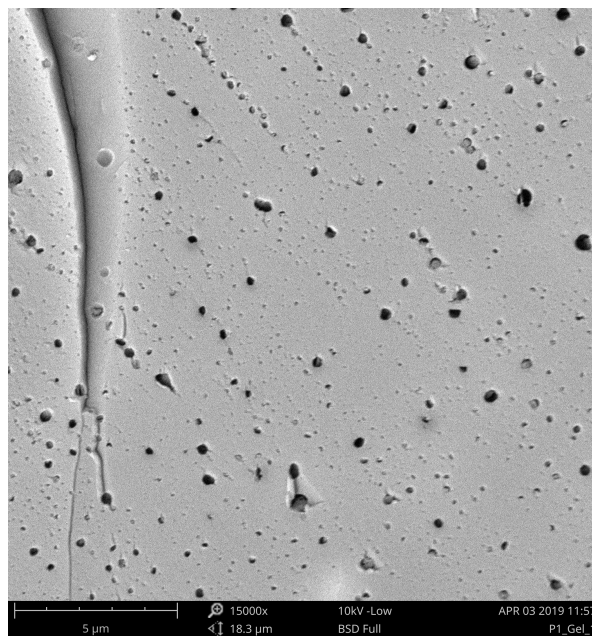


Figure 32: SEM Micrograph of 9.7 vol% Par-Gel

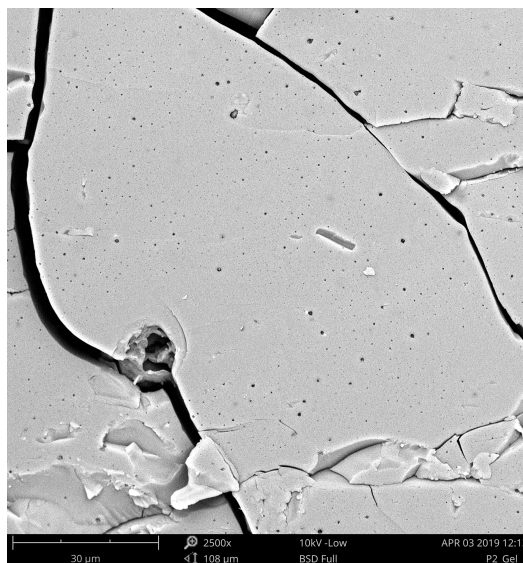


Figure 33: SEM Micrograph of 17.6 vol% Par-Gel

The apparent holes in the Par-Gel micrographs are where the wax microparticles resided before being ejected from processing. In **Figures 34-36**, representative Micro-gel micrographs with these same dispersed wax cavities were taken.

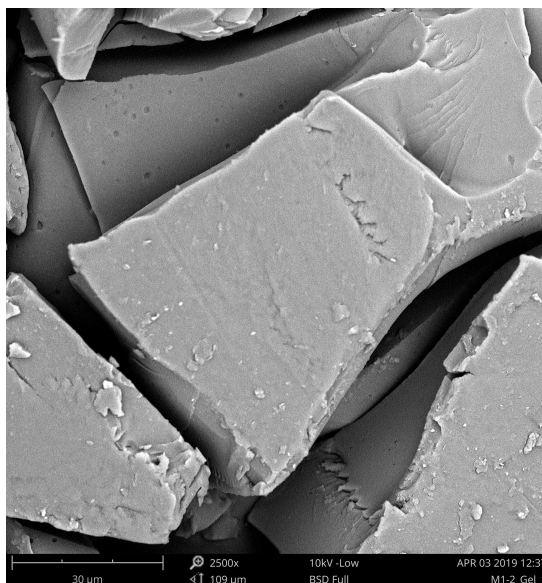


Figure 34: SEM Micrograph of 5.2 vol% Micro-Gel

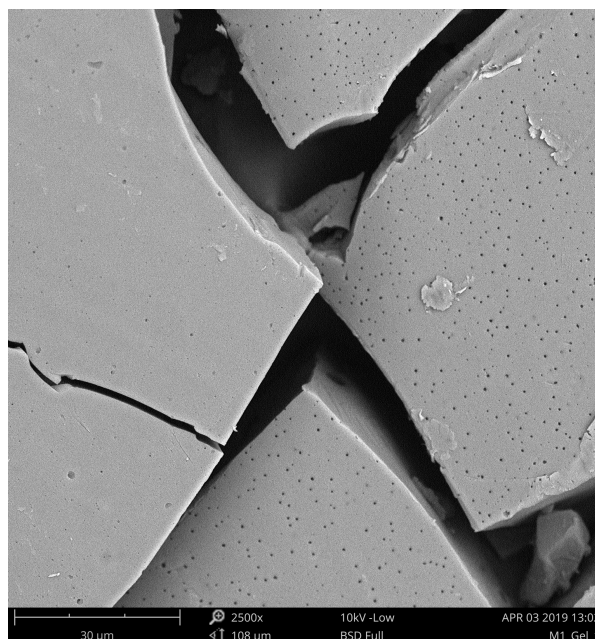


Figure 35: SEM Micrograph of 9.7 vol% Par-Gel

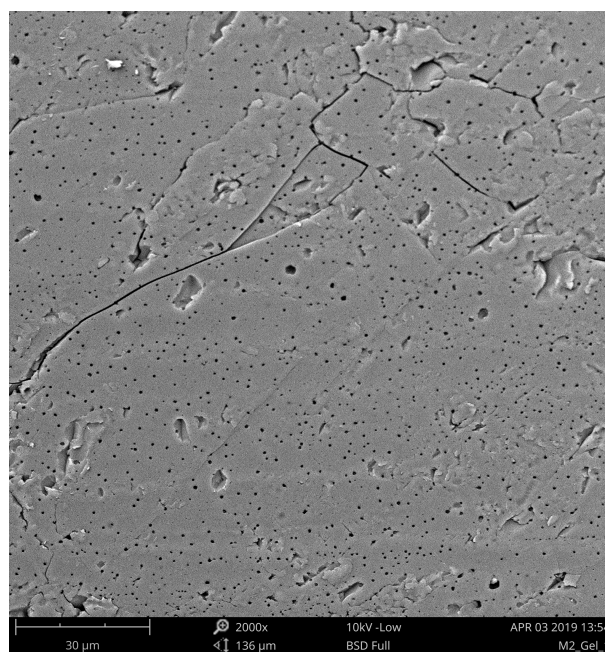


Figure 36: SEM Micrograph of 17.6 vol% Par-Gel

4.3.2 PROFILOMETRY SAMPLE

In **Figure 37-39**, a representative micro-gel profilometry sample was scanned with the SEM such that the top surface remained preserved and unfractured. Thus, instead of dispersed particles, this wax is surface segregated in form of islands.

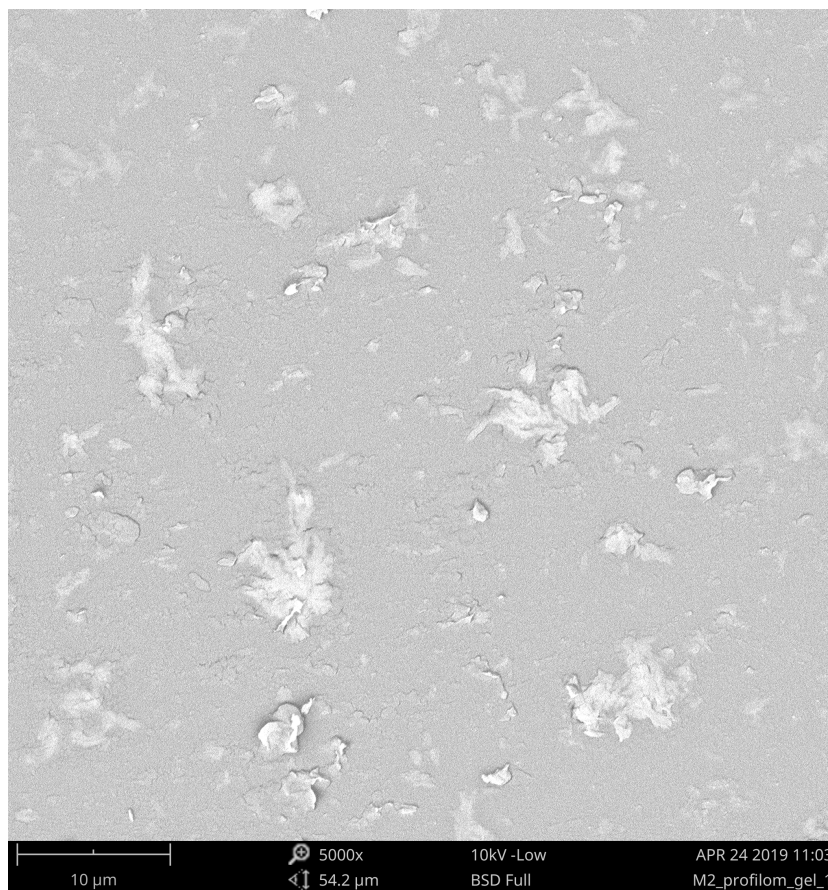


Figure 37: 5000x SEM Micrograph of 17.6 vol% Micro-Gel Profilometry Sample

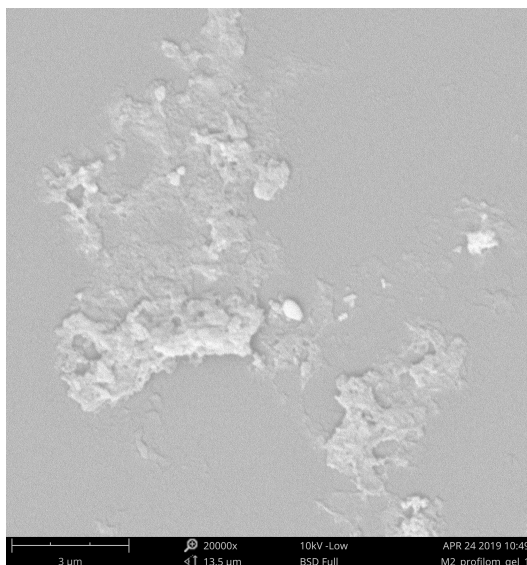


Figure 38: 20,000x SEM Micrograph of 17.6 vol% Micro-Gel Profilometry

Sample

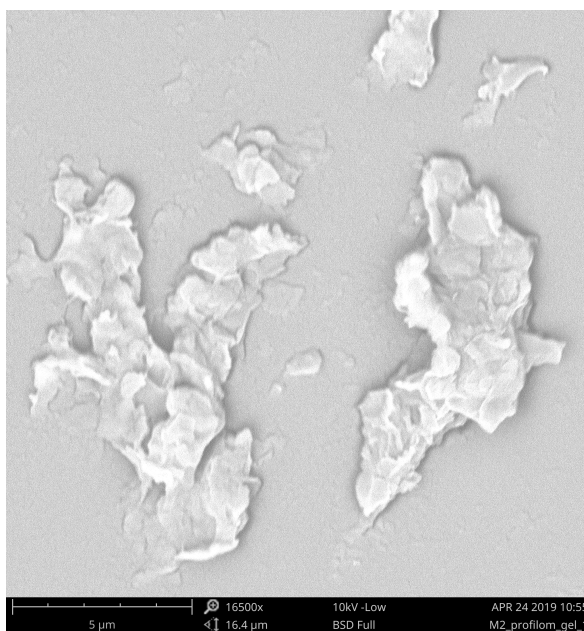


Figure 39: 16,500x SEM Micrograph of 17.6 vol% Micro-Gel Profilometry

Sample

In **Figures 37-39**, the wax islands are only specific to the Micro-gels, since Par-gels did not exhibit these features.

4.3.3 PARTICLE SIZE ANALYSIS

Following the same approach as the optical microscopy analysis, wax-gel EDFs were modeled with respect piecewise Gamma-Weibull distributions respectively. In **Figures 40-43**, these wax-gel EDFs are plotted respectively.

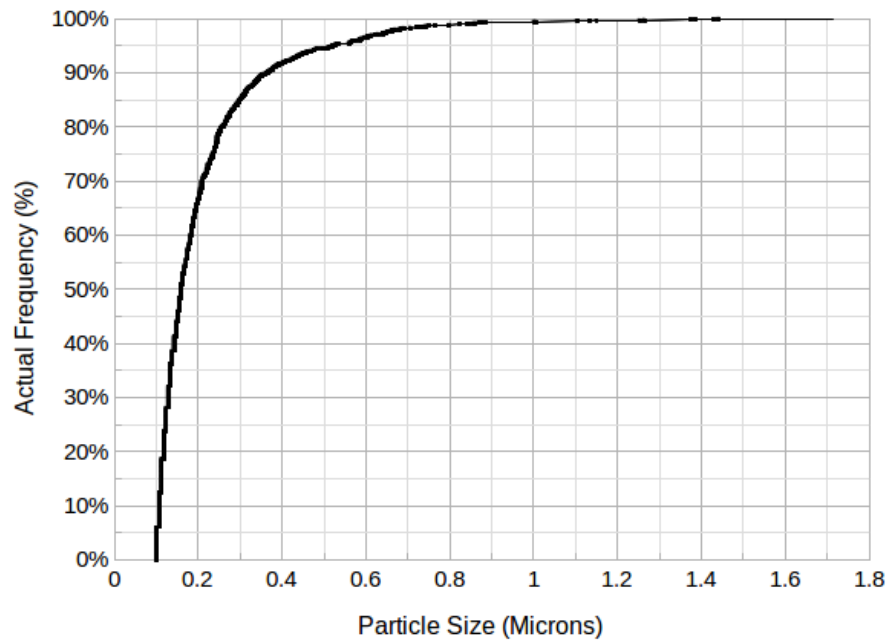


Figure 40: EDF of all SEM Wax-gel particle sizes ($n = 1774$)

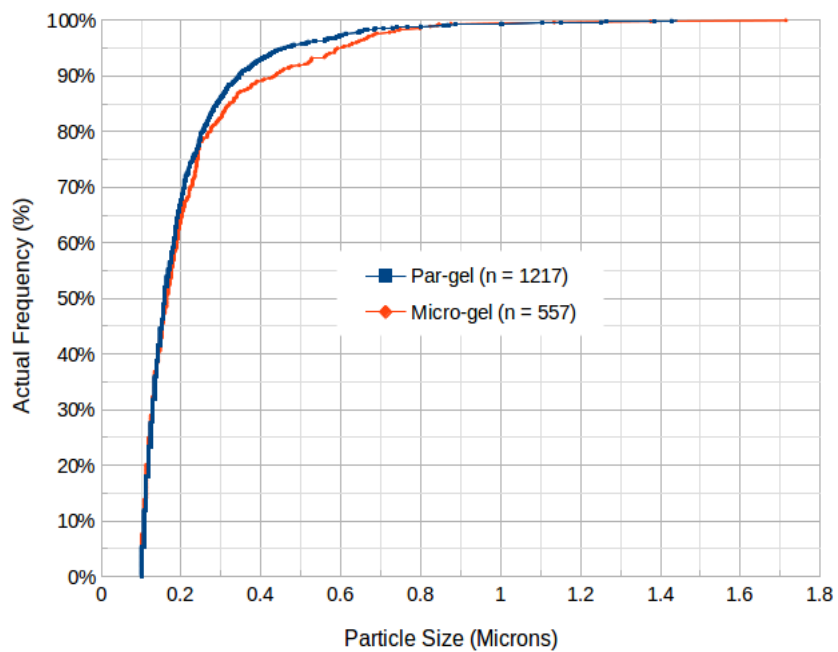


Figure 41: EDF of SEM Par/Micro-gel particle sizes

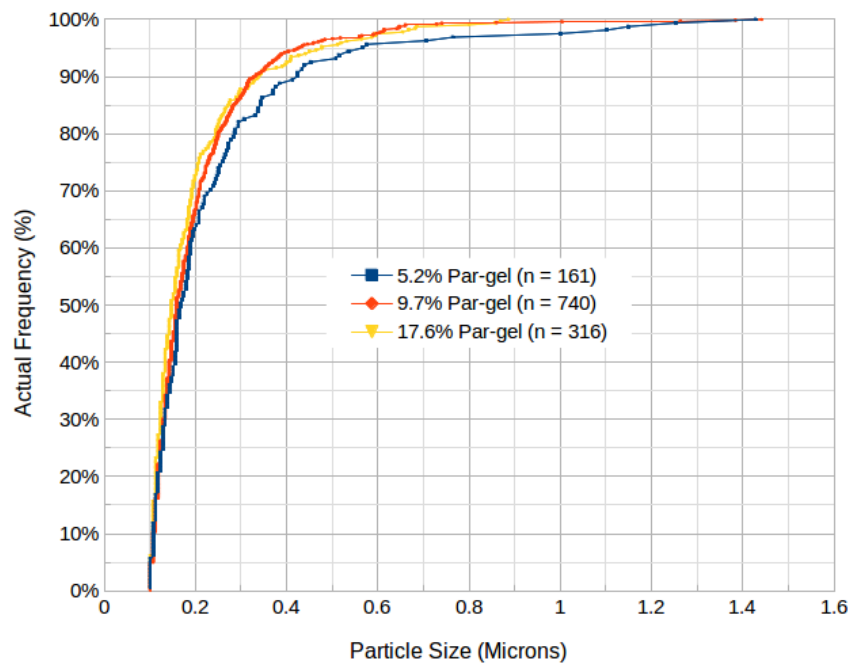


Figure 42: EDF of SEM Par-gel particle sizes across various volume percents

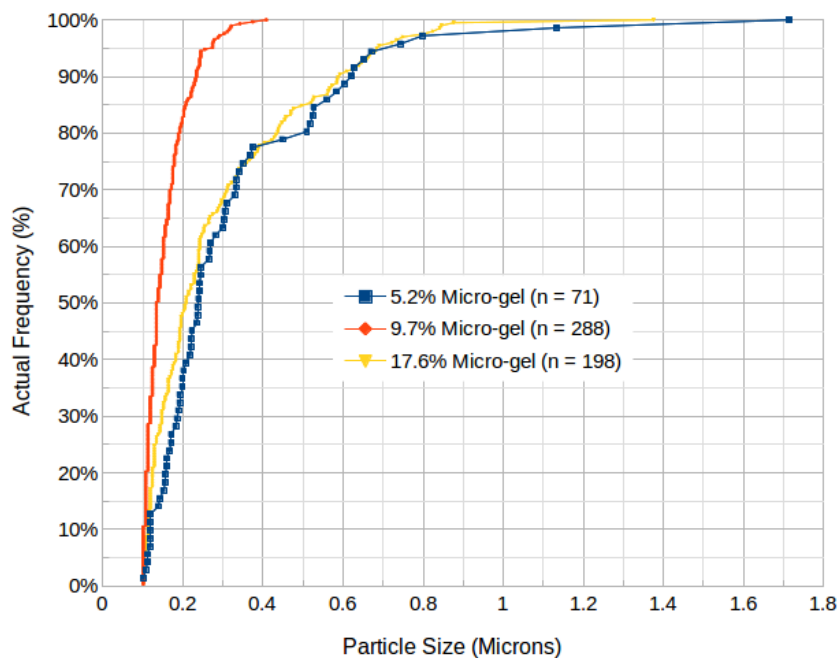


Figure 43: EDF of SEM Micro-gel particle sizes across various volume percents

In **Figure 44**, a histogram of the pooled SEM wax-gel was constructed below.

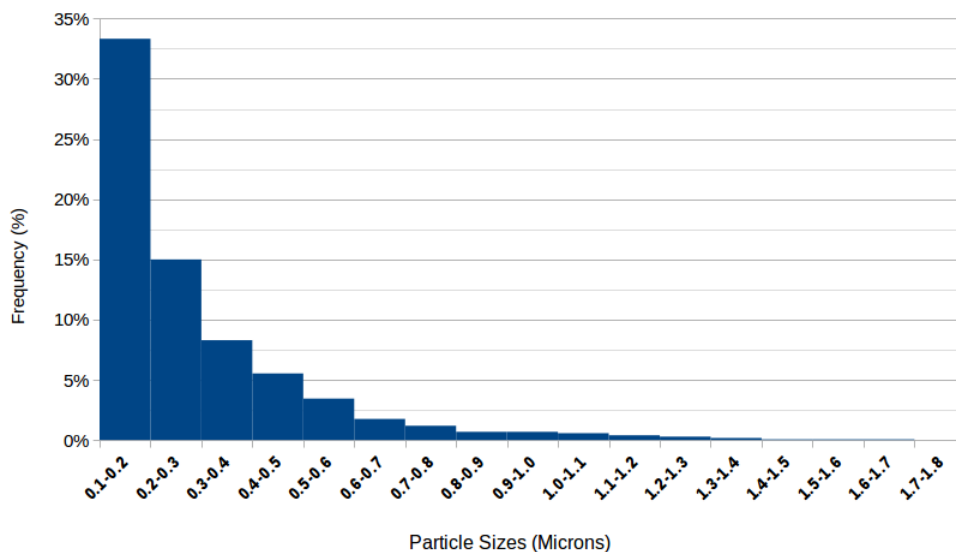


Figure 44: Histogram of all pooled SEM wax-gel particle sizes

In **Figures 45-46 and Appendix 11**, these wax-gel CDF best fits are plotted respectively with their corresponding EDFs.

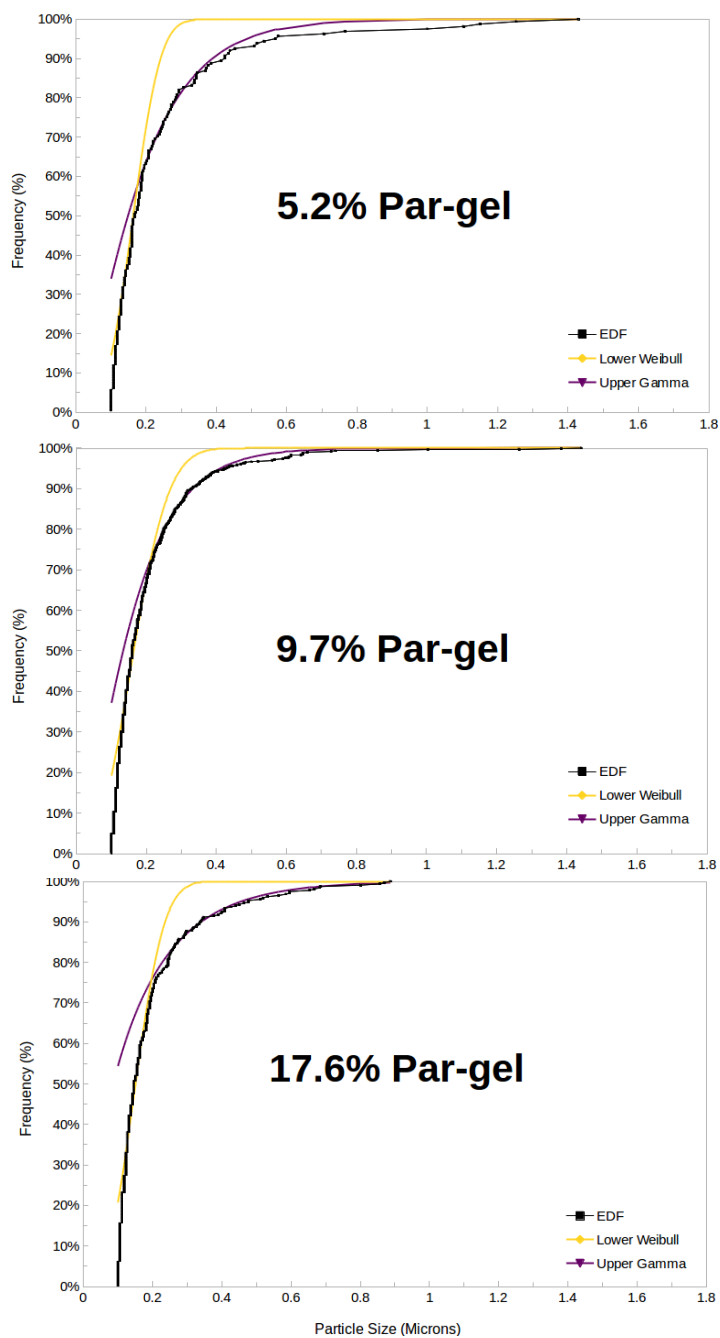


Figure 45: Par-gel SEM Particle Size Best Fits

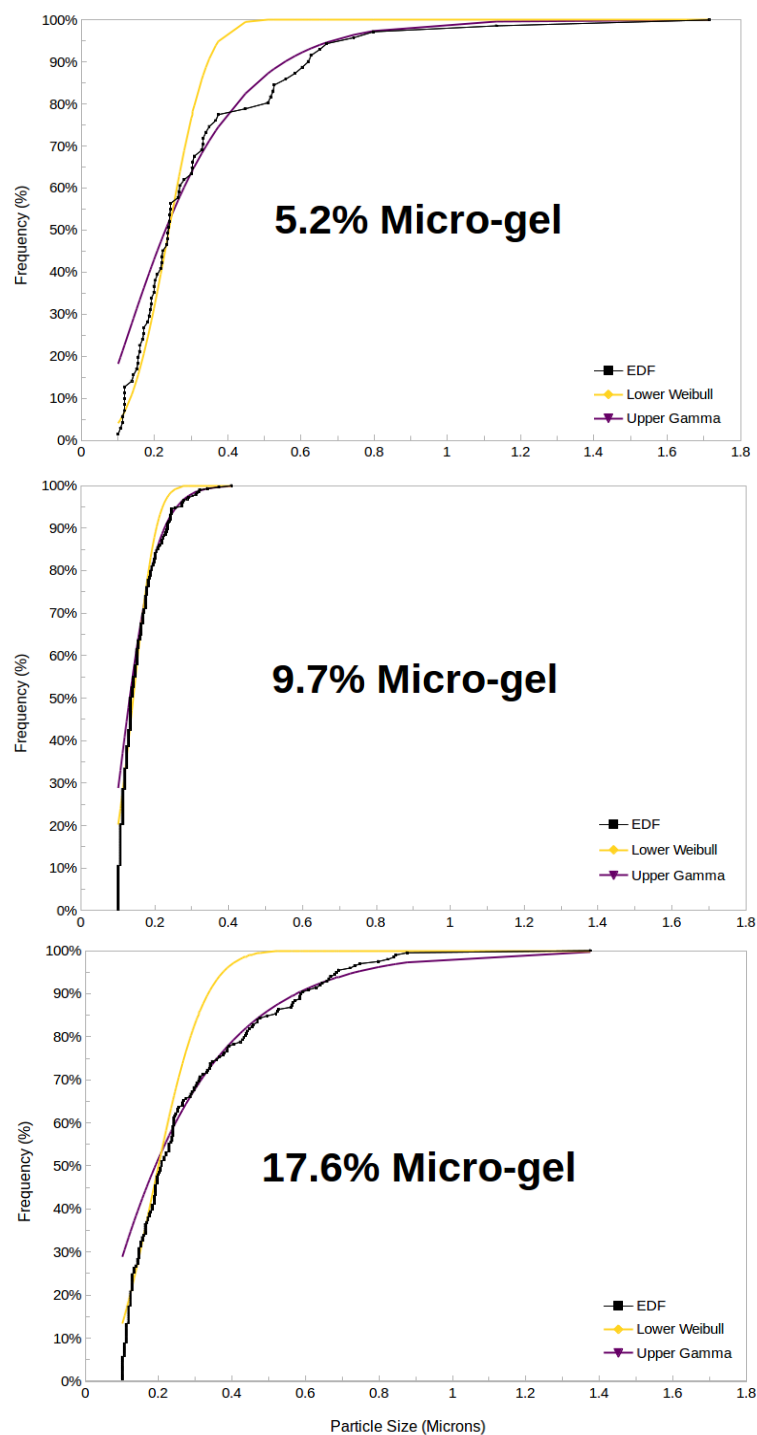


Figure 46: Micro-gel SEM Particle Size Best Fits

For each SEM wax-gel CDF in **Figures 45-46 and Appendix 11**, tabulated best fit parameters are presented below in **Table 8**.

	Sample Size	Best Model Fit Parameters				
EDFs	n	x*	α	β	k	λ
Wax-gels	1774	0.25	0.663858	0.215778	2.324675	0.196534
Par-gels	1217	0.23	0.757882	0.183886	2.480874	0.186070
Micro-gels	557	0.18	0.640815	0.252295	2.128706	0.197070
5.2% Par	161	0.15	1.534649	0.122215	3.084509	0.184268
9.7% Par	740	0.16	1.710918	0.096318	2.422265	0.190897
17.6% Par	316	0.20	0.794527	0.175996	2.687951	0.173741
5.2% Micro	71	0.17	1.818679	0.153428	3.264064	0.267998
9.7% Micro	288	0.14	4.552268	0.030689	3.292328	0.158524
17.6% Micro	198	0.16	1.171621	0.221754	2.313574	0.233365

Table 10: Parameters of CDF Best Fits for SEM Wax-gel Particle Size EDFs

The comparative medians and parameter ranges between the SEM wax-gels is tabulated below in **Tables 11-13** and plotted in **Figures 47-48**.

Interval (5.2-17.6%)	α	β
Par-gels	1.252722 \pm 0.458196	0.136157 \pm 0.039839
Micro-gels	2.861945 \pm 1.690324	0.126222 \pm 0.095532

Table 11: Bounded Gamma Parameter Ranges for Par/Micro-gel SEM Particle Sizes

	EDF Median (microns)	Gamma Median (microns)
Wax-gels	0.160	0.081
Par-gels	0.150	0.085
Micro-gels	0.164	0.089
5.2% Par-gel	0.167	0.149
9.7% Par-gel	0.160	0.134
17.6% Par-gel	0.147	0.087
5.2% Micro-gel	0.239	0.230
9.7% Micro-gel	0.136	0.130
17.6% Micro-gel	0.208	0.191

Table 12: Medians of Optical Particle Size Wax-gel CDFs and EDFs

Interval (5.2-17.6%)	EDF Median (microns)	Gamma Median (microns)
Par-gels	0.157 \pm 0.010	0.118 \pm 0.031
Micro-gels	0.188 \pm 0.052	0.180 \pm 0.050

Table 13: Bounded Median Ranges for Par/Micro-gel SEM Particle Sizes

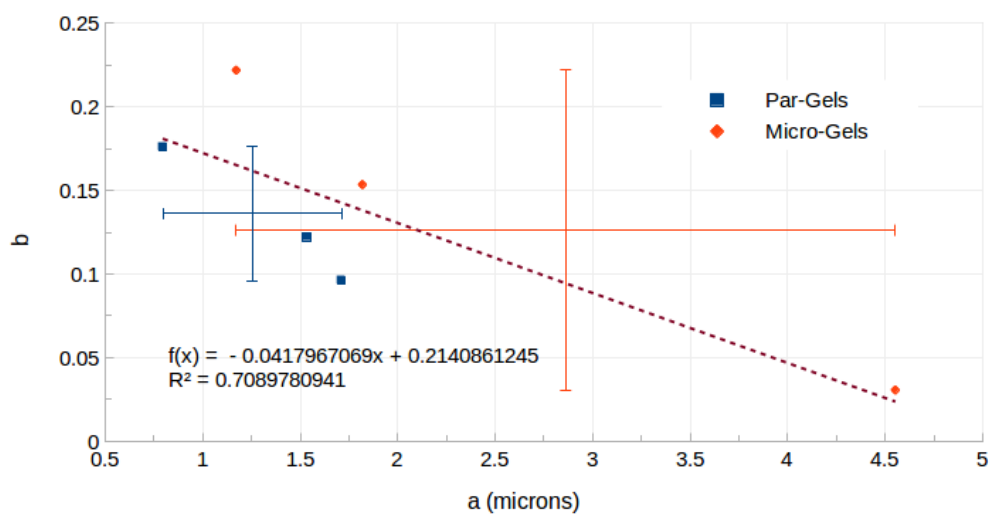


Figure 47: Gamma Parameters for Par-gel and Micro-gel SEM Particle Sizes

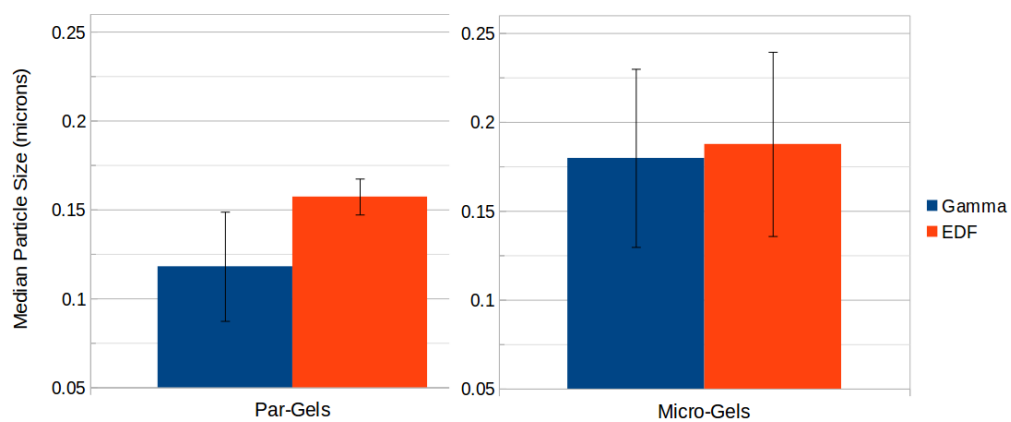


Figure 48: Median Ranges for Par-gel and Micro-gel SEM Particle Sizes

4.3.4 COMPARISON WITH OPTICAL PARTICLE SIZE DISTRIBUTIONS

By employing both SEM and optical microscopy, a wide range of particle sizes were cataloged. However, each technique is limited to their imaging resolution and maximum field of view. For example, optical microscopy could only identify particles between ~2-300 microns, while the SEM could only measure particles between ~0.1-2 microns. Since these measurable ranges practically overlap, it is reasonable to extrapolate the optical particle size model into the domain of the SEM particle sizes and only sample values constrained within this range. That way, the optical and SEM particle size distributions can be objectively compared to determine if each region shows distinctive underlying processes or can be unified in a single characteristic model. Using the best fit gamma parameters, generalized Par-gel and Micro-gel models were compared in **Figures 49-50 and Appendix 12**.

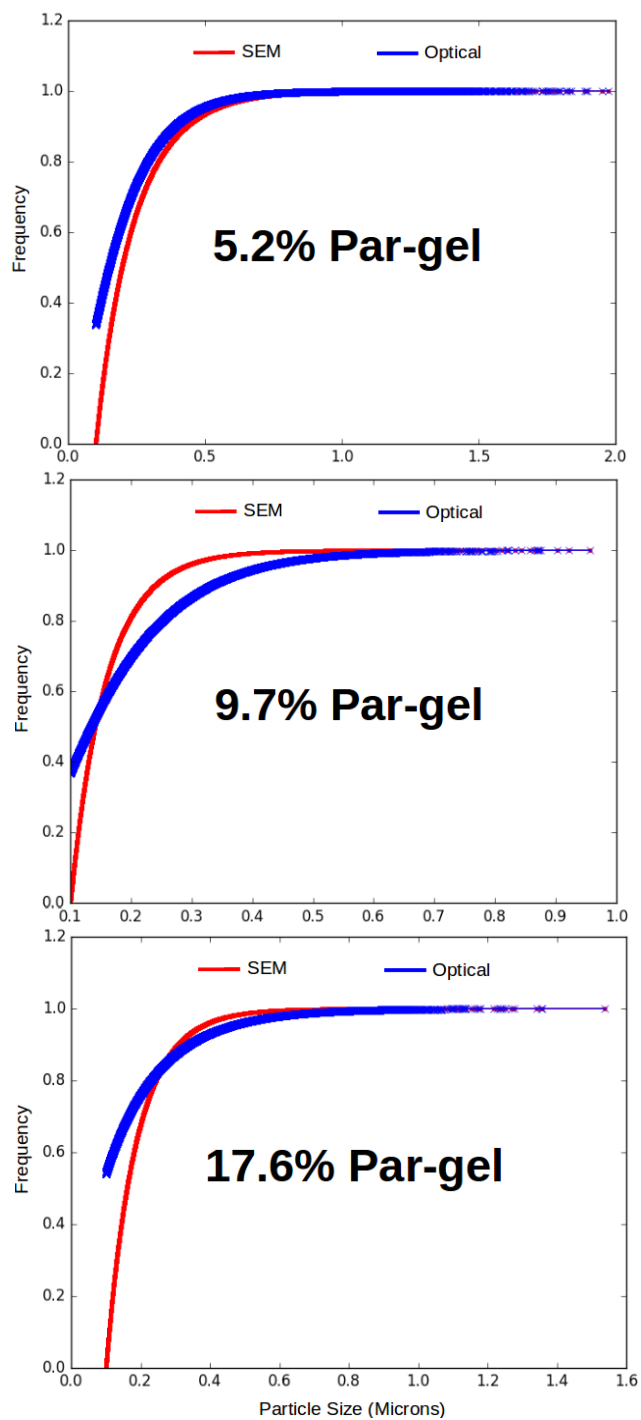


Figure 49: Par-Gel Optical-SEM Model Comparison

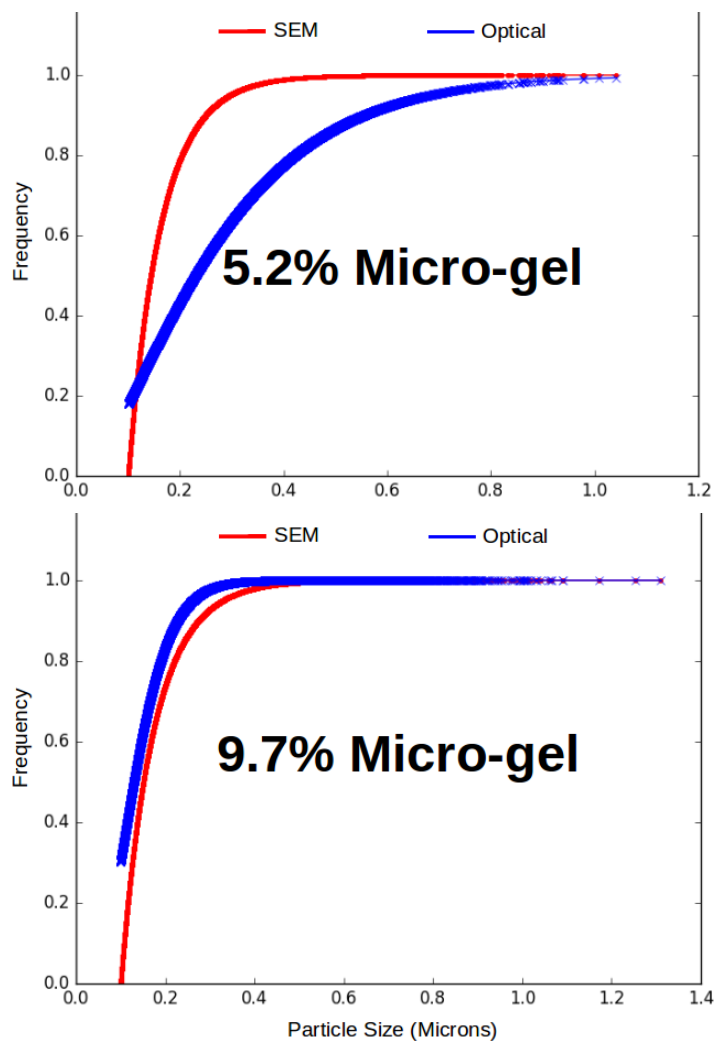


Figure 50: Micro-Gel Optical-SEM Model Comparison

Using the best matching optical model extrapolations, representative CDF/PDFs were constructed in **Figures 51-52** to illustrate the overall particle size distribution for the entire measurable range (~ 0.1 -300 microns) .

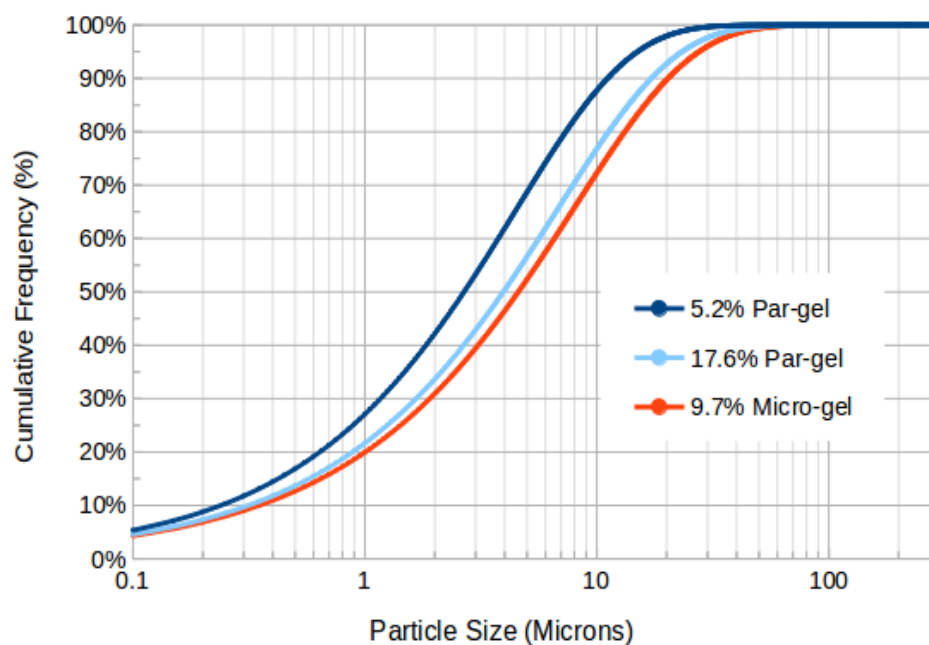


Figure 51: Representative Wax-gel Gamma CDF Fits Over Unified Optical-SEM Range

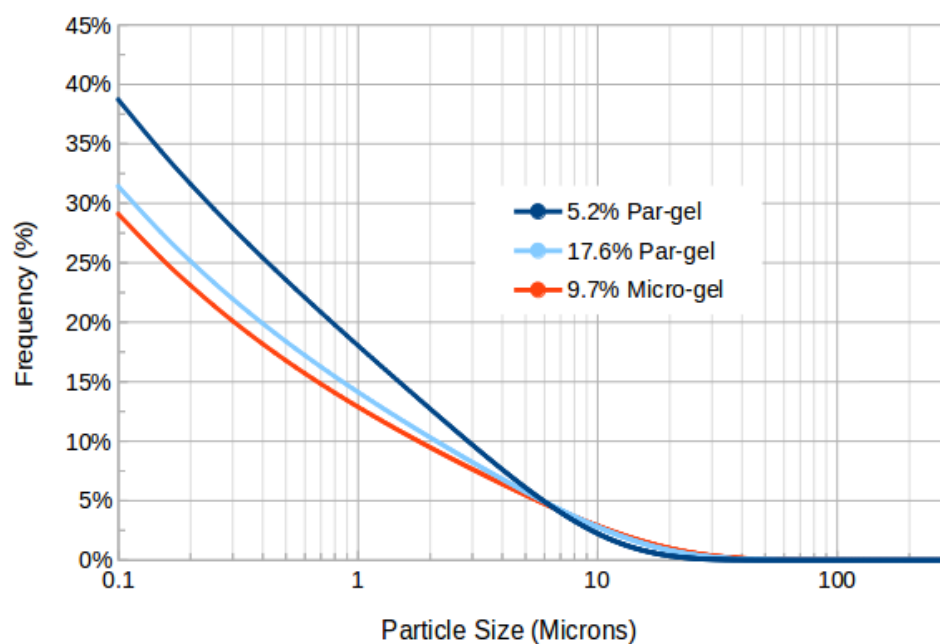


Figure 52: Representative Wax-gel Gamma PDF Fits Over Unified Optical-SEM Range

Using these generalized models, the relative wax volume percent each particle size contributes to the total wax content can be estimated using a spherical volume approximation and normalization from ~0.1-300 microns. This normalization uses the assumption that the ~5% of particles below 0.1 microns contribute negligible volume.

The corresponding volume PDF is plotted below in **Figure 53**.

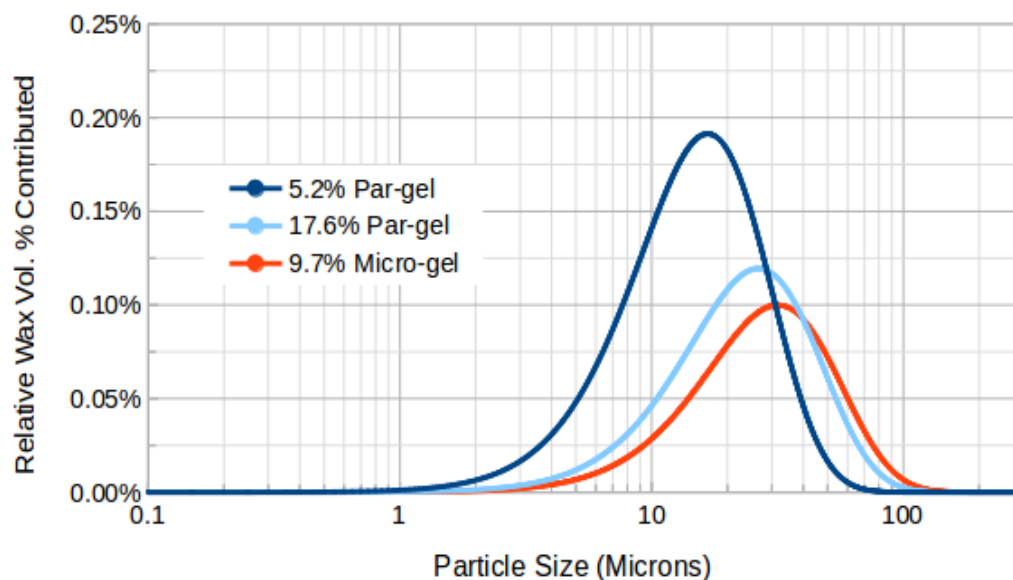


Figure 53: Best Wax-gel Gamma Volume PDF Fits Over Unified Optical-SEM Range

4.4 DIELECTRIC CHARACTERIZATION

4.4.1 DIELECTRIC BEHAVIOR OF WAX-GELS

Dielectric characterization of these wax-gels was performed in the RF spectral range (~1-1000 kHz) to study the operant dielectric relaxation mechanisms of the constituent components. Although dielectric properties of pure melting gels have been previously

studied^[35], the intrinsic sample variation of measuring these gels has not been evaluated. To determine the limitations of this dielectric characterization, duplicate measurements of the same samples were collected at different instances under identical conditions. To quantify the variation in these measurements, the statistical half range ($\max/2 - \min/2$) expressed as a percentage relative to the average value was used to construct bounded intervals. In **Figure 54**, the frequency dependence of dielectric constant variation is seen to be minuscule for both Par-gels and Micro-gels.

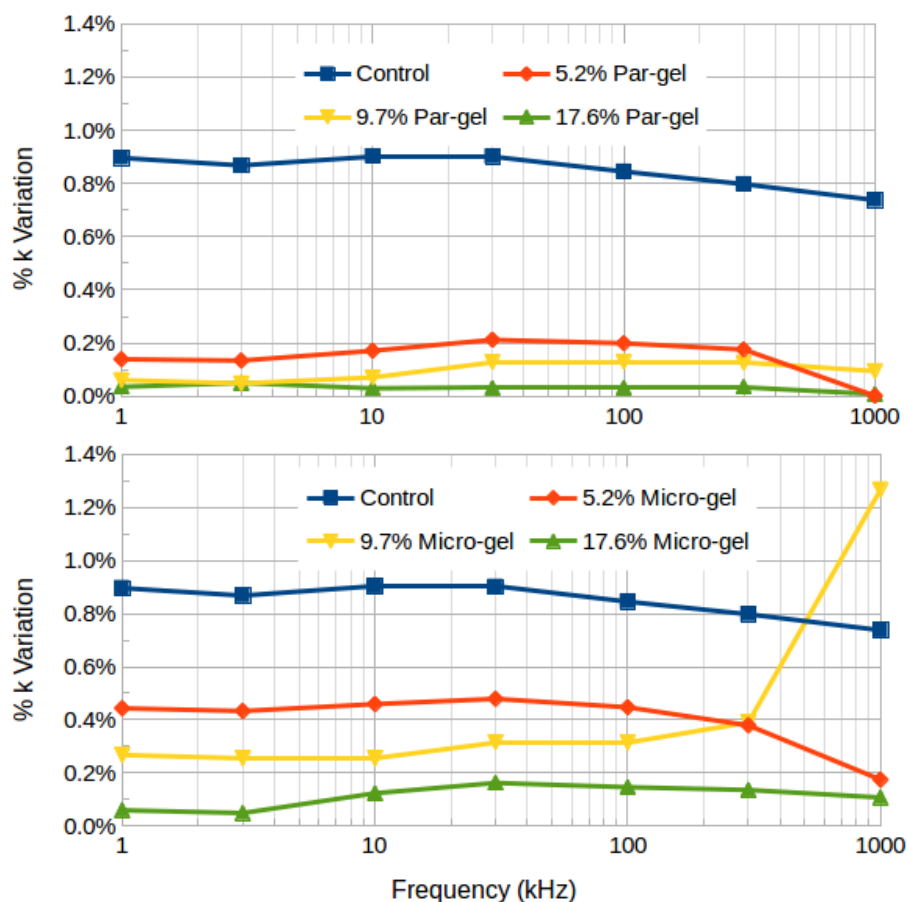


Figure 54: Dielectric Constant Duplicate Measurement Variation of Wax-Gels

However, in **Figure 55**, the variation in dissipation factor of some Wax-gels is shown to increase dramatically with frequency.

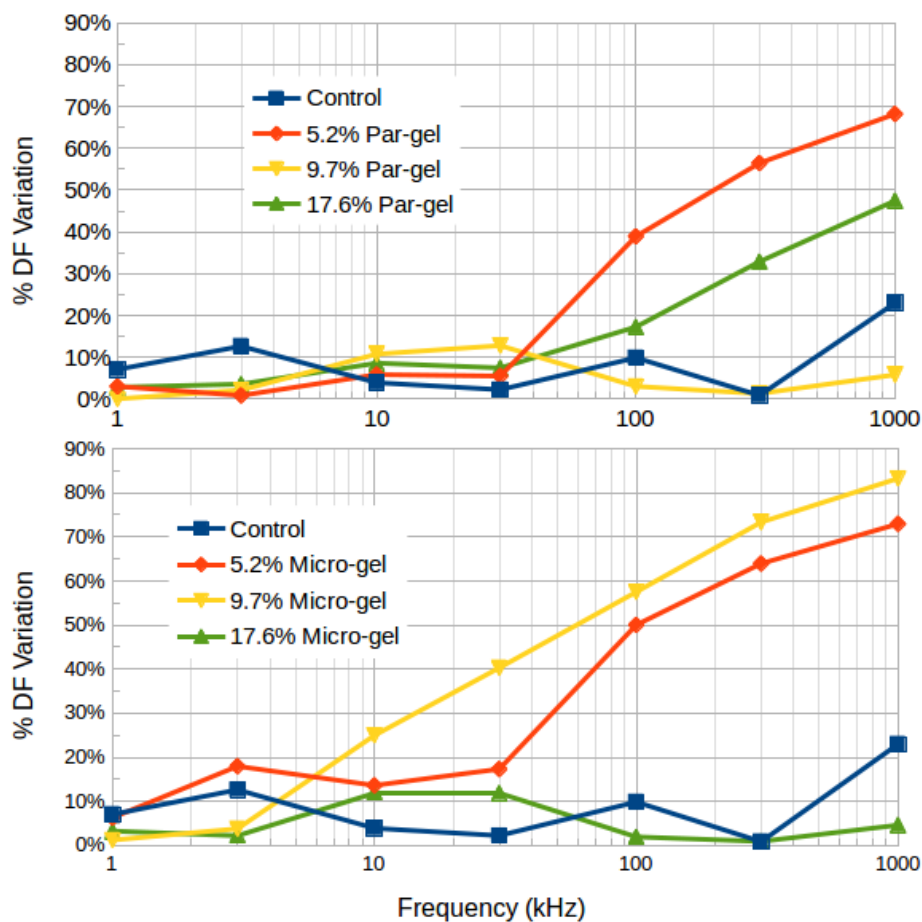


Figure 55: Dissipation Factor Duplicate Measurement Variation of Wax-Gels

For unique, independent samples derived from the same respective gel batches, the replication variation of dielectric constant measurements is illustrated below in **Figure 56**.

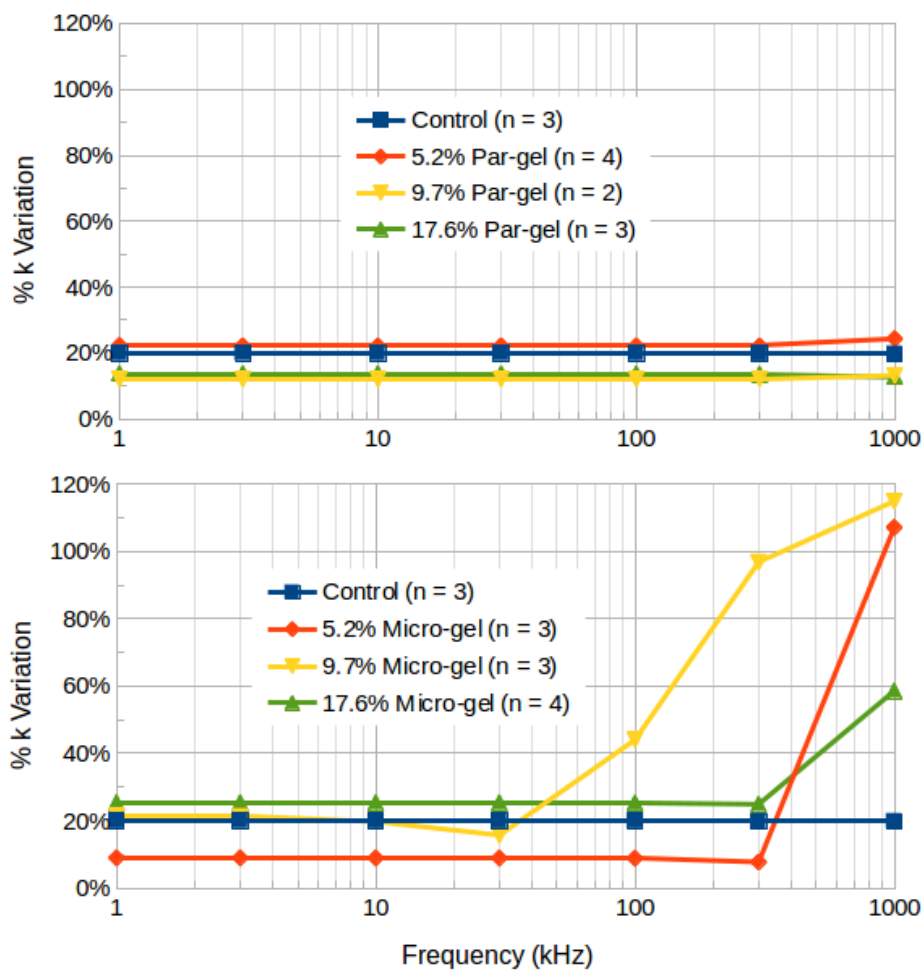


Figure 56: Dielectric Constant Replicated Measurement Variation of Wax-Gels

Just as with duplication measurement variation, **Figure 57** illustrates a very strong frequency dependence for the replication variation of dissipation factor measurements.

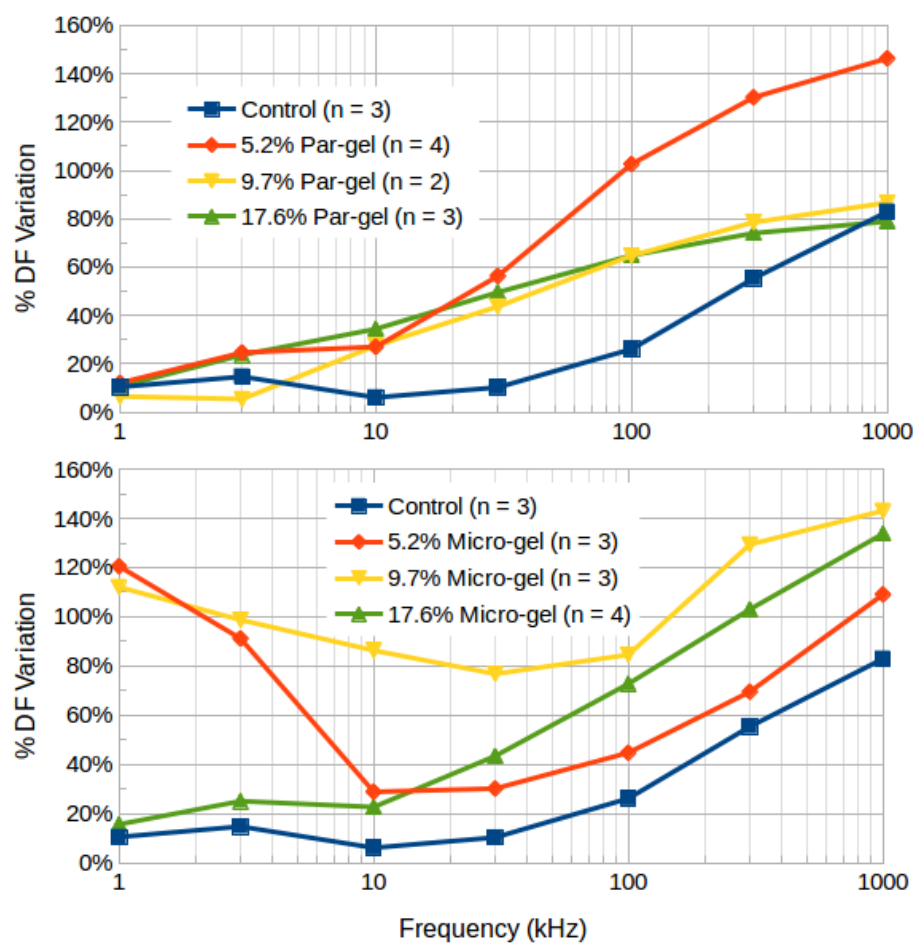


Figure 57: Dissipation Factor Replicated Measurement Variation of Wax-Gels

By applying these percent variations as error bars to the average dielectric measurements, the compositional dependence of these values can be resolved. In **Figures 58-59**, dielectric constant and dissipation factor are plotted at various scalings to illustrate the volatility of extreme measurements.

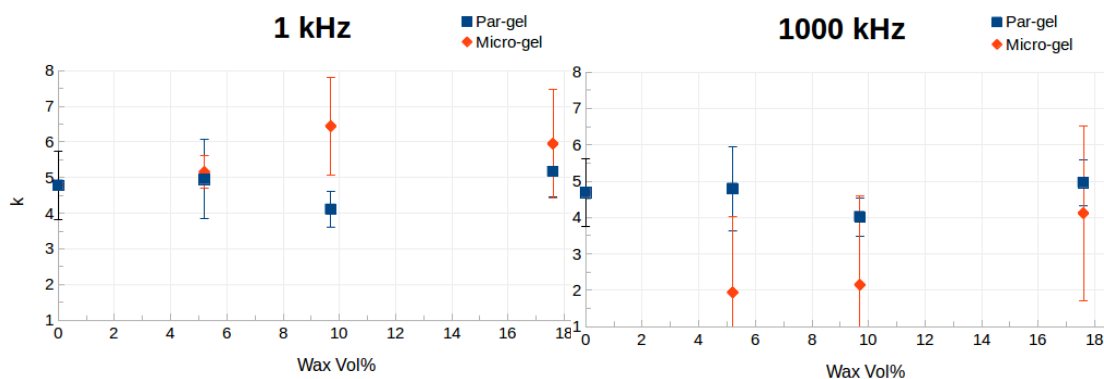


Figure 58: Dielectric Constant Measured Ranges of Wax-Gels

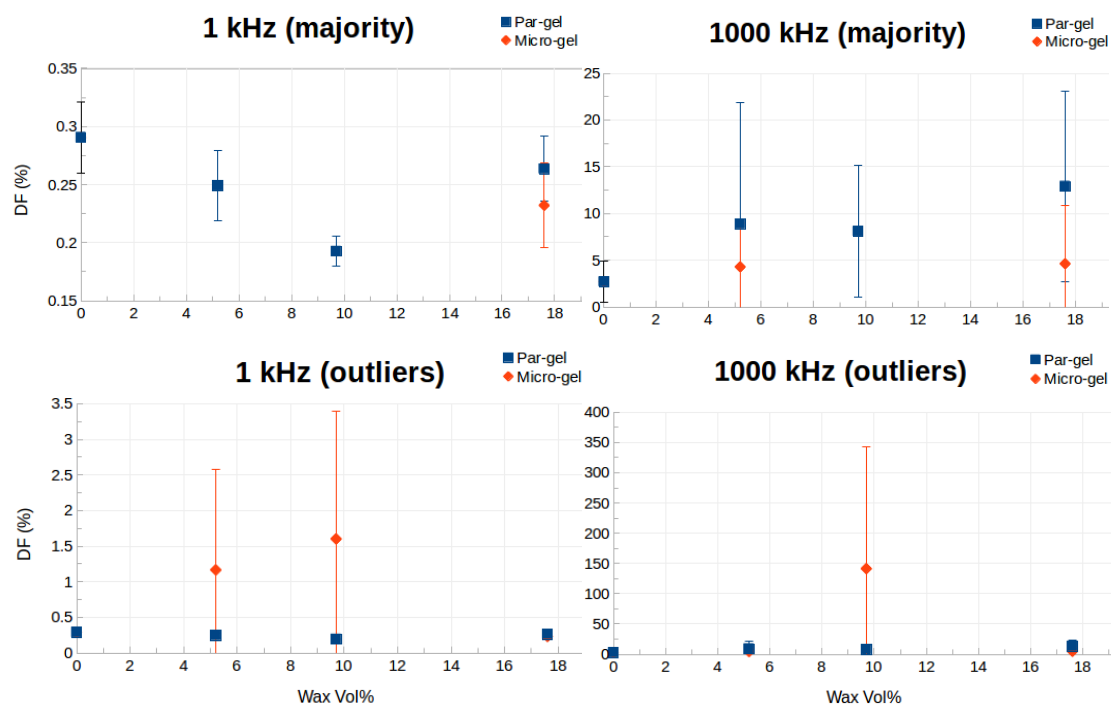


Figure 59: Dissipation Factor Measured Ranges of Wax-Gels

Based off these measurements, it is clear that any subtle variation in dielectric behavior across varying wax-gel compositions cannot be feasibly quantified. However,

relative to the control (0 wax vol%), Par-Gels are confirmed to be invariant to wax content under these conditions. Nevertheless, Micro-gels overlap significantly with the Par-gel ranges, but possess abnormal volatility.

4.4.2 EFFECT OF THERMAL TREATMENTS

In terms of thermal degradation, it was empirically determined that $\sim 120^{\circ}\text{C}$ was the onset of pyrolysis for these waxes, where yellowing would occur above this threshold. Below this temperature, the wax would remain stable almost indefinitely. Hence, prolonged exposure at the consolidation temperature of $\sim 175^{\circ}\text{C}$ leads to observable thermal degradation (as previously seen in **Figures 16-19**). To study the effect of this thermal degradation on these wax-gels, samples were cumulatively heated at the consolidation temperature ($\sim 175 \pm 5^{\circ}\text{C}$) in two day increments. After each increment, the dielectric behavior of these samples were remeasured and additional heating cycles were repeated until each sample was exposed to a cumulative total of eight days at the consolidation temperature.

Based off the measurement variation results, it is clear that the absolute dissipation factor can be feasibly quantified for most wax-gels at low frequencies. However, due to significant thickness measurements errors ($\sim 20\text{-}30\%$), only the relative dielectric constant can be accurately estimated. Therefore, to quantify the effect of cumulative thermal cycling, the change in dielectric constant with respect to heat

treatment duration or “dk/dt” was used. Combined with the dissipation factor, the thermal history dependence of the dielectric behavior of these wax-gels can be thoroughly characterized. For dk/dt, the thermo-dielectric behavior of these wax-gels is summarized below in **Figure 60**.

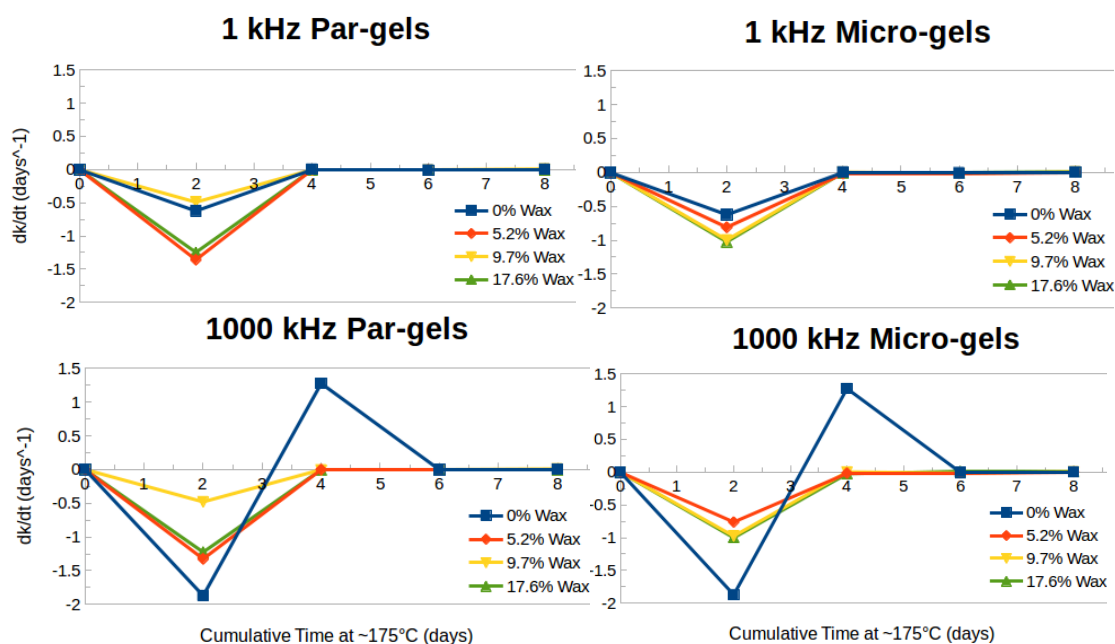
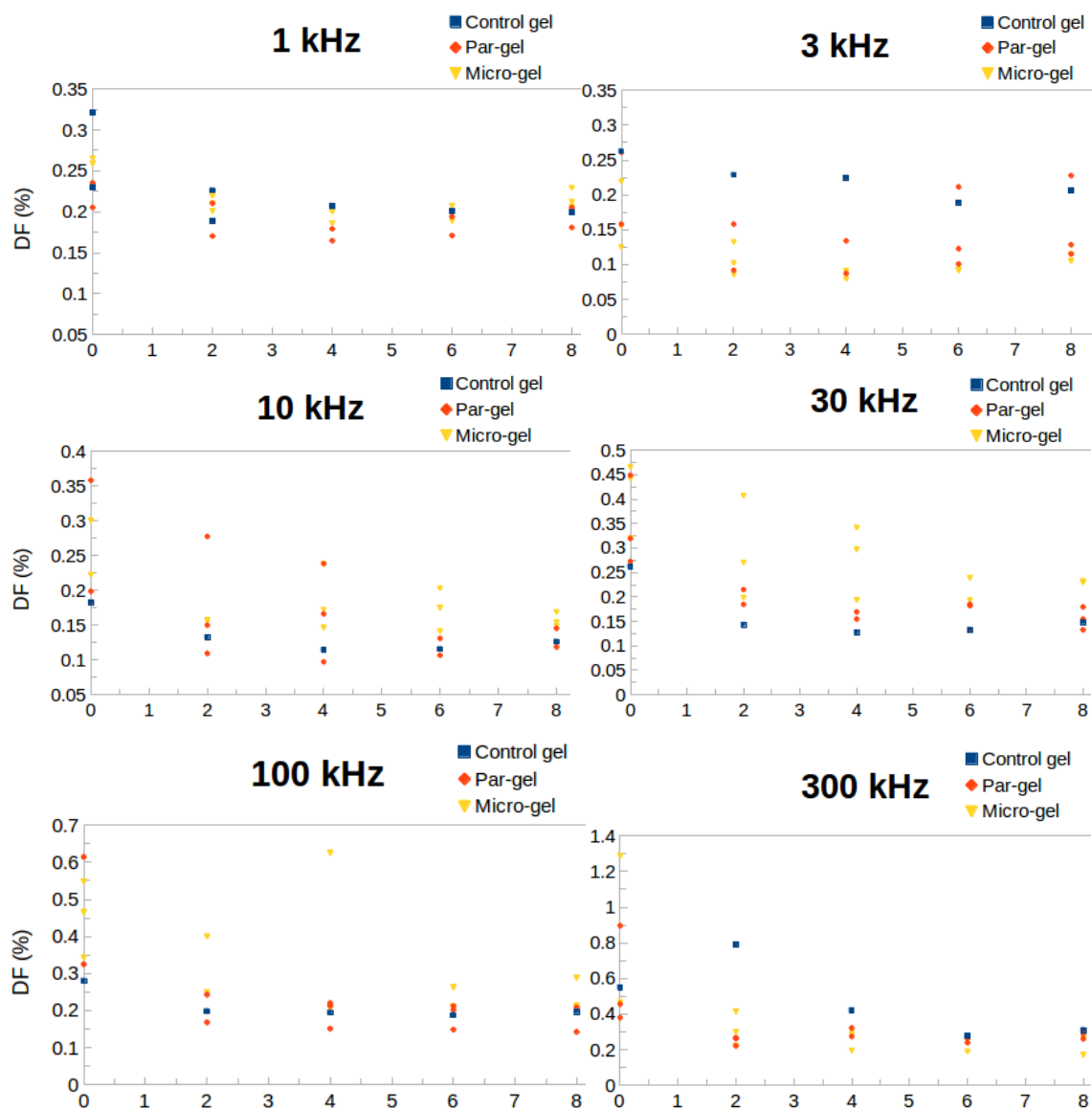


Figure 60: dk/dt variation of wax-gels during cumulative thermal cycling

These results are complemented by the thermo-dielectric variation in dissipation factor in **Figure 61**, where the wax volume fractions were pooled for each wax type to visualize the raw spread in the data (assuming negligible wax content dependence).



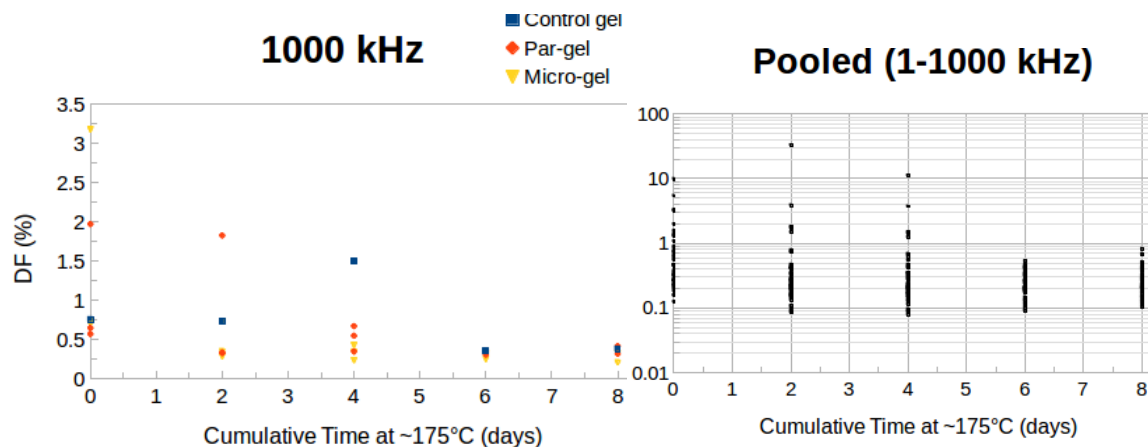


Figure 61: Dissipation factor variation of wax-gels during cumulative thermal cycling

V. DISCUSSION

5.1 PROFILOMETRY

Based on **Figure 8 and Table 3**, which present the roughness parameters Ra (arithmetic average roughness) and TIR (total indicator reading), it is clear that there are no significant statistical differences between the roughness of Par-gels and the control gel (0% wax). Thus, the surface features in **Figure 7** are submerged paraffin wax particles that do not influence the roughness of the gel phase. Nevertheless, in **Figure 9 and Table 4**, Micro-gels have the same range of roughness parameters as Par-gels, but with a distinct proportion of extreme values. Although there is no discernible dependence on wax volume, it is clear that the presence of microcrystalline wax produces the recorded

values. Using optical and SEM analysis, the source of these extreme roughness values are visible in **Figures 13-14 and Figures 37-39**. These micrographs show surface segregated, microcrystalline wax islands. In addition to the roughness due to wax islands and gel, **Figure 6** shows an undulating surface topography with wrinkles and folds. These surface features result from thermal mismatch, surface tension differences and elastic modulus differences between the wax and the gel.^[35]

Surface segregation is more prominent in Micro-gels than Par-gels. The difference is attributed to the difference in stability of wax emulsions according to the orientation and packing of polymer chains along a surfactant-adsorbed interface.^[36] Given that the branched hydrocarbons in microcrystalline wax are more difficult to orient and pack than the linear hydrocarbons in paraffin wax, it is reasonable to say that Micro-gel emulsions are less stable.

5.2 OPTICAL MICROSCOPY

5.2.1 REPRESENTATIVE MICROGRAPHS

For the Par-gels in **Figures 10-12**, all samples show a wide range of dispersed wax microparticles. Larger particles were less spherical than smaller ones. The larger particles do not appear to be agglomerates of smaller particles, although it is likely that some coalescence has occurred.^[37] In the Micro-gel micrographs of **Figures 13 and 14**, wax microparticles are found as well, with more surface segregation than in Par-gels. In

Figure 15, for the sample with 17.6% wax, the microparticles coalesced into large, submerged wax pools.

5.2.2 THERMALLY DEGRADED SAMPLES

In **Figure 16** of a fracture surface, the edges show discoloration associated with the pyrolysis of leaked wax. This discoloration is seen in the largest wax particles, but not in the microparticles. Additionally, in **Figure 17**, the effects of thermal degradation are not uniform across the sample. Under UV light, in **Figure 18** and 100x magnification in **Figure 19**, nonuniform particle densities and optical absorption are evident.

These dark features are attributed to brown carbon, which is an intermediate product of pyrolysis before black char.^[38] Based on these observations, higher wax loadings generally produce more wax pools and lead to less thermally stable composites. Nonetheless, thermally stable wax microparticles persist in all compositions. Thermal stability is related to particle size, with smaller particles being more stable.

5.2.3 PARTICLE SIZE ANALYSIS

Visually from **Figures 22 and 23** and statistically from **Table 5**, it is evident that Par-gel empirical distributions functions (EDF) differ between wax contents, but not as much as those for Micro-gel. Hence, it is better to compare EDFs for a specific wax composition than rely on pooled values. The algorithm used to model these EDFs follows the same general principles as other distribution modeling methodologies.^[39] The

alternative is to use conventional modeling on a truncated dataset, where particles are confined to an artificial limit that is greater than the instrument resolution. This would circumvent the graded steps in **Figure 25**, but would constrict the effective fitting range and reduce the sample size. Moreover, the fitting parameters would change as a function of this artificial limit. Thus, the piecewise, Monte Carlo modeling methodology was employed to avoid these issues and make best use of this complete set of data.

The cumulative distribution function (CDF) best fits derived in the **Figures 26-27 and Appendix 10** appear robust for both the upper and lower bounds of the EDFs. The Weibull distribution was used for convenience to model the lower bounds. However, the Gamma distribution used to model the upper bounds has physical significance.

The Gamma distribution is used to model droplet particle sizes, but is mathematically more difficult to manipulate than common models, such as log-normal or Weibull distributions.^[40-41] Gamma processes occur naturally from the summation of exponential distributions.^[42] These exponential distributions have relevant physical significance, as they are solutions to the partial differential equations dictating Ostwald ripening in emulsion kinetics.^[43] Therefore, the best estimation for the particle size distribution of these wax-gels is a Gamma distribution.

Using the upper Gamma fits and their respective medians, it is apparent in **Tables 8 and 9** and **Figure 29** that these CDFs systemically underestimate the EDF particle size data. In addition, the Gamma fits show that Micro-gels have higher median particle sizes than Par-gels. This is consistent with the notion that Micro-gels are less stable than Par-

gels, since the Par-gels would remain dispersed while the Micro-gels would tend to show ripening. In either case, the data for both Micro-gels and Par-gels lie in a well-bounded, linear range of parameters in **Figure 28**. Notice that the sample size of Micro-gel particles is almost 10 times smaller than that of the Par-gels. The lower sample size for microcrystalline wax particles is likely due to surface segregation and pooling, which are not included in this analysis.

5.3 SEM ANALYSIS

5.3.1 REPRESENTATIVE MICROGRAPHS

In **Figure 30**, the fractured pieces of melting gel are fully dense, showing no porosity. However, in **Figures 31-36**, all samples show spherical cavities left by particles of wax. There is no indication that wax particles agglomerated. In SEM images, where the smaller particles are visible, most particles appear to be spherical. No irregular pools of submerged wax are seen in the SEM micrographs, although they are seen in optical microscopy.

5.3.2 PROFILOMETRY SAMPLE

In **Figures 37-39**, the same Micro-gel wax islands found in optical microscopy and detected in profilometry are found in the SEM. Their microscopic roughness and abundance are seen in these micrographs. Similar morphological features have been reported before in “TEOS-wax” sol-gel composites.^[44]

5.3.3 PARTICLE SIZE ANALYSIS

The SEM EDFs in **Figure 41** exhibit the same sample size disparity and relative shapes as the optical EDFs of **Figure 21**. However, in **Figures 42 and 43**, the smaller sample sizes for SEM micrographs, compared to optical micrographs, leads to noisier EDF curves. Nevertheless, best fits were found using the same methodology as the optical analysis. The most notable difference is that the SEM range particle size is about an order of magnitude smaller than for the optical range. As a result, the underestimation bias of the medians is significantly less in **Table 13** and **Figure 48** than in the previous optical analysis. Therefore, despite lower sample sizes, these Gamma fits better predict the raw data within this tighter particle size range.

5.3.4 COMPARISON WITH OPTICAL PARTICLE SIZE DISTRIBUTIONS

Through the extrapolation of the optical CDFs into the constrained domain of the SEM CDFs in **Figures 49 and 50**, it appears optical CDFs overlap with the majority of the SEM models. The only exception is the 5.2% Micro-gel, which has the poorest fit because it has the lowest sample size ($n = 71$). Regardless, wax-gel composites can be modeled from sub-micron to almost millimeter length scales using this optical CDF extrapolation.

Using this extrapolation, the corresponding PDFs in **Figure 52** share the same extreme left skewness as the pooled histograms in **Figures 24 and 44**. When normalized to relative wax volume fractions in **Figure 53**, it is clear the majority of the wax volume

is derived from microparticles between ~5-50 microns. This suggests that large, thermally susceptible wax particles (~100+ microns) only make up a small fraction of the total wax volume in wax-gels. Thus, based on this particle size analysis and previous thermal degradation testing, these wax-gels can be the basis for thermally stable phase change materials (PCM).

5.4 DIELECTRIC CHARACTERIZATION

5.4.1 DIELECTRIC BEHAVIOR OF WAX-GELS

In **Figure 54**, the variation in measured dielectric constants is small, less than 1.4% for all wax-gels and frequencies. However, it is interesting to note that the variation is smaller for high wax contents than for low wax contents. This suggests that the gel phase is less consistent than the wax phase. In other words, the gel phase is more chemically complex than the wax phase.

The variation in measured dissipation factors increases at higher frequencies. Since these measurements vary little at lower frequencies, contact issues are ruled out. The lossiest peak frequencies are found beyond 1 MHz, and appear to reflect molecular weight distributions in the gel.

When replicated with unique samples, the dielectric constant was about the same across all the Par-gel compositions and frequencies. In contrast, the Micro-gels showed higher values at higher RF frequencies. Likewise, the Micro-gels showed a wide range of dissipation factors both at low and high frequencies.

Since both the Par-gels and control gels do not share the behavior of the Micro-gels, it suggests that only the Micro-gels have structures that influence the dissipation factor. Given that microcrystalline wax on its own does not exhibit this behavior, it is the combination of Micro-gels which gives rise to this behavior. At this time, the mechanisms at the gel-surfactant/microcrystalline wax interfaces are not known. Nevertheless, it is clear that the Par-gels and Micro-gels exhibit different interface contributions to the dielectric behavior.

In **Figures 58 and 59**, it is seen that the control gel dielectric behavior is similar to what is observed in other melting gels.^[45] In general, wax-gels show the same dielectric behavior as melting gels. As such, it is not possible to separate the effects of the wax from the gel. One noticeable difference is that Micro-gels have some outlier values.

5.4.2 EFFECT OF THERMAL TREATMENTS

In **Figure 60**, where the variations in dielectric constant over 8 days are plotted, all wax-gels showed a negative deviation after 2 days of heat treatment. This decrease in dielectric constant occurs for all compositions and frequencies. This is likely due to removal of volatile species, such as water and ethanol, and crosslinking associated with the consolidation process. Most melting gels by themselves take about 1 day to consolidate.^[46] For these wax-gel composites, changes may persist for 6 days, as indicated by changing dielectric constant. After 8 days, no further changes in dielectric constant were measured. This dielectric stability indicates that crosslinking is complete.

The dk/dt plots are supported by the dissipation factor results over the same 8 day period, plotted in **Figure 61**. Between ~ 10 -1000 kHz, all wax-gel compositions have converging values with increasing consolidation time. Between 0 and 4 days, there is a range of about 3 orders of magnitude. By 6 days of cumulative heat treatments, the dissipation factors fall within one order of magnitude. At first, the samples contain ethoxy and hydroxyl groups, which contribute to loss, but further heat treatment removes these species while the gels crosslink. As a result, the evolution of the dielectric behavior of wax-gel composites can be used as a way to determine when the structure has stabilized.

VI. SUMMARY AND CONCLUSIONS

1. Both paraffin and microcrystalline waxes were successfully dispersed as microparticles in a melting gel matrix through in-situ emulsification with a silicone-based surfactant.
2. The emulsion stability of paraffin wax is better than for microcrystalline wax under these processing conditions.
3. The volume fraction of wax does not influence Par-gel roughness. However, Micro-gels exhibit rough, surface segregated wax islands.
4. Micro-gels with a wax volume of 17.6 vol% exceeded the limit of incorporation, leading to segregated pools of wax.

5. The particle distribution in wax-gels is best fitted with a Gamma distribution, which is characteristic of the break up of a fluid droplet.
6. Micro-gels exhibit larger median particle sizes than Par-gels.
7. The majority of the wax volume in both cases is attributed to microparticles between ~5-50 microns in diameter.
8. The dielectric properties show little variation with wax content from 0-17.6 vol%.
9. Larger variations in dielectric properties were seen between the wax types, paraffin vs. microcrystalline wax.
10. Between ~6-8 days of thermal consolidation were needed to reach the final dielectric behavior in the wax-gel composites.

VII. SUGGESTIONS FOR FUTURE WORK

7.1 CHARACTERIZATION

To better understand the effect of wax volume fraction and type on composite dielectric strength, electrical resistivity, and thermal conductivity should be measured. In addition, laser diffraction and static light scattering (SLS) would provide particle size information for comparison with the image analysis presented. Transmission electron microscopy (TEM) could be used to establish a lower bound for particle size ranges. Alternatively, an HF/H₂SO₄ acid etch can dissolve the gel matrix and extract the wax particles for sieve analysis. Lastly, optical microscopy videos of wax-gels during

thermally curing could capture emulsion/coalescence kinetics that produce these particle size distributions.

Dielectric characterization should be extended across a wider range of variables. For example, dielectric measurements collected in the microwave regime would provide greater insight into the constituent polarization mechanisms. Likewise, measuring the temperature dependence of the wax-gel dielectric behavior would enable activation energies for these polarization mechanisms to be estimated. Lastly, although no pyrolysis-specific dielectric changes were detected, UV-Vis/vibrational spectroscopies and modulated differential scanning calorimetry (mDSC) could offer more insight as to the degree of thermal degradation associated with various heat treatments.

7.2 SYNTHESIS

Improved processing techniques can expand the available wax-gel compositions. For instance, purer molecular weight and special synthetic wax blends could be used to achieve superior, tunable properties. Additionally, more oleophilic melting gel compositions may be capable of dissolving wax without surfactants and could be engineered to consolidate at lower temperatures for minimal wax thermal degradation.

To overcome the high viscosity of greater wax loadings, dilution of gels with compatible solvents and simultaneous stirring/ultrasonication would be employed. The solvent type, concentration, stirring RPM, and ultrasonication frequencies/ power would be key parameters to study with regard to particle size. Although more effective

surfactants are available, their better emulsifying properties generally tend to trade-off with thermal stability. Similarly, using high specific surface area fillers (i.e. fumed silica or powdered aerogel) enable greater wax loadings, but yield less thermally stable composites. Thus, a wider range of wax-gel compositions is possible, although there are always compromises.

7.3 THERMAL APPLICATIONS

A possible application for these wax-gels is their use as an adhesive in aerospace electronics. Since high temperatures and outgassing are concerns in aerospace-grade electronics, these wax-gels may be able to compete with epoxies. Moreover, the fact that wax-gels are phase-change materials points to their use for thermal management in aerospace electronics, which rely on PCM heat sinks and radiative cooling to operate in vacuum environments.^[46-48] As an adhesive coating, wax-gels could be used as thermal underfill and staking compound for printed circuit boards (PCBs). Likewise, they may be used for thermal bonding, potting sensitive components, and as a PCM for heat sinks.

Additionally, due to their dielectric-thermal history behavior, these wax-gels may be used for measuring cumulative thermal degradation in engineering systems and products. Similar to how RFID tags can measure local thermal degradation in curing resin composites, wax-gel capacitors could be strategically placed to measure the thermal history of heat-sensitive regions.^[49] This would be useful in monitoring polymer components, where direct temperature measurements are not practical. For example,

engineering plastics used in high temperature automotive/aerospace components, high power electronics, and industrial equipment are generally replaced when creep failure or obvious pyrolysis is observed.^[50] By “waiting to fail” in these complex systems, a cascade of catastrophic failures in other components may occur, requiring expensive replacements or repair work. Nevertheless, monitoring the temperature of every plastic component simultaneously and continuously is not realistic. Instead, by using these wax-gel thermal degradation sensors, preventative maintenance measures can be taken to maximize lifetime performance.

7.4 ELECTRO-OPTICAL APPLICATIONS

For low k , low-loss applications in the RF frequency range, wax-gel composites are suitable for RF filters and audio capacitors in high power circuits.^[51-53] In addition to electret applications, electrohydrodynamic energy harvesting may be feasible with biased molten wax particles that are oscillating from applied mechanical vibrations.^[54] These vibrations would induce a variable AC voltage that could be used for sensing or energy harvesting. This could be extended to an encapsulated ferrofluid biased by a magnetic field for sensing/energy harvesting as well.^[55]

Moreover, these wax-gels may serve as analog systems for developing composites with organic payloads that possess special optical properties. For example, organic laser dyes, liquid crystals, and OLED compounds could be dispersed in melting gels to obtain novel optical composites. With the increasing demand for materials that can

integrate organic/inorganic optical components, melting gels and other hybrid nanocomposites can play a role in advanced photonics.

7.5 OTHER APPLICATIONS

Due to the low density and high hydrogen content of wax, these wax-gel composites have unique potential as neutron radiation absorbing coatings in nuclear and aerospace applications.^[56] Additionally, the dispersed nature of these waxes could enable self-lubricating tribological coatings to be developed; this is where as the gel is abraded, exposed wax capsules are smeared and melted from friction to act as a built-in lubricant during wear.^[57] Similarly, the surface segregated wax bumps of Micro-gels could be engineered into lotus leaf-mimetic, hydrophobic coatings.^[58] Hence, it is clear these wax-gel composites offer many potential applications and opportunities to be explored.

VIII. REFERENCES

- [1] Klein, Lisa, Mario Aparicio, and Andrei Jitianu. *Handbook of Sol-Gel Science and Technology*. Cham: Springer International Publishing, 2019.
- [2] Pierre, Alain C. *Introduction to Sol-Gel Processing*. Boston: Kluwer Academic Publishers, 1998.
- [3] Brinker, C. Jeffrey., and George W. Scherer. *Sol-Gel Science: The Physics and Chemistry of Sol-Gel Processing*. Saint Louis: Elsevier Science, 2014.
- [4] Klein, Lisa C. “Sol-Gel Overview: Transparent, Microporous Silica, Its Synthesis and Characterization.” *Submolecular Glass Chemistry and Physics*, January 1991.
- [5] Ishizaki Kōzō, Sridhar Komarneni, and Makoto Nanko. *Porous Materials: Process Technology and Applications*. Dordrecht: Kluwer Academic, 1998.
- [6] Reed, James Stalford. *Principles of Ceramics Processing*. New York: Wiley, 1995.
- [7] Guglielmi, Massimo, Guido Kickelbick, and Alessandro Martucci. *Sol-Gel Nanocomposites*. Dordrecht: Springer, 2014.
- [8] Hrubesh, Lawrence W. “Aerogel Applications.” *Journal of Non-Crystalline Solids* (1998).
- [9] Attaia, Yosry A. *Sol-Gel Processing and Applications*. 1st ed. New York: Springer Science, 1994.
- [10] Olenick, Anthony J. “Silicones—Basic Chemistry and Selected Applications.” *Journal of Surfactants and Detergents* 3, no. 2 (2000).
- [11] Wolfgong, W. John, and Kirk Wiggins. “The Silicone Conundrum.” *Journal of Failure Analysis and Prevention* 10, no. 4 (November 2010).
- [12] Pomogailo, Anatolii D., and Vladimir N. Kestelman. *Metallopolymer Nanocomposites*. Berlin: Springer Berlin, 2014.
- [13] Klein, Lisa C., and Andrei Jitianu. “Organic–Inorganic Hybrid Melting Gels.” *Journal of Sol-Gel Science and Technology* 55, no. 1 (2010).

- [14] Klein, Lisa C., Stamatia Kallontzi, Laura Fabris, Andrei Jitianu, Caillin Ryan, Mario Aparicio, Lin Lei, and Jonathon P. Singer. "Applications of Melting Gels." *Journal of Sol-Gel Science and Technology* 89, no. 1 (2018).
- [15] Jitianu, Andrei, Glenn Amatuucci, and Lisa C. Klein. "Phenyl-Substituted Siloxane Hybrid Gels That Soften Below 140°C." *Journal of the American Ceramic Society* 92, no. 1 (2009).
- [16] Jitianu, Andrei, Guadalupe Gonzalez, and Lisa C. Klein. "Hybrid Sol-Gel Glasses with Glass-Transition Temperatures Below Room Temperature." *Journal of the American Ceramic Society* 98, no. 12 (2015).
- [17] Melton, Laurence, Fereidoon Shahidi, and Peter Varelis, eds. *Encyclopedia of Food Chemistry*. Academic Press, 2019.
- [18] Ganeeva, Yulia M., Tatiana N. Yusupova, and Gennady V. Romanov. "Waxes in Asphaltenes of Crude Oils and Wax Deposits." *Petroleum Science* 13, no. 4 (2016).
- [19] Alnaimat, Fadi, and Mohammed Ziauddin. "Wax Deposition and Prediction in Petroleum Pipelines." *Journal of Petroleum Science and Engineering* 184 (2020).
- [20] Kant, Karunesh, A. Shukla, and Atul Sharma. "Advancement in Phase Change Materials for Thermal Energy Storage Applications." *Solar Energy Materials and Solar Cells* 172 (2017).
- [21] Agyenim, Francis, Neil Hewitt, Philip Eames, and Mervyn Smyth. "A Review of Materials, Heat Transfer and Phase Change Problem Formulation for Latent Heat Thermal Energy Storage Systems (LHTESS)." *Renewable and Sustainable Energy Reviews* 14, no. 2 (2010).
- [22] Hassan, Ahmed, Mohammad Shakeel Laghari, and Yasir Rashid. "Micro-Encapsulated Phase Change Materials: A Review of Encapsulation, Safety and Thermal Characteristics." *Sustainability* 8, no. 10 (2016).
- [23] Xiangfa, Zhou, Xiao Hanning, Feng Jian, Zhang Changrui, and Jiang Yonggang. "Pore Structure Modification of Silica Matrix Infiltrated with Paraffin as Phase Change Material." *Chemical Engineering Research and Design* 88, no. 8 (2010).

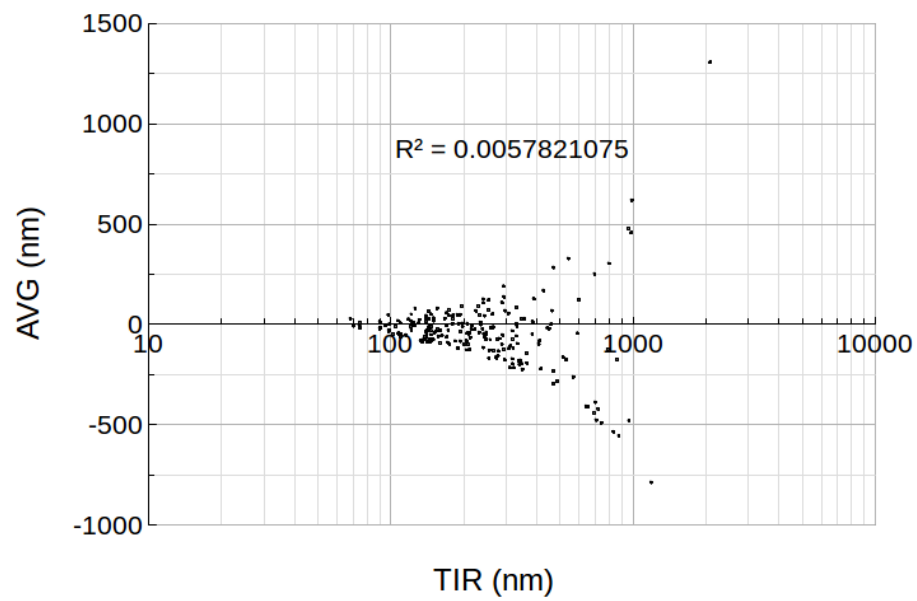
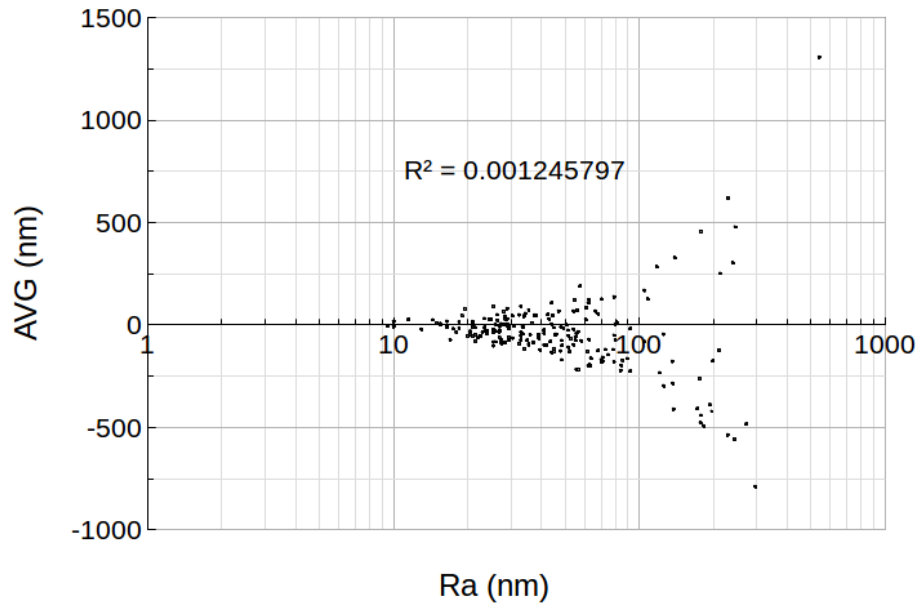
- [24] Serrano, Angel, Jesús Martín Del Campo, Nieves Peco, Juan F. Rodriguez, and Manuel Carmona. "Influence of Gelation Step for Preparing PEG–SiO₂ Shape-Stabilized Phase Change Materials by Sol–Gel Method." *Journal of Sol-Gel Science and Technology* 89, no. 3 (2018).
- [25] Feczko, Tivadar, László Trif, and Daniel Horák. "Latent Heat Storage by Silica-Coated Polymer Beads Containing Organic Phase Change Materials." *Solar Energy* 132 (2016).
- [26] Aftab, Waseem, Xinyu Huang, Wenhao Wu, Zibin Liang, Asif Mahmood, and Ruqiang Zou. "Nanoconfined Phase Change Materials for Thermal Energy Applications." *Energy & Environmental Science* 11, no. 6 (2018).
- [27] Beyhan, Beyza, Kemal Cellat, Yeliz Konuklu, Caner Gungor, Okan Karahan, Cengiz Dundar, and Halime Paksoy. "Robust Microencapsulated Phase Change Materials in Concrete Mixes for Sustainable Buildings." *International Journal of Energy Research* 41, no. 1 (2016).
- [28] Leong, Kin Yuen, Sue Ping Chew, Balamurugan A. Gurunathan, K.z. Ku Ahmad, and Hwai Chyuan Ong. "An Experimental Approach to Investigate Thermal Performance of Paraffin Wax and 1-Hexadecanol Based Heat Sinks for Cooling of Electronic System." *International Communications in Heat and Mass Transfer* 109 (2019).
- [29] Qian, Yong, Ping Wei, Pingkai Jiang, and Jiping Liu. "Preparation of Halogen-Free Flame Retardant Hybrid Paraffin Composites as Thermal Energy Storage Materials by in-Situ Sol–Gel Process." *Solar Energy Materials and Solar Cells* 107 (2012).
- [30] Mazur, K. "On the Relation between the Effective Charge of Carnauba Wax Electrets and the Polarization Temperature." *Journal of Electrostatics* 3, no. 4 (1977).
- [31] Mishra, Bhumika, and P. K. Khare. "ELECTRET: A DEVICE FOR MICROELECTRONIC APPLICATIONS." *Journal of Emerging Technologies and Innovative Research* 2, no. 1 (2015).
- [32] Bhushan, Bharat. *Modern Tribology Handbook*. Boca Raton, FL: CRC Press, 2001.
- [33] Young, Hugh D., Roger A. Freedman, A. Lewis Ford, and Hugh D. Young. *University Physics*. Boston, MA: Pearson, 2014.

- [34] Feldman, Yu., Yu. A. Gusev, and M. A. Vasilyeva. *DIELECTRIC RELAXATION PHENOMENA IN COMPLEX SYSTEMS*. Kazan University, 2012.
- [35] Gambino, Louis, Andrei Jitianu, and Lisa C. Klein. "Dielectric Behavior of Organically Modified Siloxane Melting Gels." *Journal of Non-Crystalline Solids* 358, no. 24 (2012).
- [36] Jin, Lihua. 2014. Mechanical Instabilities of Soft Materials: Creases, Wrinkles, Folds, and Ridges. Doctoral dissertation, Harvard University.
- [37] Taylor, Mark Stewart. "Stabilisation of Water-in-Oil Emulsions to Improve the Emollient Properties of Lipstick." *University of Birmingham*, January 2011.
- [38] Capek, Ignác. "Degradation of Kinetically-Stable o/w Emulsions." *Advances in Colloid and Interface Science* 107, no. 2-3 (2004).
- [39] Rathod, T.d., S.k. Sahu, M. Tiwari, and G.g. Pandit. "Direct Radiative Effect Due to Brownness in Organic Carbon Aerosols Generated from Biomass Combustion." *Journal of Quantitative Spectroscopy and Radiative Transfer* 185 (2016).
- [40] Kaczynski, W., L. Leemis, N. Loehr, and J. Mcqueston. "Nonparametric Random Variate Generation Using a Piecewise-Linear Cumulative Distribution Function." *Communications in Statistics - Simulation and Computation* 41, no. 4 (2011).
- [41] Vlachou, Maria C., Konstantinos A. Zacharias, Margaritis Kostoglou, and Thodoris D. Karapantsios. "Droplet Size Distributions Derived from Evolution of Oil Fraction during Phase Separation of Oil-in-Water Emulsions Tracked by Electrical Impedance Spectroscopy." *Colloids and Surfaces A: Physicochemical and Engineering Aspects* 586 (2020).
- [42] Jurado, Encarnación, Vicente Bravo, Fernando Camacho, José M. Vicaria, and Alejandro Fernández-Arteaga. "Estimation of the Distribution of Droplet Size, Interfacial Area and Volume in Emulsions." *Colloids and Surfaces A: Physicochemical and Engineering Aspects* 295, no. 1-3 (2007).
- [43] Devore, Jay L., and Kenneth N. Berk. *Modern Mathematical Statistics with Applications*. New York, NY: Springer New York, 2012.

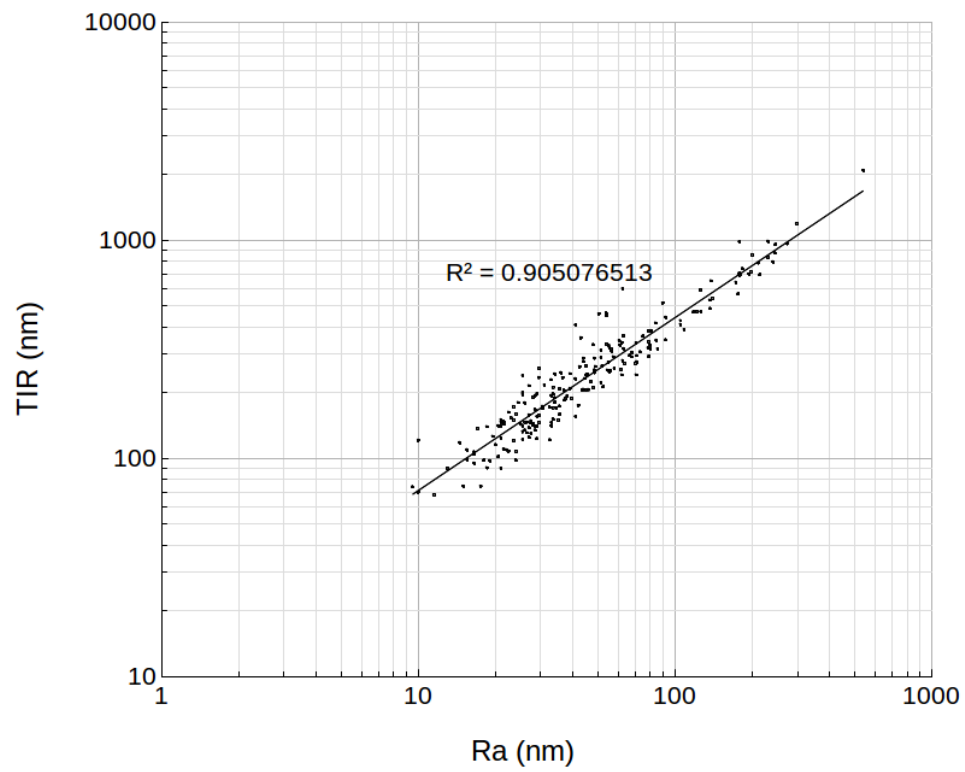
- [44] Madras, Giridhar, and Benjamin J. McCoy. "Distribution Kinetics of Ostwald Ripening at Large Volume Fraction and with Coalescence." *Journal of Colloid and Interface Science* 261, no. 2 (2003).
- [45] Tsvetkova, I. N., L. N. Krasil'Nikova, Y. V. Khoroshavina, A. S. Galushko, V. Frantsuzova Yu, A. K. Kychkin, and O. A. Shilova. "Sol-Gel Preparation of Protective and Decorative Coatings on Wood." *Journal of Sol-Gel Science and Technology* 92, no. 2 (2019).
- [46] Rashidi, S., H. Shamsabadi, J. A. Esfahani, and S. Harmand. "A Review on Potentials of Coupling PCM Storage Modules to Heat Pipes and Heat Pumps." *Journal of Thermal Analysis and Calorimetry*, February 2019.
- [47] Feng, P.h., B.c. Zhao, and R.z. Wang. "Thermophysical Heat Storage for Cooling, Heating, and Power Generation: A Review." *Applied Thermal Engineering* 166 (2020).
- [48] Timmerhaus, K. D. *Advances in Cryogenic Engineering*. Vol. 11. Springer US, 1995.
- [49] Veigt, Marius, Elisabeth Hardi, Michael Koerdt, Axel S. Herrmann, and Michael Freitag. "Curing Transponder – Integrating RFID Transponder into Glass Fiber-Reinforced Composites to Monitor the Curing of the Component." *Procedia Manufacturing* 24 (2018).
- [50] Fairhurst, A., M. Thommen, and C. Rytko. "Comparison of Short and Long Term Creep Testing in High Performance Polymers." *Polymer Testing* 78 (2019).
- [51] Mohan, P. V. Ananda. *VLSI Analog Filters: Active RC, OTA-C, and SC*. New York: Birkhäuser, 2013.
- [52] Song, Bang-Sup. *System-Level Techniques for Analog Performance Enhancement*. Cham: Springer International Publishing, 2018.
- [53] Rossing, Thomas D. *Springer Handbook of Acoustics*. New York, NY: Springer New York, 2014.
- [54] Smorodin, B. L. "The Effect of an Alternating Electric Field on the Liquid Dielectric Convection in a Horizontal Capacitor." *Technical Physics Letters* 27, no. 12 (2001).

- [55] Khairul, M.a., Elham Doroodchi, Reza Azizian, and Behdad Moghtaderi. “Advanced Applications of Tunable Ferrofluids in Energy Systems and Energy Harvesters: A Critical Review.” *Energy Conversion and Management* 149 (2017).
- [56] Uddin, Zaheer, Tariq Yasin, Muhammad Shafiq, Asif Raza, and Awais Zahur. “On the Physical, Chemical, and Neutron Shielding Properties of Polyethylene/Boron Carbide Composites.” *Radiation Physics and Chemistry* 166 (2020).
- [57] Armada, S., R. Schmid, S. Equey, I. Fagoaga, and N. Espallargas. “Liquid-Solid Self-Lubricated Coatings.” *Journal of Thermal Spray Technology* 22, no. 1 (2012)
- [58] Bhushan, Bharat. *Nanotribology and Nanomechanics: an Introduction*. Berlin: Springer, 2008.

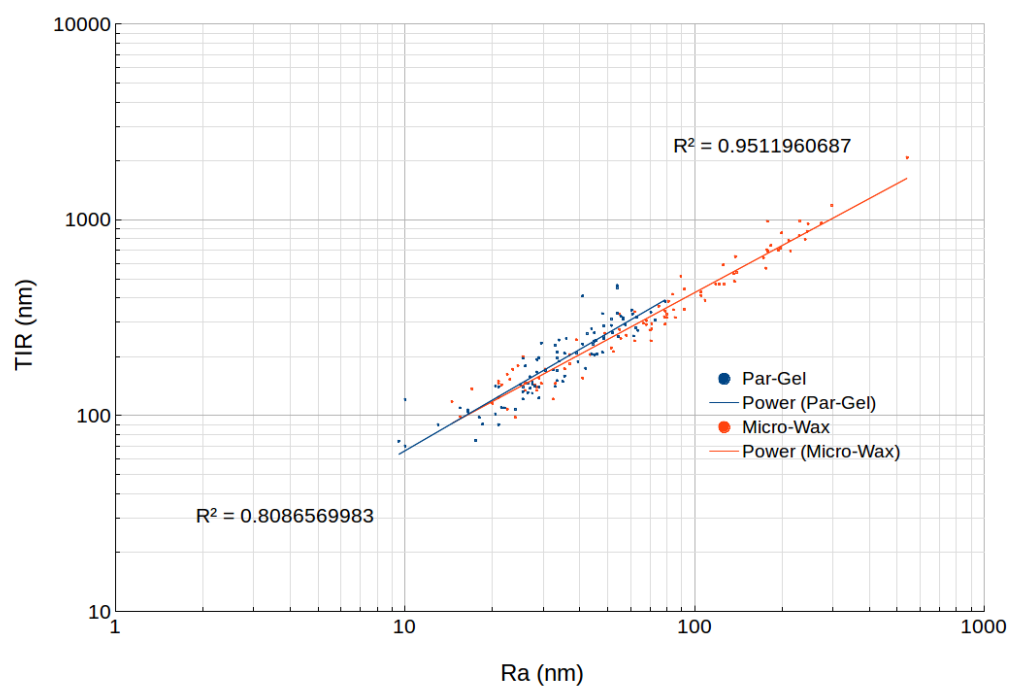
IX. APPENDIX



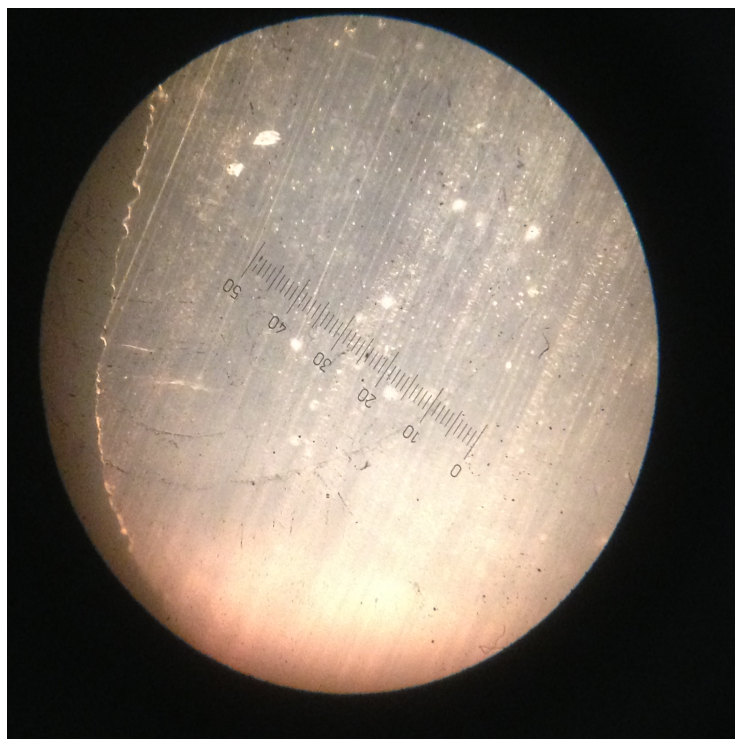
Appendix 1: Pooled Ra and TIR values plotted against AVG (n = 210, Linear R^2)



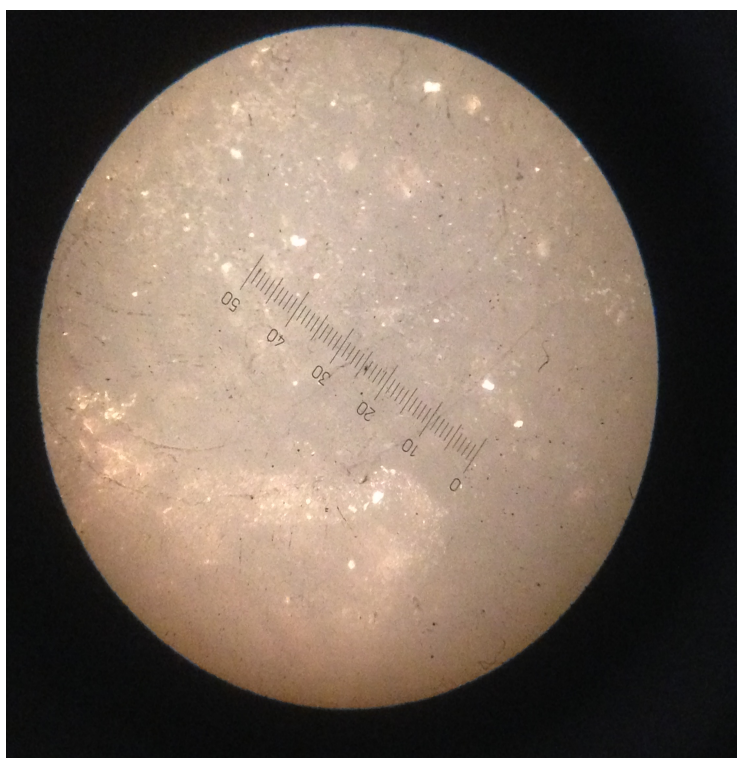
Appendix 2: Pooled TIR and Ra Correlation (n = 210, Power Model R^2 Fit)



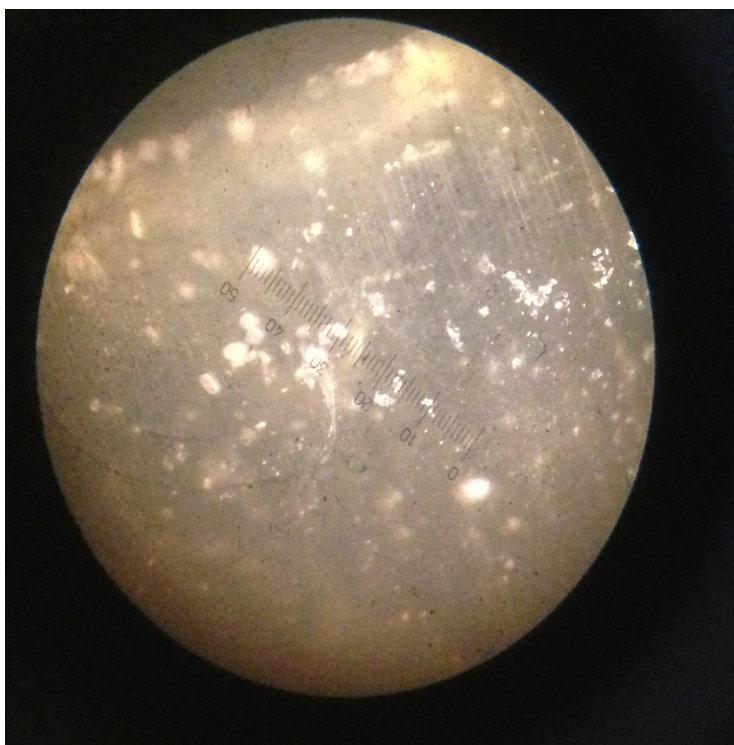
Appendix 3: TIR-Ra Clusters of Par/Micro-Gels (n = 90, each)



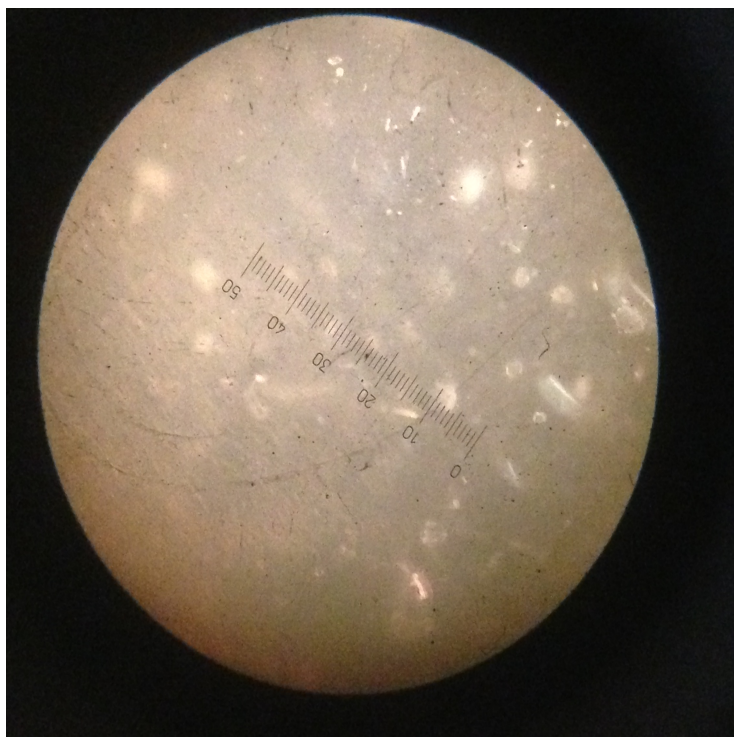
Appendix 4: Optical Micrograph of 5.2 vol% Par-Gel (100x)



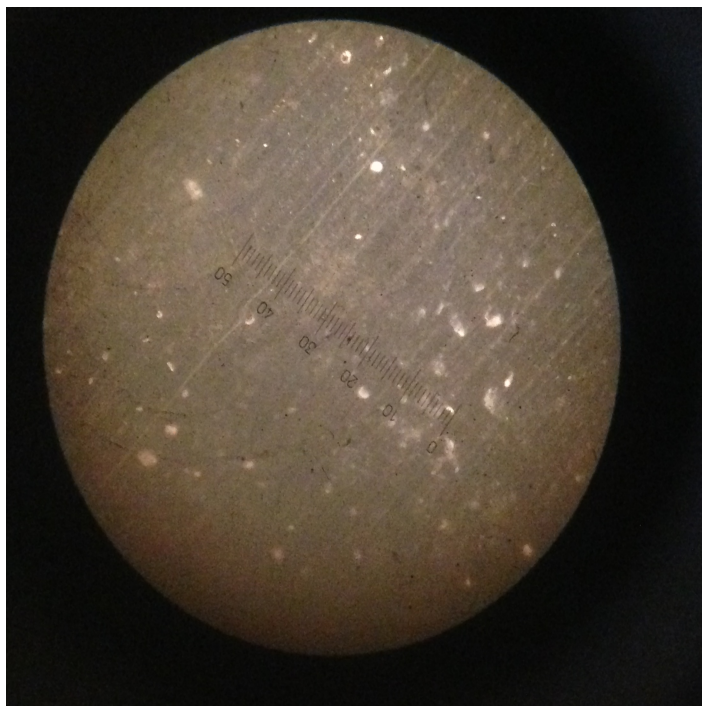
Appendix 5: Optical Micrograph of 9.7 vol% Par-Gel (100x)



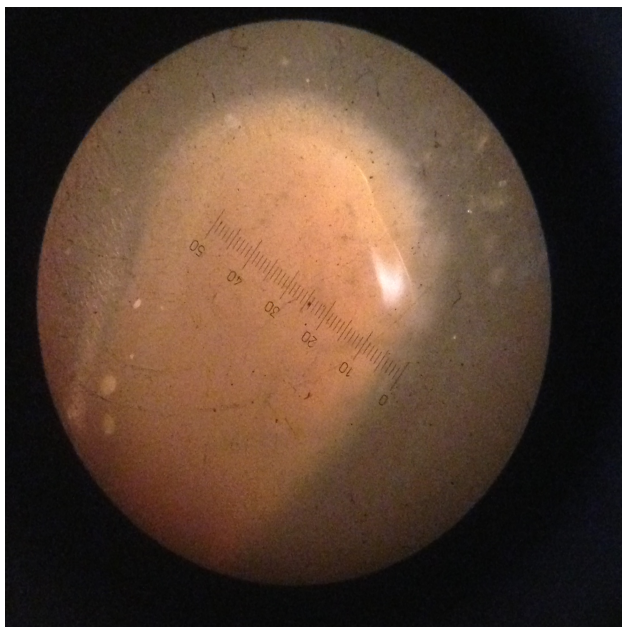
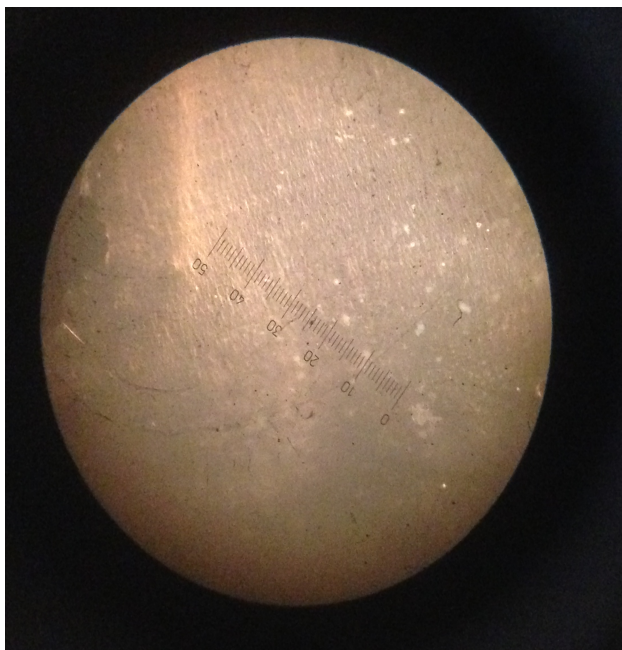
Appendix 6: Optical Micrograph of 17.6 vol% Par-Gel (100x)



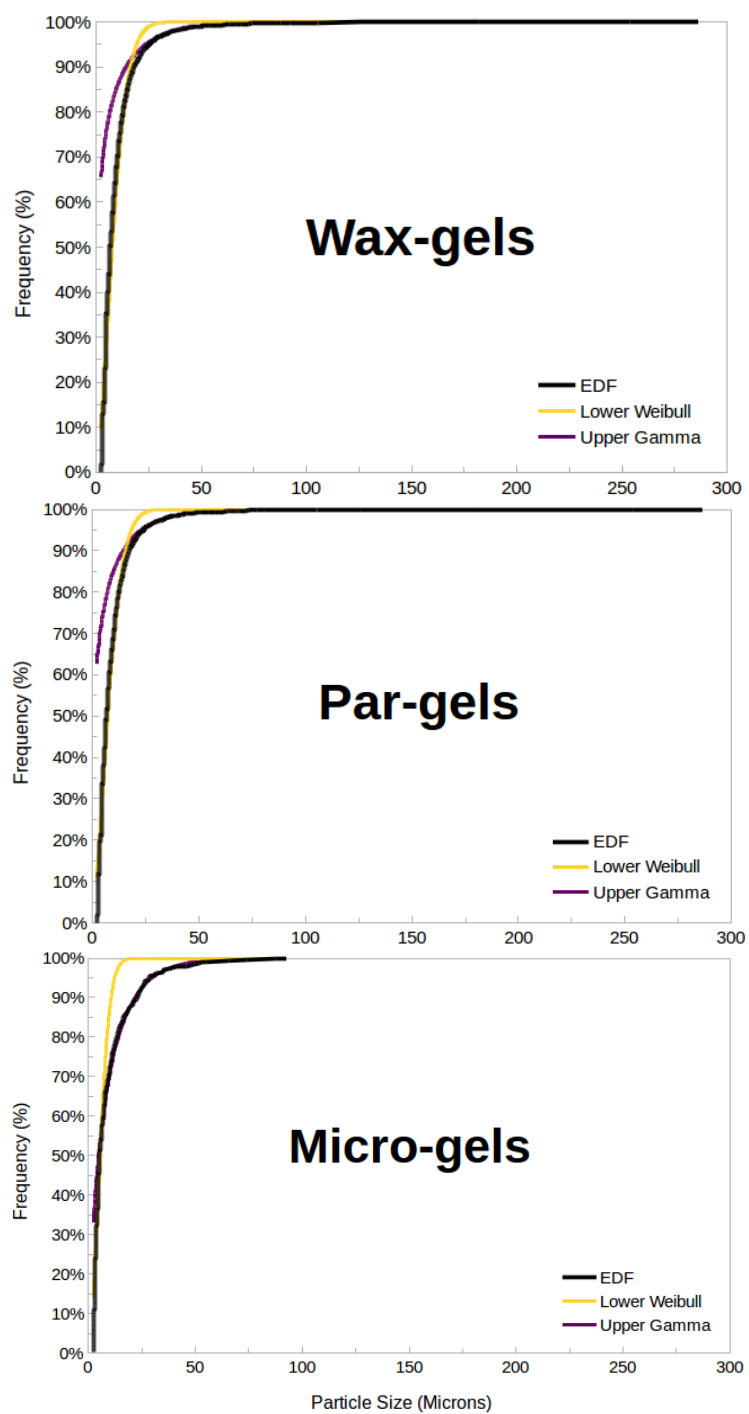
Appendix 7: Optical Micrograph of 5.2 vol% Micro-Gel (100x)



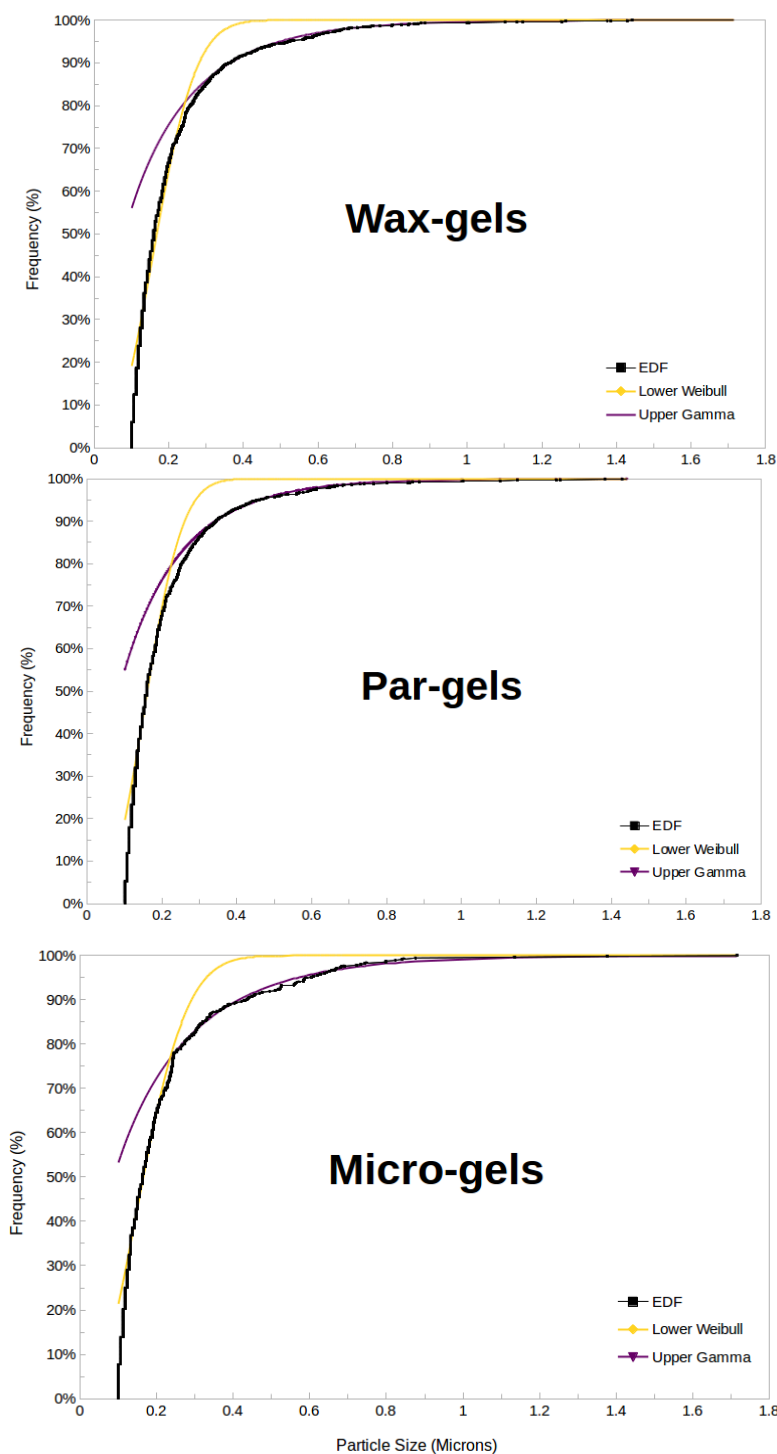
Appendix 8: Optical Micrograph of 9.7 vol% Micro-Gel (100x)



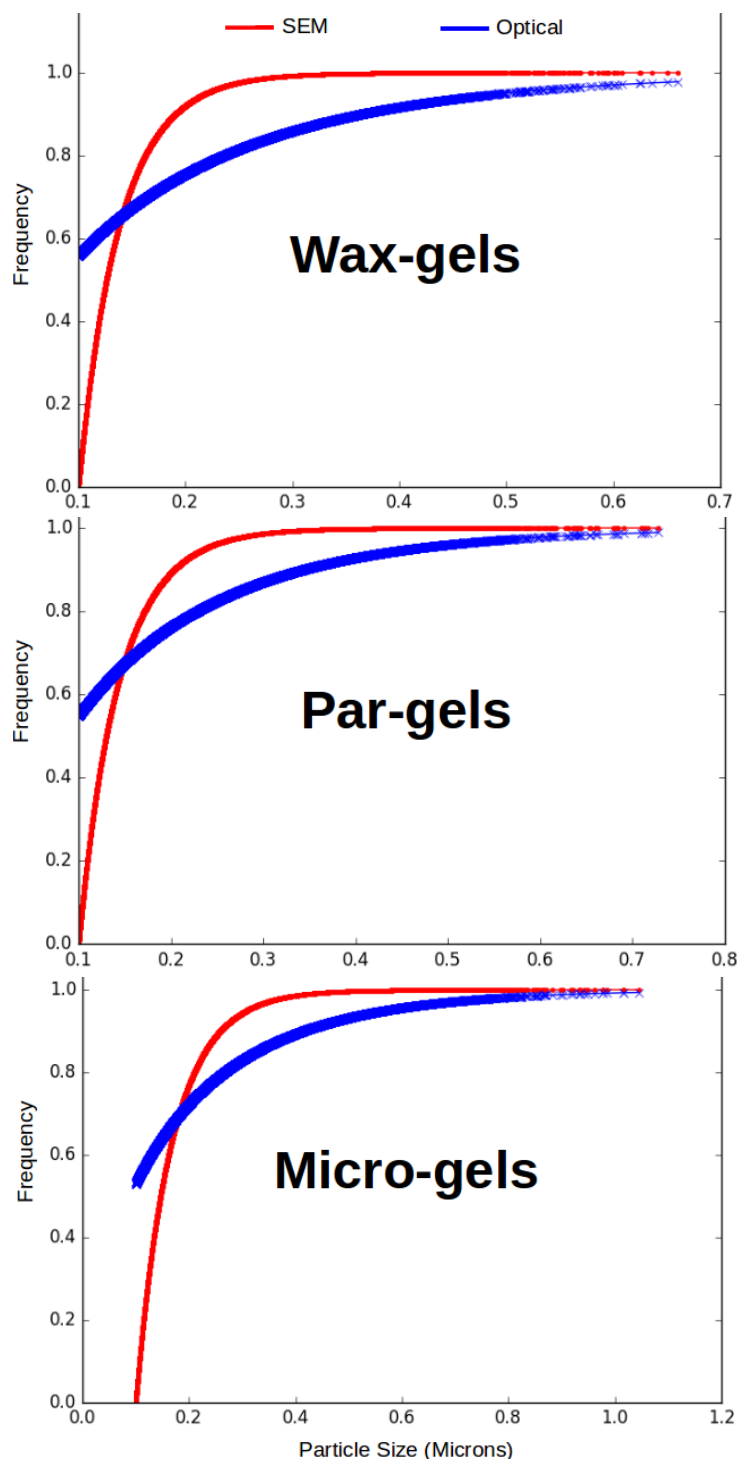
Appendix 9: Optical Micrographs of 17.6 vol% Micro-Gel (100x)



Appendix 10: Pooled Wax-gel Optical Particle Size Best Fits



Appendix 11: Pooled Wax-gel SEM Particle Size Best Fits



Appendix 12: Pooled Wax-Gel Optical-SEM Model Comparison